

University of Alberta

A Numerical Model of Local Water Vapour Transport

by

Luis Prieto



A thesis submitted to the Faculty of Graduate Studies and Research in partial fulfillment of the requirements for the degree of Master of Science

Department of Mechanical Engineering

Edmonton, Alberta
Fall 2006



Library and
Archives Canada

Bibliothèque et
Archives Canada

Published Heritage
Branch

Direction du
Patrimoine de l'édition

395 Wellington Street
Ottawa ON K1A 0N4
Canada

395, rue Wellington
Ottawa ON K1A 0N4
Canada

Your file *Votre référence*
ISBN: 978-0-494-22347-5
Our file *Notre référence*
ISBN: 978-0-494-22347-5

NOTICE:

The author has granted a non-exclusive license allowing Library and Archives Canada to reproduce, publish, archive, preserve, conserve, communicate to the public by telecommunication or on the Internet, loan, distribute and sell theses worldwide, for commercial or non-commercial purposes, in microform, paper, electronic and/or any other formats.

The author retains copyright ownership and moral rights in this thesis. Neither the thesis nor substantial extracts from it may be printed or otherwise reproduced without the author's permission.

AVIS:

L'auteur a accordé une licence non exclusive permettant à la Bibliothèque et Archives Canada de reproduire, publier, archiver, sauvegarder, conserver, transmettre au public par télécommunication ou par l'Internet, prêter, distribuer et vendre des thèses partout dans le monde, à des fins commerciales ou autres, sur support microforme, papier, électronique et/ou autres formats.

L'auteur conserve la propriété du droit d'auteur et des droits moraux qui protègent cette thèse. Ni la thèse ni des extraits substantiels de celle-ci ne doivent être imprimés ou autrement reproduits sans son autorisation.

In compliance with the Canadian Privacy Act some supporting forms may have been removed from this thesis.

Conformément à la loi canadienne sur la protection de la vie privée, quelques formulaires secondaires ont été enlevés de cette thèse.

While these forms may be included in the document page count, their removal does not represent any loss of content from the thesis.

Bien que ces formulaires aient inclus dans la pagination, il n'y aura aucun contenu manquant.


Canada

Abstract

Recent studies suggest an apparently high occurrence of dust devils on Mars. Accordingly, a detailed study of these atmospheric vortices may help to better understand the complex Martian atmosphere and its interaction with the water cycle on the planet. However, field studies of dust devils on Mars are difficult because of their sporadic and unpredictable occurrence. Therefore, laboratory simulations present a better physical insight into this complex swirling flow by consideration of a much simplified, and more controllable model flow. The use of numerical simulations in addition to laboratory experiments also allows for significant flexibility in the model layout and they are, therefore, ideally suited for a comparison of different model flows and scales. The present study investigates several ways to simulate laboratory scale dust devils and to estimate the local water vapour flux rate through the Martian regolith under the influence of dust devils, as well as experimental data to support the numerical results.

Acknowledgements

I am deeply indebted to my supervisor Dr. Carlos F. Lange who believed in me to make this work possible. His suggestions, patience and encouragement helped me to complete this thesis.

Secondly, I would like to extend my sincerest thanks to Prof. Mark Y. Ackerman. His incredible knowledge and experience in the field of laboratory experiments made the data acquisition system a viable solution.

I would also like to thank my lab mates for their wonderful ideas, Dr. Olajide Akinlade and Ifteker Rahman.

My colleagues from the Department of Mechanical Engineering, University of Alberta, Canada, supported me in my research work. I want to thank them for all their help and support.: Rick Bubenko, Jonathan Clark, Bernie Faulkner, Liana Ireland, Tuula Hilvo, Roger Marchand, Greg Miller, Terry Nord, Wayne Pittman and Alan Wilson. I would also like to thank Dr. Douglas R. Schmitt and Len Tober, experts in soils at the Department Geophysics and Physics, for their help in all aspects of porous media.

I acknowledge the financial support from the Canadian Space Agency and the National Sciences and Engineering Research Council of Canada (NSERC).

To my parents

Contents

1	Introduction	1
2	Literature Review	4
2.1	Mechanisms of Mass Transport in Porous Media	4
2.1.1	Advective Flux	4
2.1.2	Molecular Diffusive Flux	6
2.1.3	Knudsen Diffusive Flux	7
2.1.4	Thermal Diffusive Flux	7
2.1.5	Surface Diffusive Flux	8
2.1.6	Models of Mass Transport	8
2.2	Atmospheric Vortices: Dust Devils	9
2.2.1	Theoretical Analysis	10
2.2.2	Field Studies	14
2.2.3	Laboratory Simulations	14
2.2.4	Numerical Models	17
3	Theoretical Modelling	19
3.1	Preamble	19
3.2	Governing Equations	21
3.2.1	Mass Transport	22
3.2.2	Definitions	27
3.3	Dust Devils: Kinematic Similarities	29
3.4	Computational Fluid Dynamics	30
4	Modelling Setup	32
4.1	Laboratory Experiments	32

4.1.1	Vortex Generator	33
4.1.2	Test Table	35
4.1.3	Mini Tank	35
4.1.4	Intrinsic Permeability	36
4.1.5	Porosity	38
4.2	Numerical Simulations	39
4.2.1	Ward's Model	40
4.2.2	Open Model	40
4.2.3	Test Table and Mini Tank	43
4.3	Instrumentation	43
5	Procedures and Results	45
5.1	Porous Medium Properties	45
5.1.1	Porosity	45
5.1.2	Permeability	51
5.2	Data Acquisition	55
5.3	Mass Transport Experiments	58
5.3.1	Test Table	58
5.3.2	Mini Tank	67
5.3.3	Laboratory Air Circulation	72
5.3.4	Vortex Generator	74
5.4	Numerical Simulations	80
5.4.1	Test Table	81
5.4.2	Mini Tank	82
5.4.3	Convective Flux	85
5.4.4	Ward's Model of Laboratory Vortex	89
5.4.5	Open Model of Laboratory Vortex	94
5.4.6	Water vapour and dust devils	100
6	Conclusions	102
	Bibliography	106
	Appendix	115

A Additional Data	115
A.1 Multipycnometer	115
A.2 Pressure Transducer	117
A.3 Volume Flow Transducer	118
A.4 Permeability Data	119
A.5 Adsorption Analysis	119

List of Tables

2.1	Applicability of Gas Transport Models (Adapted from Scanlon et al. [2002]).	9
4.1	Measured Parameters and Instrumentation.	44
5.1	Polyurethane foam bulk density, ρ_{pm}	46
5.2	Multipycnometer foam samples approximate volume.	46
5.3	Average density obtained using the polyurethane foam.	49
5.4	Typical pore diameters for a polyurethane foam.	50
5.5	Permeability sample dimensions.	53
5.6	Water adsorption on polyurethane foams.	70
5.7	Approximate volume flow and RH at lab openings.	73
5.8	Ward's model geometric parameters (adapted from Church and Snow [1993] and Lund and Snow [1993]).	90
5.9	Ward's model boundary conditions (adapted from Church and Snow [1993] and Lund and Snow [1993]).	90
A.1	Pressure obtained for the empty cell.	115
A.2	Pressure obtained for the sphere.	115
A.3	Pressure obtained for sample 1.	116
A.4	Pressure obtained for sample 2.	116
A.5	Pressure obtained for sample 3.	116
A.6	Pressure obtained for sample 4.	116
A.7	Data obtained for the pressure calibration experiment.	118
A.8	Data obtained for the volume flow calibration experiment.	118
A.9	Data obtained for the permeability experiment.	120
A.10	Measured parameters of water adsorption.	121

List of Figures

2.1	a) Tangential velocity profile, U_θ , for a Rankine vortex showing the vortex radius core (r_1), b) Tangential velocity profile, U_θ , for a Burgers-Rott vortex.	11
2.2	A schematic of an idealized tornado-like vortex, adapted from Snow [1982].	11
2.3	A schematic of the Ward-type vortex generator, adapted from Ward [1972].	15
2.4	A schematic of the “Open” model vortex generator	16
4.1	Schematic of the Laboratory Environment	33
4.2	The Vortex Generator Device showing the cylinder-electrical motor combination, the frame, and test table.	34
4.3	Simulated dust devil created using the vortex generator.	34
4.4	Schematic of the test table showing the water reservoir, the porous medium, and the metallic net.	35
4.5	Schematic of the transient study showing the water tank, foam and the removable lid.	36
4.6	Outside view of the permeability test arrangement.	37
4.7	Schematic design of the permeability test.	37
4.8	Multipycnometer used for the porosity test.	38
4.9	Schematic diagram of the Multipycnometer.	39
4.10	3-D Numerical representation of Ward’s Model.	41
4.11	Geometric parameters used for Ward’s model simulation.	41
4.12	Two schematics of open vortex numerical domains: a) rectangular domain, b) cylindrical domain.	42
4.13	Numerical schematic of the Laboratory Open Model including the Test Table.	42

5.1	Calibration curve of the pressure transducer.	52
5.2	Calibration curve of the volume flow transducer.	52
5.3	Permeability test results.	54
5.4	Calibration of Relative Humidity Sensors.	56
5.5	Calibration of Temperature Sensors.	57
5.6	Time Response for the Relative Humidity Sensors.	57
5.7	Relative humidity profiles as a function of time.	60
5.8	Temperature profiles as a function of time.	60
5.9	Water loss profile as a function of time.	61
5.10	Relative humidity profiles as a function of time.	63
5.11	Temperature profiles as a function of time.	63
5.12	Water loss profile as a function of time.	64
5.13	Relative humidity profiles as a function of time.	65
5.14	Temperature profiles as a function of time.	65
5.15	Water loss profile as a function of time.	66
5.16	Transient <i>RH</i> profiles of experiment 4.	68
5.17	Transient <i>RH</i> profiles of experiment 5.	69
5.18	Relative humidity profiles as a function of time (shorter study).	69
5.19	Transient <i>T</i> profiles of experiment 4.	71
5.20	Transient <i>T</i> profiles of experiment 5.	72
5.21	Relative humidity profiles as a function of time.	73
5.22	Relative humidity profiles as a function of time.	75
5.23	Temperature profiles as a function of time.	75
5.24	Water loss profile as a function of time.	76
5.25	Relative humidity profiles as a function of time.	78
5.26	Temperature profiles as a function of time.	78
5.27	Water loss profile as a function of time.	79
5.28	Unstructured mixed element mesh used for the discretization of the test table at mid plane.	81
5.29	Contour of water vapour relative humidity in mid plane of the test table	82
5.30	Relative humidity profile along a vertical line at the centre of the foam.	83
5.31	Unstructured mixed element mesh used for the discretization of the mini tank at mid plane.	83

5.32	A comparison of transient analysis for relative humidity profiles between numerical simulation and experimental data at two different foam locations (bottom and middle position).	84
5.33	Relative humidity profile with no velocity.	86
5.34	Relative humidity profile with a horizontal velocity of 0.01 m/s across the domain.	87
5.35	Relative humidity profile with a horizontal velocity of 0.5 m/s across the domain.	88
5.36	Relative humidity profile at mid line for different room air velocities. Zero height corresponds to the surface of the foam.	88
5.37	Unstructured mixed element mesh used for the discretization of the Ward's model showing the updraft hole region close up.	91
5.38	Contours of the predicted turbulent kinetic energy of the Ward's model, using RSM model (left) and $k - \epsilon$ model (left).	92
5.39	Radial profile at 0.15 m elevation of the tangential velocity component.	93
5.40	Ward's model radial profiles of radial velocity component at different elevations.	93
5.41	Ward's model profile of the axial vertical velocity component at $r = r_0$	94
5.42	Vorticity isosurface in Ward's model.	95
5.43	Vorticity isosurface in the Open model showing the velocity field at a cross-sectional plane.	96
5.44	Vorticity isosurface in the Open model showing the velocity field at a cross-sectional plane.	97
5.45	Open model radial profiles of radial velocity component at different elevations.	98
5.46	Open model axial profile of the axial vertical velocity component at $r = r_0$	98
5.47	Vorticity isosurface in the new Ward's model showing a vorticity of 0.2 s^{-1}	99
5.48	Water vapour profiles under the influence of a dust devil.	101
A.1	A schematic of the calibration set-up used for the pressure transducer.	117

List of Symbols

- A = area, m^2
 a = aspect ratio
 C = dimensionless constant of proportionality
 $C_{1\varepsilon} = k - \varepsilon$ model constant = 1.44
 $C_{2\varepsilon} = k - \varepsilon$ model constant = 1.92
 $C_\mu = k - \varepsilon$ model constant = 0.09
 c_F = drag coefficient...
 D_{va} = binary air-water vapour diffusion coefficient, m^2/s
 $D_{\alpha\beta}$ = binary diffusion coefficient for the component α into β , m^2/s
 h = depth of the inflow layer, m
 $\mathbf{j}_{x\alpha}$ = diffusive flux due to concentration gradients, kg/s
 \mathbf{j}_ϕ = diffusive flux field (vector) of ϕ
 K = intrinsic permeability, m^2
 K_n = Knudsen number
 K_s = saturated permeability, m/s
 k = turbulence kinetic energy, m^2/s^2
 L = dimension scale, m
 L_{pm} = porous medium length scale, m
 L_e = porous medium length scale, m
 l = convection region height, m
 M_a = molecular weight of water vapour, 29 kg/kmol
 M_v = molecular weight of water vapour, 18 kg/kmol
 m = constant of proportionality
 \dot{m} = water vapour losses rate, kg/s
 \dot{m}_A = water vapour losses rate per unit area, $kg/m^2 \cdot s$
 m_α = mass of the component α , kg
 \mathbf{n} = normal vector at A
 P_1 = pressure in V_R with the sphere in the cell, Pa
 P_2 = pressure in V_R and the cell with the sphere in the cell, Pa
 P'_1 = pressure in V_R with no sphere in the cell, Pa
 P'_2 = pressure in V_R and the cell with no sphere in the cell, Pa
 P_1^* = pressure in V_R with no sample in the cell, Pa
 P_2^* = pressure in V_R and the cell with the sample in the cell, Pa

Pr_t = turbulent Prandtl number
 p = pressure of the fluid, Pa
 p_0 = standard atmospheric pressure, 101,325 Pa
 p_a = air partial pressure, Pa
 p_{sat} = saturated pressure, Pa
 p_v = partial water vapour pressure, Pa
 R = universal gas constant, 8314 J/kmol·K
 Re_r = radial Reynolds number
 RH = relative humidity, %
 r_0 = radius of the updraft hole, m
 S_i = additional momentum sources in the i direction
 S_{ij}, S_{ji} = rate of deformation
 $S_{\chi\alpha}$ = additional sources of $\chi\alpha$
 S_{Φ} = additional sources of Φ
 S_{ϕ} = additional sources of ϕ
 T = temperature, K
 T_0 = water temperature freezing point, 273.15 K
 t = time, s
 U_r = radial velocity, m/s
 $U_{(r, local)}$ = local radial velocity at any point
 U_{θ} = tangential velocity, m/s
 $U_{(\theta, local)}$ = local tangential velocity at any point
 \mathbf{u} = velocity field (vector) of the fluid, m/s
 u_i, u_j, u_k = velocity component in the index notation, m/s
 u'_i, u'_j, u'_k = time-varying fluctuating velocity component in the index notation, m/s
 V = total volume of the fluid mixture, m^3
 V_C = cell volume sample, m^3
 $V_{g sphere}$ = volume of the calibration sphere, $56.58 \cdot 10^{-6} \text{ m}^3$
 V_R = reference volume, m^3
 W_l = instantaneous water weight, kg

Greek symbols

χ_v = water vapour mass fraction
 χ_{α} = mass fraction of the component α
 δ_{ij} = Kronecker delta function
 Γ_{Φ}^* = turbulent diffusion coefficient of Φ
 Γ_{ϕ} = diffusion coefficient of ϕ
 μ = dynamic viscosity, Pa·s
 μ_t = eddy viscosity, Pa·s
 Φ = turbulent scalar quantity of the fluid
 Ψ_{ij} = quadratic pressure-strain correlation, $\text{kg/m} \cdot \text{s}^3$
 ϕ = scalar quantity of the fluid

ρ = total density of the fluid, kg/m³
 ρ_a = air density, kg/m³
 ρ_y = solid phase average porous medium density, kg/m³
 ρ_v = water vapour density, kg/m³
 ρ_{pm} = porous medium bulk density, kg/m³
 ρ_α = density of the component α
 $\sigma_k = k - \varepsilon$ model constant = 1.0
 $\sigma_\varepsilon = k - \varepsilon$ model constant = 1.3
 τ = tortuosity
 Υ_{ij} = shear turbulence production, kg/m·s³
 ε = turbulence dissipation rate, m²/s³
 φ = porosity
 ζ = blend factor, $0 \leq \zeta \leq 1$

System of coordinates

x, y, z = Cartesian system
 r, θ, z = cylindrical system
 i, j, k = index notation

Overbar

- = average conditions; time mean

Chapter 1

Introduction

The recent discovery of ancient oceans on Mars based on the exploration of the landers Spirit and Opportunity has changed our perspective of our neighbouring planet. Hence, new questions are being raised among scientists about the Martian current cycle of water and its history. The upcoming Phoenix Mars Lander, a joint US-Canada mission, is designed to investigate this natural event on Mars. The lander will search for frozen water below the Martian surface, as well as recording atmospheric conditions, by using a robotic arm and a meteorological station. The research will study mass exchange of water vapour between the regolith and the atmosphere of Mars. However, due to the payload restrictions only a fraction of the ideally required measurements can be performed. Therefore, the development of a reliable mathematical model that may help analyse data provided by the lander, and identify the relevant physical mechanisms that cause water vapour transport is needed. Previous studies of the water vapour transport, such as those by Mellon and Jakosky [1993], and Savijarvi [1995] have investigated the phenomenon in a one-dimensional approach on the entire Martian atmosphere. The proposed model, in contrast, will address the immediate vicinity of the lander and simulate its three dimensional near field.

An understanding of mass transport in porous media is important to quantify the water vapour transport through the Martian regolith. The complexity of the study is

evidenced by several processes [de Groot and Mazur, 1984, Do, 1998] that may take part in the mass transport: Advective Flux, Molecular Diffusive Flux, Knudsen Diffusive Flux, Thermal Diffusive Flux, and Surface Diffusive Flux. In a natural porous medium the distribution of pores based on shape and size is somehow non-isotropic. Hence, on the pore scale the flow quantities (velocity, pressure, temperature, etc.) will be clearly irregular. In order to make the mass transport studies amenable for theoretical treatment (conservation laws), the flow quantities of interest need to be measured over a space-averaged (macroscopic) volume. However, an appropriate characterization of the pore structure to ensure averaged macroscopically equivalent dimensions requires physical samples, which in the case of the Martian regolith, is not possible for the current stage of the present study. Consequently, the use of materials that simulate the regolith may provide a controlled boundary condition necessary to the validation of the model. There have been past studies of the water transport in porous media on Earth and Martian conditions, such as those by Gu et al. [1998], Travis et al. [2003], respectively. They analysed the water vapour transport due to thermal diffusion and Knudsen diffusion. These studies could indeed provide useful information to formulate a model valid in both environments. In addition, the combined effects of other several processes present in the atmosphere may also take part in the spatial variations in the column of water vapour in the Martian near surface region. Among these processes, dust devils could be an important local factor in the water concentration levels. In fact, the apparently high occurrence of dust devils on Mars [Thomas and Gierasch, 1985, Metzger et al., 1999] could potentially affect the mass transfer rate of water vapour from the Martian regolith.

Basically, dust devils are atmospheric events characterized by a low pressure, warm core vortices with a vertical upward flow forming the core, a weaker downdraft flow near the centre, and a lateral layer flow close to ground. A typical dust devil resembles an inverse cone, with a relative size smaller than tornadoes, and differing from the latter in the mechanism of formation [Idso, 1974]. They have been observed in hot desert areas [Sinclair, 1969, Hess and Spillane, 1990], and sub-arctic regions

[Wegener, 1914, Grant, 1949]. A detailed study of these atmospheric vortices may help to better understand the complex relation between the cycle of water and this atmospheric event on Mars. Subsequently, field data are required to provide a close estimation of the dynamics presented in the Martian surface. However, field studies of dust devils, such as Hannesen et al. [2000], and Bluestien et al. [2003] to mention some, are difficult because of their sporadic, unpredictable occurrence and distance. In contrast, laboratory simulations present a better physical insight into this complex swirling flow by consideration of a much simplified, and more controllable and reproducible model flow. The use of numerical simulations in addition to laboratory experiments can provide complementary information on flow properties in regions where measurements are difficult due to flow profiles. Computational models also allow for significant flexibility in the model layout and they are, therefore, ideally suited for a comparison of different types of model flows.

The objectives of the present work were as follows: to define a numerical model capable of estimating local flux of water vapour on the Martian regolith, and to evaluate the effects of dust devils on the water vapour transport on Mars. A theoretical model will first be presented followed by the description of the numerical simulations. Experimental results will then be presented and discussed.

Chapter 2

Literature Review

This chapter is divided into two different parts. The first begins with the mechanism of mass transport and how it is applied to soil-related studies. The second field concerns about atmospheric vortices.

2.1 Mechanisms of Mass Transport in Porous Media

Fluids move through the earth in response to driving forces acting upon them. Hence, in flow systems where the fluid is gas through a porous material, there are five primary mechanisms of mass transport: Advective Flux, Molecular Diffusive Flux, Knudsen Diffusive Flux, Thermal Diffusive Flux, and Surface Diffusive Flux [de Groot and Mazur, 1984, Do, 1998]

2.1.1 Advective Flux

In simple flow systems, the fluids follow a linear relationship between pressure gradients and velocity fields. Particularly, liquid water flow through permeable materials obeys a fundamental law known as Darcy's Law (see Chapter 3). Darcy [1856] first

established his flow equation for water flow in saturated sand. More generally, it is now known that the Darcy's law applies to flow of most simple liquids in any permeable (and porous) medium. It describes that the flow rate is proportional to the difference in head of two points (pressure gradient), and inversely proportional to the distance between them, where the proportionality constant is known as hydraulic conductivity, which measures the ability of a media to transmit a fluid. Since most soils are unsaturated, Buckingham [1907] developed a generalization of Darcy's law for unsaturated flow, where the hydraulic conductivity is not necessary a constant, but function of water content in the medium. However, the linearity of this more general form of the Darcy's equation may fail for high flow velocity regimes [Hubbert, 1956], due to the fact that the form drag due to solid obstacles is now comparable with the surface drag due to friction. In other words, inertial forces are no longer negligible compared to viscous forces. Joseph et al. [1982] based on studies of Dupuit [1863] and Forchheimer [1901] developed an appropriate modification of Darcy's equation to include the inertial terms. For packed beds a more specific application of the inertial term is expressed in terms of a friction factor known as Ergun and Carman-Kozeny equations (Further details are explained by Bird et al. [2001]). Finally, in order to extend Darcy's law to other liquids or gases, the hydraulic conductivity can be broken down into properties of the fluids and properties of the medium. To separate these terms, the hydraulic conductivity is written in terms of the specific or intrinsic permeability, which is a property of the porous medium alone [Bosch and Shirmohammadi, 2003].

Relatively small pressure gradients described by Darcy's law can result in advective fluxes that are greater than other mechanisms of gas fluxes, such as diffusivity processes [Alzaydi and Moore, 1978, Thorstenson and Pollock, 1989, Massmann and Farrier, 1992]. This is when the mean free path of gas molecules is much less than pore radius or particle radius, resulting in intermolecular collisions being dominant relative to collisions between gas molecules and the pore walls [Cunningham and Williams, 1980]. However, when the mean free path of the molecules becomes approximately

the same as the pore radius, a transition or change occurs into the advective flux to a viscous slip flux [Klinkenberg, 1941]. In other words, the intrinsic permeability of a dry porous medium obtained by measuring gas flow is larger than corresponding permeability from liquid flow. Stonestrom and Rubin [1989] and Detty [1992] found that errors resulting from ignoring viscous slip flux in dry coarse-grained porous media (sands) were less than 7%.

2.1.2 Molecular Diffusive Flux

In a fluid mixture, the local concentration of a mass species can be expressed in a similar manner as the Darcy's Law, that is, a linear relation between a flux and a corresponding driving force. Fick [1855] proposed what has become known as his first law (Fick's law), a relation between the rate of diffusion of chemical species and the local concentration gradient of the species. Fick's law (see 3) was originally developed to describe molecular diffusion of solutes in liquid solutions. More generally, Fick's law is used to describe molecular diffusion of one gas into another [Jaynes and Rogowski, 1983, Bird et al., 2001]. It should be noted that Fick's law is strictly applicable to molecular diffusion of equimolar (similar molecular weights) gases in isothermal, isobaric conditions. In addition, it is important to mention that Fick's law can predict the flux of only one chemical species. When the gas mixture is composed of two nonequimolar components, lighter molecules have higher velocities than heavier molecules, as a consequence, a more rapid diffusion of the lighter gas molecules results in a partial pressure gradient. An appropriate modification of the Fick's law adds an extra term called nonequimolar flux to include the flux resulting from these partial pressure gradients [Cunningham and Williams, 1980]. Similar to Darcy's Law, a proportional constant is used to measure the ability of one chemical species to diffuse into another, and it is known as a free space diffusion coefficient. There are several studies of diffusion coefficients. For a review of these studies, see Massmann [1998]. When Fick's law is applied to a porous medium, an effective diffusion coefficient is used to account for the obstruction caused by the material [Do,

1998].

2.1.3 Knudsen Diffusive Flux

A second type of diffusion flux occurs when the gas mean free path is the same order as the pore radius. This condition corresponds to the Knudsen regime [Alzaydi, 1975, Abu-EL-Sha'r, 1993]. Knudsen [1909] introduced an important criterion for molecular flow at low pressure, where the driving force is a partial pressure gradient. Knudsen diffusion can be described in precisely the same way as Fick's law, but differs in the proportionally constant, where the coefficient of diffusion depends on temperature and pressure, and the Knudsen diffusion coefficient relates molecular weights, temperatures, and geometry of the porous media [Clifford and Hillel, 1986].

In case of a Knudsen regime, molecule-wall collisions dominate over the molecule-molecule collisions (Fick's law). Therefore, the study of transport diffusion due to the Knudsen flux is no longer negligible compared to molecular diffusion; indeed, Sleep [1998] found that environmental conditions, such as low permeability materials or sub atmospheric pressures, may increase the transport diffusion by 40% due to the Knudsen flux compared to those predicted with a Fick's model only. In addition to the above, Clifford and Hillel [1986] considered Knudsen diffusion as an important mechanism for flow through porous media on Mars. However, Knudsen diffusion may not be relevant for laboratory experiments under Earth atmospheric pressures and high permeability porous media.

2.1.4 Thermal Diffusive Flux

The presence of a thermal gradient in a fluid mixture induces a relative diffusive flux of the chemical species known as thermal diffusion or Ludwig-Soret effect. Ludwig [1856] described a cross-flow effect induced by temperature differences based on salt solution experiments. The thermal diffusion has been found not only in liquids, but also in

gases [Mason et al., 1966]. The thermal diffusive flux adds a new term into the Fick's law by introducing a new quantity called the coefficient of thermal diffusion [de Groot and Mazur, 1984], which is proportional to the free space diffusion coefficient. The ratio of the thermal coefficient to the free space coefficient is called the Soret coefficient [Soret, 1879]. Tyrrell [1961] has described some typical values of the Soret coefficient in several gases. The mass transport cases included in the present study will be confined to isothermal flows and, therefore, this transport mechanism will not apply.

2.1.5 Surface Diffusive Flux

In surface diffusion, the mass transport is confined to a surface in an adsorbed layer, and it is driven by local concentration gradient as same as the molecular diffusion. Higashi et al., 1963 assumed that when a molecule hit a site occupied by another molecule it would immediately bounce off and continue until finding an unoccupied site. This interaction with the surface is strongly affected by the size of the molecule in movement [Do, 1998]. The surface diffusive flux is commonly assumed as an independent mechanism of mass transport, and it may be defined a manner similar to Fick's law [Gilliland et al., 1974]. There are also several other forms to express surface diffusion, among them Schneider and Smith [1968], and Patel and Butt [1972]. However, this method of mass transport will not be addressed in the present study, since in most soil-related applications it can be neglected [Thorstenson and Pollock, 1989].

2.1.6 Models of Mass Transport

Diffusive gas transport in soils has traditionally been modelled using Fick's law, whereas advective gas transport has been by Darcy's law. In theory, the resulting mass fluxes can be then linearly added to yield to a total flux. Unfortunately, as shown by Webb [1996], this approach may not be appropriate in presence of non-equimolar fluxes. However, for air and water vapour, where the air is treated as a

single “dry-air” component, the molecular weights are relatively similar such that the error involved by neglecting the nonequimolar flux is less than 1 percent zero [Bird et al., 2001, Çencel, 2007]. In addition, Fick’s law as described before applies only to binary system. A more general case, the Stefan-Maxwell equations [Bird et al., 2001] describe gas diffusion in a multicomponent system (a system containing two or more gases). However, the accuracy of this approach could be compromised when the Knudsen diffusion is no longer negligible and the system is nonisobaric. Finally, the Dusty Gas model, developed originally by Mason et al. [1967], is a more general theoretical frame for multicomponent nonisobaric systems in porous media, and it accounts for all types advection-diffusive flows described above. Ho and Webb [1996] and Scanlon et al. [2002], present an extensive discussion of the applicability of each gas transport model. These authors identified the most appropriate models for describing gas flux under different pressure, permeability, total pressure gradient, and component concentrations. Their recommendations are summarized in Table 2.1.

Table 2.1: Applicability of Gas Transport Models (Adapted from Scanlon et al. [2002]).

Pressure Gradient	Permeability	Low Concentration	High Concentration
Isobaric ¹	Low	Dusty Gas Model	Dusty Gas Model
Isobaric ¹	High	Fick’s Law	Stefan-Maxwell
Nonisobaric	Low	Dusty Gas Model ²	Dusty Gas Model ²
Nonisobaric	High	Advection Diffusion	Dusty Gas Model

¹Total system

²Includes advective flux

2.2 Atmospheric Vortices: Dust Devils

Atmospheric vortices present a wide variety of flows, not only in the range of sizes and intensities, but in the different flow structures encountered. Moreover, different environmental conditions may affect the form of the vortices’ “internal” structures. How to categorize and to scale-down these structures has been a long-standing goal of

vortex research. There are a number of approaches to obtaining a better understanding of the kinematics of the atmospheric vortices such as dust devils. These include theoretical modeling, field study, laboratory simulation and numerical modeling.

2.2.1 Theoretical Analysis

Theoretical models have been developed to characterize, understand, and classify the atmospheric vortices and to break them down into different physical mechanisms. A number of reviews of these models are available in the literature [Davies-Jones and Kessler, 1974, Davies-Jones, 1982, Lewellen, 1993]. Tornado-like flows can generally be divided into two categories on the basis of scale [Snow, 1982]. The first category, which it is not addressed in this study, deals with the creation and time dependency of vortices caused by environmental conditions. The second category concerns the kinematics of the vortex. In other words, the objectives in this area are to describe and explain physically the flow characteristics of wind speed and pressure near the vortex.

Rankine [1858] developed the simplest solution for the Navier-Stokes equation in vortex flows. He assumed that the core of the vortex was axisymmetric, and the radial and axial velocities were zero. This simple distribution does match the coarse features of the tangential velocities observed in tornadoes well above the surface. The Rankine vortex uses an ideal core that rotates nearly as a solid body, where the tangential velocity is proportional to the radius, and an approximately irrotational vortex outside of the core, where the same velocity is inversely proportional to the radius [Kundu, 1990] (see Figure 2.1a). However, this idealization gives no information on the other velocity components, since they are ignored. A more complete solution to the axisymmetric Navier-Stokes equation was obtained by Burgers [1948], and independently by Rott [1958]. This solution, known as Burgers-Rott, includes a radial velocity proportional to the radius and a tangential velocity as a function of the radial velocity (see Figure 2.1b).

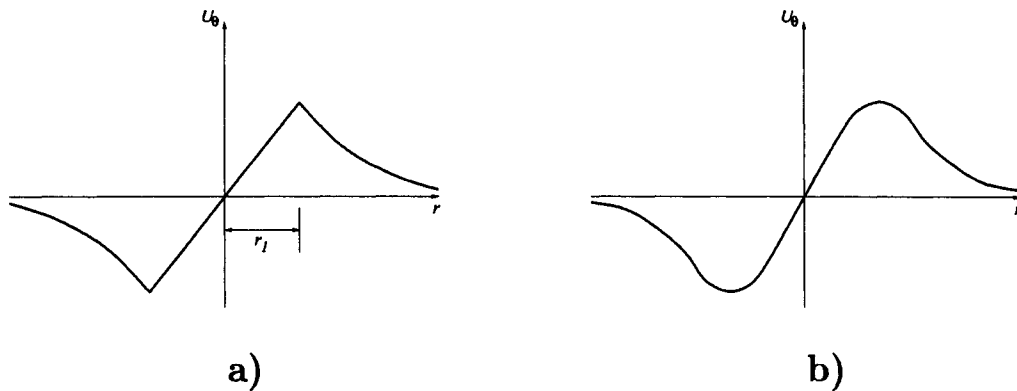


Figure 2.1: a) Tangential velocity profile, U_θ , for a Rankine vortex showing the vortex radius core (r_1), b) Tangential velocity profile, U_θ , for a Burgers-Rott vortex.

The nature of the tornado-like vortex, where the different areas have different flow structures makes it convenient to separate the flow into five different regions based on the physical mechanism that appears to be common to all atmospheric vortices [Morton, 1970, Lewellen, 1976]. Figure 2.2 shows the main regions of a vortex domain.

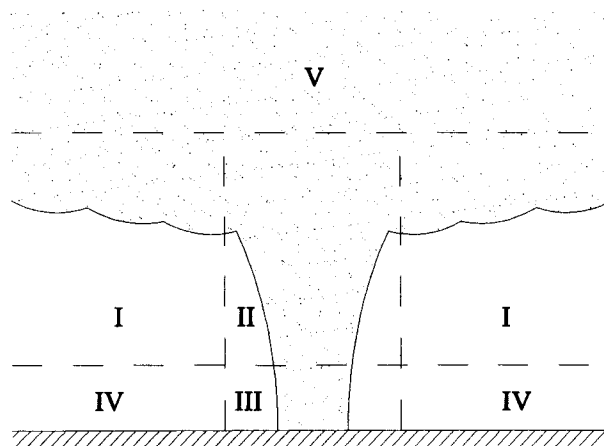


Figure 2.2: A schematic of an idealized tornado-like vortex, adapted from Snow [1982].

- Region I, the Outer Flow, extends from the vortex core, where the radial motion

is being suppressed, out to a radius of a few kilometres where it blends into the parent tornado cyclone. Over most of this region the flow spirals inward and upward. The tangential velocity could be described using the idealization of Rankine vortex or of Burgers-Rott outside of the core. However, this region is not irrotational since radial and vertical velocities are both present [Snow, 1982].

- Region II, the Core Flow, confines the central part of the vortex. This region presents an almost solid body profile, with a strong updraft surrounding a weaker downdraft stream [Hall, 1966]. In addition, the radius of the core is defined along the maximum tangential velocity.
- Region III, the Corner Flow, represents the inner region of the tornado-like flow, as shown in Figure 2.2. It is here where the flow appears to have the highest absolute velocities to be found within the vortex [Lewellen and Sheng, 1980]. In fact, the outer limits of this region are taken at the radial location where the radial velocity has its maximum absolute value [Wilson and Rottuno, 1982].
- Region IV, the Inflow, consists of a boundary layer feeding the tornado. The kinematics of this region has been widely studied by Rottuno [1980], Morton [1981], and Wilson and Rottuno [1982]. Some important characteristics to mention from these studies are: Radial and tangential components of the velocity are relatively large, while the axial component is comparatively small. The fluid is accelerated inward toward Region III due to unbalanced pressure gradient forces, where the fluid is being drawn from Region I.
- Region V, the Rotating Convective Plume, concentrates the vertical flow that emerges from the lower atmospheric system. Very little specific information is known about this region, but it seems that it may extend into the lower stratosphere. How this flow structure and its dynamics interact with the other regions is being slowly revealed, primarily by Doppler radar studies [Lewellen, 1976, Snow, 1982].

For the present study the analysis and characterization of the tornado-like vortex will be confined to the Corner Flow and the Inflow regions (Figure 2.2), since these zones are in direct contact with the surface and they are most likely to influence the water mass transport through the regolith.

Rennó et al. [1998](see also Rennó et al. [2000]) proposed a scaling theory based on the thermodynamic mechanisms responsible for the maintenance of pressure drop across dust devils. The intent of the present study is not to discuss these thermal mechanisms, rather the kinematic and geometric similarity parameters present between different dust devils.

Lewellen [1962] has shown, based on the Navier-Stokes equations, that two length scales and two velocity scales can be applied to characterize a swirling sink flow. Further, Davies-Jones [1973] found that by applying these parameters, the governing equations of an axisymmetric vortex can be nondimensionalized by defining three important dimensionless quantities, namely a radial Reynolds number, an internal aspect ratio, and a swirl ratio (see Chapter 3). Church and Snow [1993] explains that the swirl ratio and radial Reynolds number control the kinematics of the flow, while the aspect ratio controls its geometry. All these parameters could be scaled down for any size domain except for the radial Reynolds number. The problem arises from the fact that when air is used as a fluid of study, the fluid needs to increase its velocity to compensate for the small length scale, which in practice proves unfeasible. Two approaches have been developed to overcome this problem [Teunissen, 1974]. In one approach it is hypothesized that there should exist a critical value of Reynolds number, above which this number has no significant effect on the similarity of the flow. The second one argues that different molecular air viscosity parameters, one for the large-scale natural event, and another for the model, should be used to calculate the Reynolds number. Because this model is primarily used in mesoscale simulations, this approach will not be used in the present study. Fortunately, the dependence of flow characteristics on the Reynolds number appears to be weak over smooth surfaces

[Church and Snow, 1993], as in laboratory experiments. However, the dependence on Reynolds number over rough surfaces is not well established yet.

2.2.2 Field Studies

What we know about tornado-like vortices, where tornadoes, dust devils, and waterspouts are included, is mainly from in situ studies, such as Vasiloff [1993], Hannesen et al. [2000], Bluestien et al. [2003], to mention some. It should be noted that, even though most of the studies presented here are related to tornadoes, a fair comparison between them and dust devils is feasible, since it appears that the main differences among them are the mechanisms of formation [Idso, 1974]. In fact, in a series of studies of dust devils, Sinclair [1969, 1973] and Kaimal and Businger [1970] showed that the dust devil core presents a nearly solid body rotation, where the tangential velocity profile follow into a typical Rankine vortex.

Dust devils have been observed in hot desert areas [Sinclair, 1969, Hess and Spillane, 1990], and sub-arctic regions [Grant, 1949]. Dust devils also have been seen on Mars by the Viking Orbiter [Thomas and Gierasch, 1985]. More recently, the Mars Orbiter, and Pathfinder imaged additional dust devils from orbit [Edgett and Malin, 2000, Balme et al., 2003], and the surface [Metzger et al., 1999, 2000]. Indeed, recent images from the Martian lander, Spirit, could suggest an apparently high occurrence of dust devils on Mars. Hence, knowledge of these atmospheric phenomena is an important local factor to be included in the quite complex Martian water cycle.

2.2.3 Laboratory Simulations

Field studies of dust devils are difficult because of their sporadic, unpredictable occurrence and distance. In contrast, laboratory simulations present a better physical insight into this complex swirling flow by consideration of a much simplified, and more controllable and reproducible model flow. Although a number of experimental

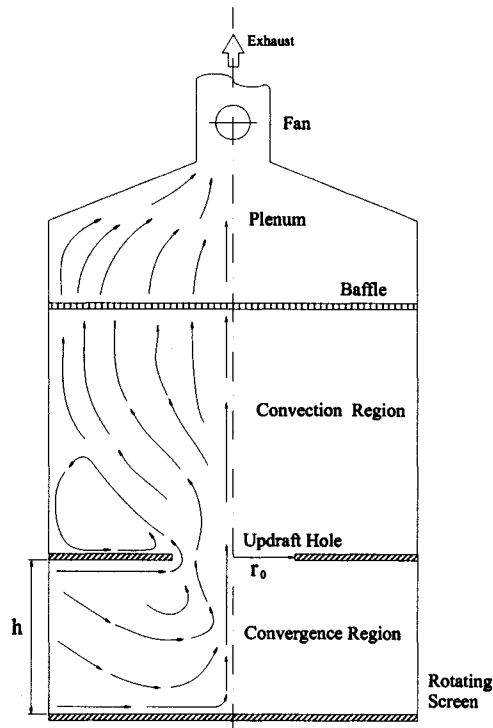


Figure 2.3: A schematic of the Ward-type vortex generator, adapted from Ward [1972].

models have been constructed in the past to represent tornado-like vortices, Davies-Jones [1976], in a review of different type of laboratory simulators, concluded that the most appropriate apparatus that reproduces similar kinematics (swirl ratio) and geometry (aspect ratio) characteristics of natural vortices is a Ward [1972] (shown in Figure 2.3) type tornado chamber.

The Ward model represents, in a laboratory scale, the inflow layer, corner flow, and core flow of a real tornado-like vortex. Basically, air flows into a convergence zone (inflow layer) through a series of directional vanes before entering the convective area (corner flow) where it rises and exits the model (core flow) through a fine mesh honeycomb. The honeycomb prevents the fan from inducing vorticity into the apparatus. It also removes the rotation from the outflow and, therefore, decouples the vortex from the fan. This creates a non rotating flow overlying the top of the vortex, as

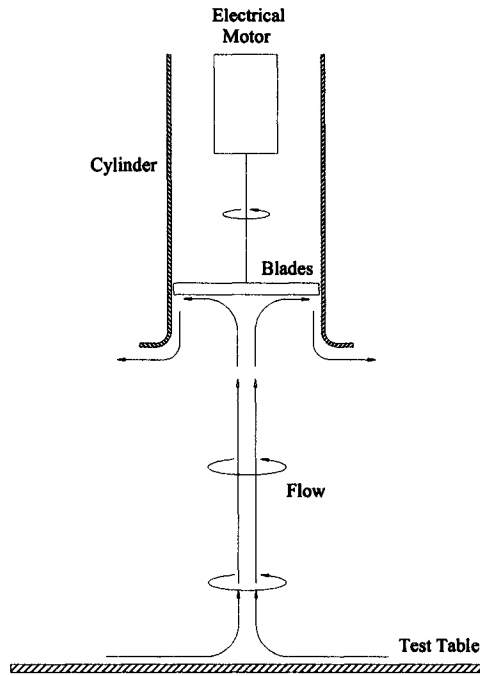


Figure 2.4: A schematic of the “Open” model vortex generator

must be the case in the atmosphere [Davies-Jones, 1976].

In spite of the advantages of the Ward type model, for a vortex that moves along the surface, the use of the Ward model is not feasible. For this reason, other approaches of tornado-like vortex laboratory simulators are presented here to overcome this issue. Hsu [1973] developed an open model tornado generator, where the air is driven downward by a fan, which is enclosed in a fixed cylinder. A simplified version of Hsu’s model was developed by Greeley et al. [2001] and it is shown in Figure 2.4, where the vortex can be moved laterally to simulate motion of a dust devil across the terrain. The vortex generator consists of a cylinder with a “belt mouth” to alleviate boundary effects at the edge, a motor drive, and a fan blade system. This model was designed to simulate dust devils by inducing an upward angular momentum in the flow using viscous forces. However, this type of generator produces relatively weak vortices. A second, and more robust vortex generator was developed by Gallus et al.

[2006]. This model is very much similar to the Ward model except that it includes a fan just above the honeycomb to create a stronger vortex. This design thereby permits tangential velocities of up to 96 km/h.

2.2.4 Numerical Models

The use of numerical simulations in addition to laboratory experiments can provide complementary information on flow properties in regions where velocity gradients make flow profiles difficult to obtain [Snow and Lund, 1997]. Computational models allow for significant flexibility in the model layout and they are, therefore, ideally suited for a comparison of different types of model flows.

There are two main approaches to reproduce a numerical tornado-like vortex. The first approach, which it is not addressed in the present study, deals with the creation and time dependency of vortices caused by environmental conditions such as buoyancy forces [Nolan and Farrell, 1999, Zhao et al., 2004, Kanak, 2005]. However, the disadvantages of those simulations are still the absence of a robust method to characterize and to compare different tornado-like vortices or the attempt to use the Reynolds number as a nondimensional parameter for relatively small length scales [Teunissen, 1974]. The second category, a more idealized model, deals with the reproduction of vortices by introducing a source of momentum as the boundary condition, and neglecting other factors, such as temperature [Lewellen and Lewellen, 1997, 2000]. The present study focused on small-scale momentum-induced vortices, since a better understanding of full-scale atmospheric vortex simulations must be preceded by simulations of a more controllable numerical laboratory scale vortex. One of the first attempts to reproduce a numerical vortex of a laboratory simulator based upon Ward's model was presented by Rottuno [1977, 1984]. Current research by Gallus et al. [2006] deals with a numerical model that represents a laboratory scale vortex generator. Here, the authors compared their numerical results with radar measurements of a real tornado [Alexander and Wurman, 2005]. They have concluded that

the numerical model is in good agreement with the radar observations. Finally, two turbulence models will be used to reproduce the numerical vortices. The two-equation model known as the $k - \varepsilon$ model [Launder and Spalding, 1974], and the Reynolds stress model developed by Speziale et al. [1991].

Chapter 3

Theoretical Modelling

3.1 Preamble

The objective of the present work was to develop a numerical model that predicts the water vapour transport through a Martian regolith subject to a Martian atmospheric event, namely a dust devil. There have been many studies of water vapour transport in porous media, and of dust devils on Mars. However, these studies have been conducted separately without including the effects of one event on the other. The proposed model, in contrast, attempts to take into account the physical effect of atmospheric vortices on the water vapour transport.

The approach used in this study was as follows:

- Estimate of water vapour transport in porous medium.

A quantitative study of water vapour rate through a porous medium was needed to verify and to validate theoretical predictions. Two different experiments were required to carry out this analysis. First, a proper characterization of the porous medium was conducted. The study of water transport required the knowledge of the fluid properties and physical characteristics of the medium through which the water vapour is moving. Two main parameters are required to properly

characterize the porous medium: Intrinsic permeability and porosity. A simple airflow test was designed to assess the intrinsic permeability by evaluating the pressure differences with a series of prescribed air flow rates through a foam sample. Porosity was evaluated using a multipycnometer, a device able to measure void volume based on the principle of the ideal gas law. Second, an experimental method to directly assess the water vapour flux rate was developed. Accordingly, a laboratory device consisting of a water reservoir covered with a foam layer was equipped with sensors that evaluated local relative humidity for water vapour profile analysis. This experiment also included a mass balance to measure the total water losses due to evaporation.

- Evaluate the effect of a vortex on water vapour flux in the porous medium. The influence of vortex events over the Martian near-surface water cycle requires an estimate of the effect of advection flux of the water vapour inside the porous medium. This device, similar to the one used by Greeley (2001), was used to generate a laboratory scale dust devil above the foam layer. The quantification of the enhanced mass rate of water vapour transport is critical for the validation of the numerical model, since the advection flux is considered the dominant term in the governing transport equation. As with the foam, a proper characterization of the vortex is important in order to understand how different combinations of pressure and velocity profiles affect the amount of water vapour transported through the foam layer. A series of pressure transducers placed along the surface of the foam were used to assess the pressure profile caused by the vortex. Finally, the development of a practical definition of scaling parameters for dust devil vortices is necessary in order to provide a simple method to apply results from laboratory studies and numerical simulations to real terrestrial and Martian atmospheric events.

These objectives are required stepping stones in the pursuit of an accurate numerical model capable of estimating local flux of water vapour in the Martian regolith. However, it is important to mention that in order to provide a more complete numerical

model, future studies are required to examine the relationship between water vapour transport, Knudsen diffusion, and thermal diffusion, since these mechanisms may play an important role under Martian conditions.

3.2 Governing Equations

The atmospheric pressure on Mars is approximately 1 % of that on Earth. As a consequence, the continuum assumption can be questioned. However, for the present study, both laboratory experiments and numerical simulations are conducted under Earth's conditions, where the continuum approach applies. Considering a generic conserved variable, ϕ , a conservative form of the governing equation for any type of fluid flow can be written as [Versteeg and Malalasekera, 1995]:

$$\frac{\partial \rho \phi}{\partial t} + \nabla \cdot (\rho \phi \mathbf{u}) = \nabla \cdot (\Gamma_\phi \nabla \phi) + S_\phi \quad (3.1)$$

The equation 3.1 highlights the several transport processes involved in a general flow problem. The first left hand side term represents the rate of change with time of the property ϕ , where the second term represents the convective part of the transport equation. The diffusive term, and the source term respectively are shown on the right hand side. If in equation 3.1 we insert $\Gamma_\phi \nabla \phi = -\mathbf{j}_\phi$, where \mathbf{j}_ϕ represents the diffusive flux, we obtain:

$$\frac{\partial \rho \phi}{\partial t} + \nabla \cdot (\rho \phi \mathbf{u}) = -\nabla \cdot \mathbf{j}_\phi + S_\phi \quad (3.2)$$

Following the general form given by equation 3.2, the governing equations used in the present study to solve for velocity, and pressure of a compressible Newtonian fluid are:

- Conservation of Mass:

$$\frac{\partial \rho}{\partial t} + \nabla \cdot (\rho \mathbf{u}) = 0 \quad (3.3)$$

- Conservation of Momentum:

$$\frac{\partial \rho u_i}{\partial t} + \nabla \cdot (\rho u_i \mathbf{u}) = -\nabla p + \nabla \cdot (\mu \nabla u_i) + S_i \quad (3.4)$$

The calculation of the mass flux is explained in the next section.

3.2.1 Mass Transport

Water vapour transport is described as a multicomponent fluid, since it involves the transport of a component, the water vapour, in a fluid mixture (air-water vapour). Therefore, an additional balance equation beside equations 3.3 and 3.4 must be solved to determine how the components of the fluid mixture, also known as species, are transported within the flow. Consequently, some considerations are necessary to properly describe the fluid mixture.

Assume a fluid mixture of volume V and mass m . Let the subscript α refer to the α^{th} component of the mixture. Therefore, the total mass density of the fluid ρ is equal to the sum of the individual mass concentration components α , so $\rho = \Sigma \rho_\alpha$. Here ρ_α is defined as the individual mass concentration component α per unit volume of the fluid.

$$\rho_\alpha = \frac{m_\alpha}{V} \quad (3.5)$$

A common way to define ρ_α in terms of ρ is called mass fraction and it is defined as

$$\chi_\alpha = \frac{\rho_\alpha}{\rho} \quad (3.6)$$

If in equation 3.2 we insert $\phi = \chi_\alpha$, we obtain

$$\frac{\partial \rho \chi_\alpha}{\partial t} + \nabla \cdot (\rho \chi_\alpha \mathbf{u}) = -\nabla \cdot \mathbf{j}_{\chi_\alpha} + S_{\chi_\alpha} \quad (3.7)$$

As mentioned before, there are four primary mechanisms of mass diffusion: Molecular Diffusive Flux, Knudsen Diffusive Flux, Thermal Diffusive Flux, and Surface Diffusive Flux [de Groot and Mazur, 1984, Do, 1998]. However, for the present study some assumptions could be made to simplify the analysis of the mass transport process:

- The Knudsen diffusion can be ignored, since under the laboratory conditions the mean free path, λ , is much smaller than the geometrical length scale the molecule travels through (see Chapter 5 for a proof of this statement).

- The thermal diffusion can be suppressed, since the process is carried out under isothermal conditions.
- The surface diffusion can be neglected for all major soil-related applications.
- The fluid mixture is treated as an equimolar flux, where the air component acts as “dry-air” component, and the water vapour is transported through the air.

Based on these assumptions, the primary effect on the governing diffusion mass flux term, \mathbf{j}_{χ_α} , is caused by a concentration gradient or the molecular diffusion flux. Bird et al. [2001] explained that for the case of a two-component ideal mixture, the diffusivity flux, \mathbf{j}_{χ_α} , can be represented by Fick’s Law as

$$\mathbf{j}_{\chi_\alpha} = -\rho D_{\alpha\beta} \nabla \chi_\alpha \quad (3.8)$$

Substituting equation 3.8 into equation 3.7, and in the absence of any chemical reaction, we have

$$\frac{\partial \rho \chi_\alpha}{\partial t} + \nabla \cdot (\rho \chi_\alpha \mathbf{u}) = \nabla \cdot (\rho D_{\alpha\beta} \nabla \chi_\alpha) \quad (3.9)$$

If we express equation 3.9 in terms of ρ_α (see equation 3.6) instead of χ_α , we obtain

- Conservation of Species

$$\frac{\partial \rho_\alpha}{\partial t} + \nabla \cdot (\rho_\alpha \mathbf{u}) = \nabla \cdot \left[\rho D_{\alpha\beta} \nabla \left(\frac{\rho_\alpha}{\rho} \right) \right] \quad (3.10)$$

Equations 3.3, 3.4, and 3.10 are the basic governing equations to be used in the present study. However, some factors, such as turbulence or the presence of a porous medium require additional treatment to include these effects in the transport equations for modelling.

Porous Media Model

As described before, a porous medium is a material formed by a series of pores with irregular shapes and sizes. Therefore, the use of macro, space-averaged properties

that well represent the geometry is a critical issue when representing the porous medium in laminar flows. In order to include the porous media effects, we need to multiply equation 3.10 by the porosity, φ , [Bear, 1988]. In addition, an extra factor, the tortuosity (τ), is needed to account properly for the obstruction caused by the material in the diffusion coefficient [Do, 1998]. As a result we obtain

- Conservation of Species

$$\frac{\partial \varphi \rho_\alpha}{\partial t} + \nabla \cdot (\varphi \rho_\alpha \mathbf{u}) = \nabla \cdot \left[\rho \varphi \tau D_{\alpha\beta} \nabla \left(\frac{\rho_\alpha}{\rho} \right) \right] \quad (3.11)$$

As before, the conservation of momentum also requires certain modifications to include the effects of the porous medium. Joseph et al. [1982] suggests that an appropriate modification of the conservation of momentum is to include new terms into the source term, S_i , in the form

$$S_i = -\frac{\mu}{\varphi K} u_i - c_F K^{-1/2} \varphi^{-2} \rho u_i u_i \quad (3.12)$$

where K is the intrinsic permeability, and φ is the porosity. The first term includes a new viscous forces term, and the second term the inertial forces due to solid obstacles. It is important to mention that the non-linear term of equation (3.12) can be neglected under fairly general assumptions, applicable to this study, such as sufficiently small Reynolds number based on pore or particle diameter. The term “sufficiently small” means that the Reynolds number is of order of unity or smaller [Nield and Bejan, 1999]. This assumption holds for the velocity regimes present in this study, as it will be shown later (see Chapter 5). Consequently, S_i can be written as

$$S_i = -\frac{\mu}{\varphi K} u_i \quad (3.13)$$

Substituting equation 3.13 into equation 3.4, and multiplying again by the porosity, we have

- Conservation of Momentum:

$$\frac{\partial \varphi \rho u_i}{\partial t} + \nabla \cdot (\varphi \rho u_i \mathbf{u}) = -\nabla \varphi p + \nabla \cdot (\varphi \mu \nabla u_i) - \frac{\mu}{K} u_i \quad (3.14)$$

Finally, in presence of a steady-state process, relatively small velocities, and a homogeneous porous medium, equation 3.14 becomes the Darcy's law equation

$$\nabla p = -\frac{\mu L}{\varphi K} u_i \quad (3.15)$$

Turbulence Model

Since, the major events in consideration for the mass transport in the present study are Dust Devils, which are fully turbulent events, the analysis of those effects on the "mean" flow are of the first concern. Therefore, the implementation of a turbulence model is necessary to quantify the flow field at the near surface. Following this concept of mean "quantities", the flow quantity ϕ , which is time dependant, can be written as the sum of a steady mean component Φ and a time-varying fluctuating component ϕ' , for instance, $\mathbf{u} = \mathbf{U} + \mathbf{u}'$. The result of applying this kind of averaging to the conservation equations is the Reynolds Averaged Navier-Stokes (RANS) Equation. However, the RANS models introduce new unknown terms called Reynolds stresses, which produces a system with more unknowns than equations (The Closure Problem). To close these equations, a reasonable approach rests on the concept of Dynamic Turbulent Viscosity or Eddy Viscosity (μ_t), where the Reynolds stresses can be related to the mean velocity gradients, using a direct analogy of the relationship between the stress and strain tensors for Newtonian fluids. A new transport equation for the mean general variable, Φ , of the flow property ϕ , could be defined in order to take into account time average fluctuations due to turbulence [Versteeg and Malalasekera, 1995]

$$\frac{\partial(\rho\Phi)}{\partial t} + \nabla \cdot (\rho\Phi\mathbf{u}) = \nabla \cdot (\Gamma_{\Phi}^* \nabla\Phi) + S_{\Phi} \quad (3.16)$$

Defining Γ_{Φ}^* as

$$\Gamma_{\Phi}^* = \rho D_{\alpha\beta} + \frac{\mu_t}{Pr_t} \quad (3.17)$$

Γ_{Φ}^* involves the turbulence diffusion coefficient, where the first term represents the diffusion process primarily due to the binary molecular diffusivity, and the second

term the diffusion by turbulence processes. Based on the general equation 3.16, equations 3.4 and 3.10 can be adjusted to included the eddy viscosity. In addition, it is important to mention that the present study does not attempt to solve turbulent flows that could be present in the porous medium, in fact, it is assumed that no turbulence is produced inside the porous medium, since the effect of porous medium acts as a damp to the turbulence [Antohe and Lage, 1997].

The $k-\varepsilon$ model has been chosen to assess the first version of the numerical model, due to low costs in terms of computing resources, and because it is the most validated turbulence model. This two-equation turbulence model is based on the assumption that the eddy viscosity through dimensional analysis can be characterized by turbulence kinetic energy, k , a length scale, L , and C a constant of proportionality.

$$\mu_t = C\rho(k)^{1/2}L \quad (3.18)$$

The two-equation model uses the fact that in equilibrium turbulent flows, i.e., flows in which the rates of production and destruction of turbulence are near balance, the energy dissipation, ε , and k and L are related by [Kolmogorov, 1941]

$$\varepsilon \approx \frac{k^{3/2}}{L} \quad (3.19)$$

The standard $k-\varepsilon$ model for a steady-state Newtonian compressible flow is given by Launder and Spalding [1974]:

$$\nabla \cdot (\rho k \mathbf{u}) = \nabla \cdot \left(\frac{\mu_t}{\sigma_k} \nabla k \right) + 2\mu_t S_{ij} \cdot S_{ij} - \rho \varepsilon \quad (3.20)$$

$$\nabla \cdot (\rho \varepsilon \mathbf{u}) = \nabla \cdot \left(\frac{\mu_t}{\sigma_\varepsilon} \nabla \varepsilon \right) + 2C_{1\varepsilon} \frac{\varepsilon}{k} \mu_t S_{ij} \cdot S_{ij} - C_{2\varepsilon} \frac{\varepsilon^2}{k} \quad (3.21)$$

Where

$$S_{ij} = \frac{1}{2} (\partial_i u_j + \partial_j u_i) \quad (3.22)$$

and

$$u_t = \rho C_\mu \frac{k^2}{\varepsilon} \quad (3.23)$$

A second turbulence model, the transient Reynolds Stress Model (RSM) is used in this study, since several major drawbacks of the $k - \varepsilon$ model emerge when it is applied to the simulation of highly rotating flows, such as dust devils vortices [Versteeg and Malalasekera, 1995]. The present study uses a version of the Reynolds stress model developed by Speziale et al. [1991], in which the Reynolds stress transport equation is given by.

$$\frac{\partial (\overline{\rho u'_i u'_j})}{\partial t} + \frac{\partial (u_k \overline{\rho u'_i u'_j})}{\partial x_k} = \frac{\partial}{\partial x_k} \left[\left(\mu \delta_{kl} + c_S \rho \frac{k}{\varepsilon} \overline{u'_k u'_l} \right) \frac{\partial \overline{u'_i u'_j}}{\partial x_l} \right] - \frac{2}{3} \delta_{ij} \rho \varepsilon + \Upsilon_{ij} + \Psi_{ij} \quad (3.24)$$

The terms Υ_{ij} and Ψ_{ij} are the shear turbulence production and quadratic pressure-strain correlation respectively. The detailed meaning of the terms in equation 3.24 can be found in Speziale et al. [1991].

In addition, the RSM uses a transient scheme (Section 3.4), in contrast, with the $k - \varepsilon$ model that is defined as a steady-state process.

3.2.2 Definitions

Water Vapour

Water vapor pressure (p_v) is the fraction of the environment pressure that is due to the fraction of water vapour in the air. Thus, p_v can be expressed as a function of relative humidity (RH), and saturation vapour pressure (p_{sat}), which is the maximum vapor pressure that the air can support, thus:

$$p_v = p_{sat} \cdot RH \quad (3.25)$$

Let assume that the air and the water vapour behave as ideal gases; thus

$$p_v = \frac{\rho_v RT}{M_v}, \quad p_a = p - p_v = \frac{\rho_a RT}{M_a} \quad (3.26)$$

Like ρ , densities ρ_v and ρ_a are defined in terms of mass per unit volume of a fluid mixture so that

$$\rho = \rho_v + \rho_a \quad (3.27)$$

Thus, using the definition of mass fraction (equation 3.6) for water vapour, we have

$$\chi_v = \rho_v / \rho \quad (3.28)$$

Finally, the conservation of water vapour component is given from equation (3.10) and equation (3.28), and assuming that the fluid density, ρ , is constant, we obtain

$$\frac{\partial \rho_v}{\partial t} + \nabla \cdot (\rho_v \mathbf{u}) = \nabla \cdot (D_{va} \nabla \rho_v) \quad (3.29)$$

Binary Diffusion Coefficient

The ability of a single component to diffuse into another it is measured by a constant of proportionality, called binary diffusion coefficient, $D_{\alpha\beta}$. Massmann [1998] proposed an empirical correlation for the air- water vapour diffusion coefficient, D_{va} , which is the fluid mixture used in the present study, and it is given by

$$D_{va}(T, p) = D_{va}(T_0, p_0) \left(\frac{p_0}{p} \right) \left(\frac{T}{T_0} \right)^{1.81} \begin{cases} p \leq 2.53 \cdot 10^6 \text{ Pa} \\ 253 \text{ K} \leq T \leq 373 \text{ K} \end{cases} \quad (3.30)$$

where $T_0 = 273.15 \text{ K}$, $p_0 = 101,325 \text{ Pa}$, and $D_{va}(T_0, p_0) = 2.17 \cdot 10^{-5} \text{ m}^2/\text{s}$. In Martian conditions a different empirical equation must be used.

Porosity

Porosity, φ , is one of the porous media macro physical properties that represents the structure of the medium. This parameter is defined as the ratio of the porous medium volume that is not occupied by the solid phase and the total volume. It is related to the bulk density of the medium, ρ_{pm} , by

$$\varphi = 1 - \frac{\rho_{pm}}{\rho_g} \quad (3.31)$$

where ρ_g is the solid phase average density [Bird et al., 2001].

Permeability

Permeability, K , is another property that defines the structure of the porous medium. This parameter measures the resistance of the medium to the movement of any fluid. Recalling equation 3.15, K is defined as

$$K = -\frac{\mu L}{\varphi \nabla p} u_i \quad (3.32)$$

Tortuosity

Tortuosity, τ , represents the last property used to characterize a porous medium. This parameter stands as the ratio between the straight line of length L_{pm} , connecting the two ends of a tortuous tube of length L_e , and L_e itself. Bear [1988] defined τ average as

$$\tau = \left(\frac{L_{pm}}{L_e} \right)^2 \leq 1 \quad (3.33)$$

3.3 Dust Devils: Kinematic Similarities

This section focuses on the kinematic of dust devils, rather than the dynamic analysis. More specifically, only a small area of the dust devil is relevant for this study, namely, the Corner Flow Region and the Inflow Flow Region (as described in Section 2.2).

Lewellen [1962] described how a three-dimensional steady state, incompressible, axisymmetric vortex flow in a closed cylinder can be characterized by three dimensionless parameters. Lately Davies-Jones [1973] based on the Ward's model chamber [Ward, 1972], redefined these parameters as: Re_r , the radial Reynolds number; S , as the swirl ratio; and a , the aspect ratio

$$Re_r = \frac{\rho r_0 U_r}{\mu} \quad (3.34)$$

$$S = \frac{r_0 U_\theta}{2h U_r} \quad (3.35)$$

$$a = \frac{h}{r_0} \quad (3.36)$$

where r_0 is the radius of updraft, h the depth of the inflow, (as shown in Figure 2.3). In addition, U_θ is the average tangential velocity at r_0

$$U_\theta = \frac{1}{2\pi} \int_0^{2\pi} U_{(\theta, local)} d\theta \quad (3.37)$$

and U_r is the mean radial velocity at the inflow zone at r_0

$$U_r = \frac{1}{2\pi h} \int_0^h \int_0^{2\pi} U_{(r, local)} d\theta dz \quad (3.38)$$

Although axisymmetric flows are relatively easy to achieve in closed cylindrical chambers, this is not always true for natural vortices. Furthermore, the precise definition of these three parameters is not well established for open vortex models. However, some studies have used a quasi-axisymmetric flow as an acceptable condition to apply the Lewellen analysis. For instance, Lewellen and Lewellen [2000] defined an averaged swirl ratio based on net rate of flow into the Corner Region. There is also in the literature, an attempt to define the location of r_0 at the radial location of the maximum absolute value of the radial velocity component based on numerical studies of laminar vortex flows [Wilson and Rottuno, 1982] (see Chapter 5).

In Section 5.4.4, based on the dimensionless parameters S , and a , a characterization of dust devils is presented, by defining the geometrical locations of r_0 and h in turbulent flow regimes. This is done, by solving the governing equations through numerical fluid dynamics calculations for an incompressible, isothermal fluid.

3.4 Computational Fluid Dynamics

In this paper, the numerical simulations were performed using the Computational Fluid Dynamics (CFD) ANSYS/CFX5.7 software package, which is based on the

Finite Volume Method. Following this approach, the equation 3.1 can be rewritten as

$$\frac{\partial}{\partial t} \left(\int_V \rho \phi dV \right) + \int_A \mathbf{n} \cdot (\rho \phi \mathbf{u}) dA = \int_A \mathbf{n} \cdot (\Gamma_\phi \nabla \phi) dA + \int_V S_\phi dV \quad (3.39)$$

where A is the surface of the control volume, and \mathbf{n} is the normal vector to the surface.

Equation 3.39 is the general equation that ANSYS/CFX5.7 uses to solve the flow numerically. The ANSYS [2005] manual reviewed the numerical schemes used in the present study:

- The Second Order Backward Euler scheme. The transient term (equation 3.39) is calculated by this scheme, which is robust, implicit, and second order in time.
- The Upwind Differencing Scheme (UDS) is the most robust scheme used for the advection term, but suffers of high numerical diffusion problems. It is first order in space.
- The Central Differencing Scheme (CDS) is the most accurate scheme used to calculate the advection term; in addition, the numerical diffusion is relatively small. However, for high convection velocities, this scheme presents serious robustness problems. This scheme is second order in space.
- High Resolution [Barth and Jespersen, 1989], this scheme is a blend between the UDS and CDS. This setting introduces a Blend Factor ζ , which varies through the numerical domain, in order to enforce robustness. This factor will be close to 1.0 (CDS) for accuracy wherever small gradients are present, and close to 0.0 (UDS) in areas of high flow gradients, in order to maintain robustness.

Chapter 4

Modelling Setup

Two general types of modelling were conducted for this study, namely: laboratory experiments, and numerical simulations. The laboratory experiments were designed to determine, and to provide significant results of water vapour profiles, vortex flow fields, water losses, and porous medium properties assessment. The tests were conducted at one atmosphere (92,000 Pa), under Earth conditions. The second type includes numerical calculations using the Ward's model geometry, open model case, and other secondary geometries to assess and to validate the theoretical model.

4.1 Laboratory Experiments

All the experimental procedures were conducted in a semi closed environment illustrated in Figure 4.1, which consists of a 6.05 m long x 3.54 m wide x 3.40 m high room. The room presents a quasi-steady air circulation due to the presence of three inflow zones (blue area), and one outlet zone (red area). This process provides a supply of fresh air into the room that keeps the relative humidity levels relatively constant.

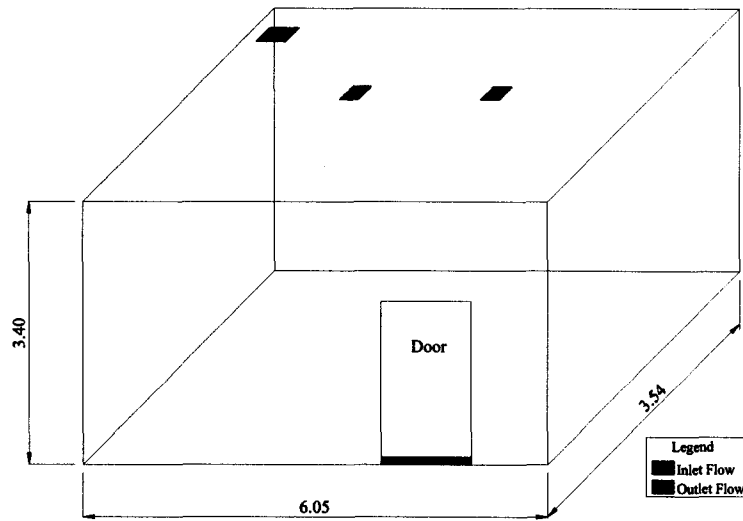


Figure 4.1: Schematic of the Laboratory Environment

4.1.1 Vortex Generator

The main component used to produce dust devils (laboratory scale) is the Vortex Generator Device, which consists of three parts, the frame, the cylinder-electrical motor combination, and the test table (Figure 4.2). The generator is a similar design to the one used by Greeley et al. [2001]. The cylinder-electrical motor combination includes a cylinder 0.45 m in diameter, a motor drive with variable speed, and a four-fan blade system at 90 degrees to each other. This arrangement is mounted to the frame, so that future applications will allow moving the cylinder along the test table to simulate motion of the vortex across the terrain. The table is 2 m x 1 m, and it is detached from the frame to avoid potential motor vibrations.

Figure 4.3 shows a visible dust devil as the white cloud rising from the dry ice container on the test table.

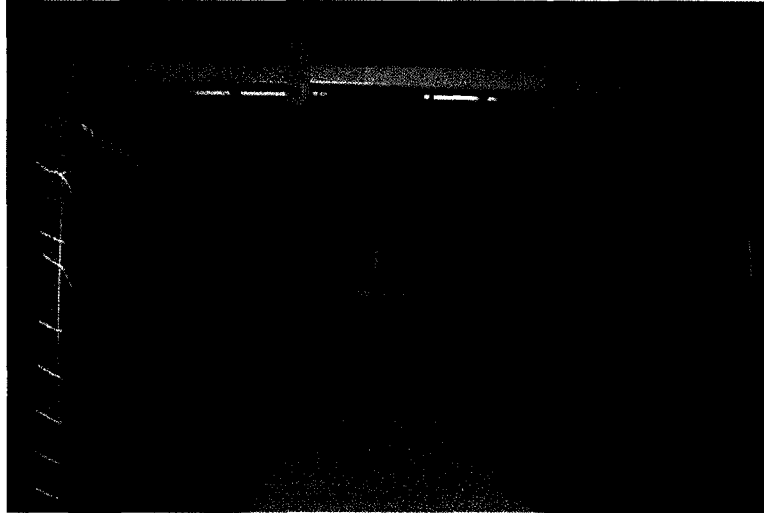


Figure 4.2: The Vortex Generator Device showing the cylinder-electrical motor combination, the frame, and test table.



Figure 4.3: Simulated dust devil created using the vortex generator.

4.1.2 Test Table

The test table described in Section 4.1.1 consists of a water tank, and the porous media (polyurethane foam). The tank is made of a stiff and lightweight aluminium honeycomb panel (2 m long x 1 m wide x 0.14 m deep x 0.025 m thick). It also contains a metallic net to offer foam support to avoid possible deflections in the material (shown in Figure 4.4) and to prevent the foam from touching the water. The foam region is 0.1 m thick, composed of two foam layers of 0.05 m each. The water vapour flux in still air condition is created by a gradient of water vapour concentration from the water reservoir, which is at saturated pressure conditions, and the top of the foam.

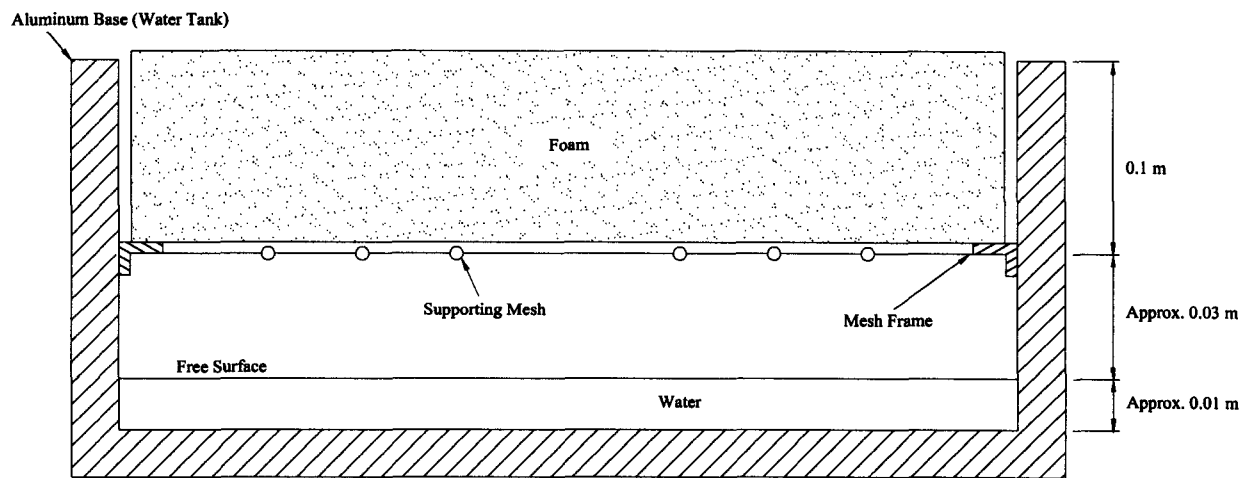


Figure 4.4: Schematic of the test table showing the water reservoir, the porous medium, and the metallic net.

4.1.3 Mini Tank

For transient water vapour flux studies a second experimental setup was used instead of the test table. The mini tank (shown in Figure 4.5) experiment presents better-controlled conditions to assess the increase of water vapour levels in the water reservoir from room values to saturated conditions. This apparatus consists of a water tank

made of acrylic material, a foam region, and an internal plastic lid ($3 \cdot 10^{-3}$ m thick). This lid acts as a physical barrier between the water reservoir and the foam. By removing the lid when the water reservoir reaches equilibrium we are able to measure the time dependent water vapour concentration at the bottom of the foam. This data is subsequently used as a boundary condition for the numerical simulations. This setup is also used to determine the adsorption of water vapour by the foam, as will be explained later. The mini tank dimensions are 0.2 m x 0.2 m x 0.2 m, where the foam thickness is 0.1 m.

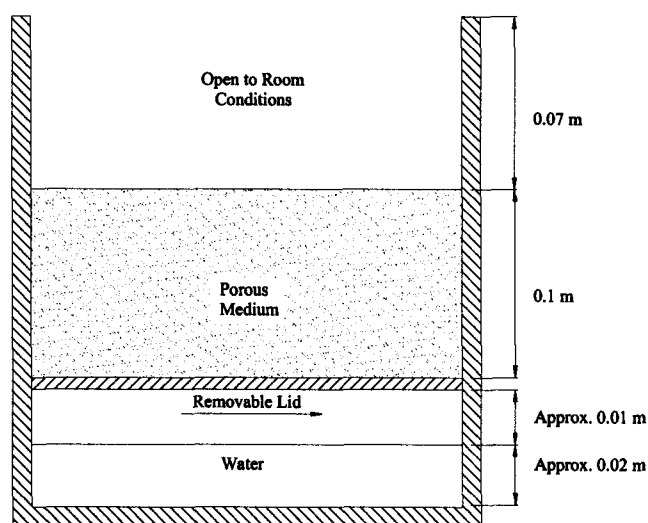


Figure 4.5: Schematic of the transient study showing the water tank, foam and the removable lid.

4.1.4 Intrinsic Permeability

Based on equation 3.12, a third experiment was designed to evaluate the polyurethane foam intrinsic permeability (Figure 4.6). In this test, a prescribed air volume flow is conducted into a plastic tube that contains a foam specimen, in addition, a screen is attached at the beginning of the tube to suppress any eddies from the air supply (Figure 4.7). The pressure drop is varied across the foam by the given air inlet flow. As a result, the permeability is obtained based upon information about the pressure

and velocity profiles. A predefined range of pressure gradients was tested based on typical values present on dust devils [Greeley et al., 2003]. The permeability test dimensions were 0.92 m long x 0.078 m inner diameter, where the distance between the flow screen and the foam was 0.48 m (to avoid any entry effects). In addition, the foam specimen dimensions were selected from recommendations made by ASTM [2003] and Gummaraju et al. [2001].



Figure 4.6: Outside view of the permeability test arrangement.

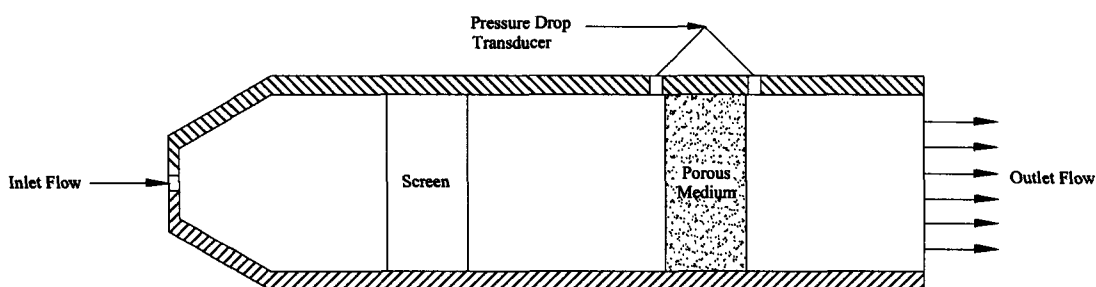


Figure 4.7: Schematic design of the permeability test.

A second experiment designed by Bouzidi [2003] was used to evaluate and to compare the permeability results obtained by the air flow test. However, the transient nature

of this experiment was not suitable to carry out the test using highly porous foam materials.

4.1.5 Porosity

Based on the equation 3.31, the porosity of a polyurethane foam can be determined. The density of the foam, ρ_{pm} , is easily calculated using a normal mass balance. However, the solid material density, ρ_g , needs complex experiments to be defined. The instrument used for this experiment was the multipycnometer [Quantachrome, 2003] as shown in Figure 4.8. This instrument is specifically designed to measure the true volume, and therefore the solid density, of porous materials. The technique employs the relationship $P_\alpha V_\alpha = P_\beta V_\beta$, and the principle of Ideal Gas Law.

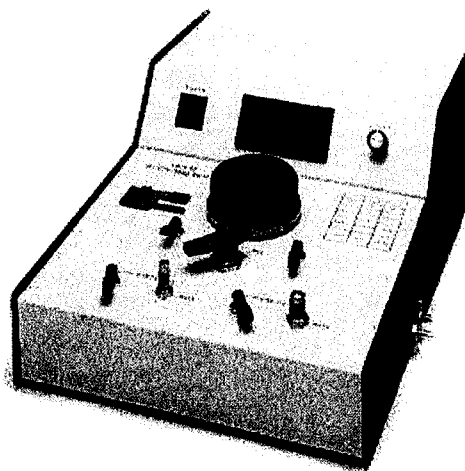


Figure 4.8: Multipycnometer used for the porosity test.

A schematic diagram of the gas multipycnometer is shown in Figure 4.9. It calculates the volume of the foam specimens by measuring the pressure difference when a prescribed inert gas¹ quantity under a positive pressure gradient is allowed to flow from

¹The manufacturer recommends helium since its small molecule dimensions assures penetration into pores approaching one Angstrom (10^{-10}m).

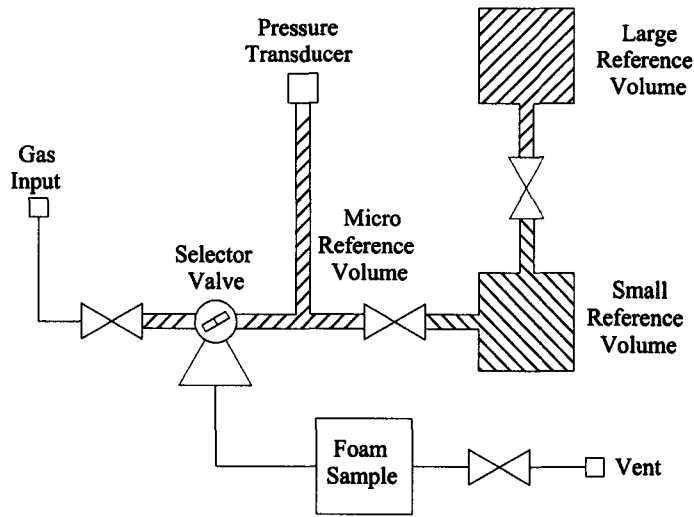


Figure 4.9: Schematic diagram of the Multipycnometer.

a precise reference volume, V_R into the cell that contains the porous material. The governing equation employed for the multipycnometer is given by [Quantachrome, 2003]

$$V_g = V_C - V_R \left(\frac{P_1}{P_2} - 1 \right); \quad \rho_g = \frac{m_g}{V_g} \quad (4.1)$$

where P_1 represents the pressure in the system, and P_2 the pressure when the foam sample is included.

A second experiment using optical evaluation was attempted to measure the porosity of the polyurethane foam. The procedure involved the preparation of foam samples around 100 microns (approximate thickness of one layer of pores). However, this method caused the partial destruction of the foam cells.

4.2 Numerical Simulations

The goal of the computational fluid dynamics simulation is to duplicate a flow field present in nature. Consequently, the methods to achieve these objectives are validate the transport model, create a geometrical domain that reproduces the original

model, and finally compare the numerical values with previous results obtained in laboratory experiments. Different flow and mass transfer problems were simulated with ANSYS/CFX5.7 in the present study, for instance, the Ward's model, the Open model, the test table, and the mini tank.

4.2.1 Ward's Model

The Ward's model of the vortex generation was chosen to validate the numerical turbulence models (Section 3.2.1) used in the present study, since there are many studies on this vortex generator where detailed laboratory data is available. A three dimensional representation of the Ward's model is shown in Figure 4.10. This figure is the numerical domain used to reproduce the flow fields for the Ward's model described in Section 2.2.3. A schematic of the different parameters that define geometrically the Ward's model is shown in Figure 4.11, where r_s is the radius of the convergence zone, r_0 is the updraft hole radius, h is the inflow depth, r_c is the radius of the convection zone, and l is the height of the convection zone (see Figure 2.3 for more details). In Chapter 5, a more complete description of the Ward's model simulated in the present study is introduced, including boundary conditions and exact dimensions.

4.2.2 Open Model

As it was mentioned before, the use of an open vortex generator model brings the option to translate any vortex across the surface of study. The open model used for the present numerical simulation study is a simplification of the vortex generator described in Section 4.1.1. The vortex is created by a rotating wall at the top, which reproduced the rigid solid core rotation present in atmospheric vortices. This wall produces an angular momentum that in theory should be able to create a vortex. Two different domain concepts were employed in the numerical simulations, a rectangular domain (Figure 4.12a), and a circular domain (Figure 4.12b). Both models are designed to study axisymmetric flows behaviour, which is necessary for the proper

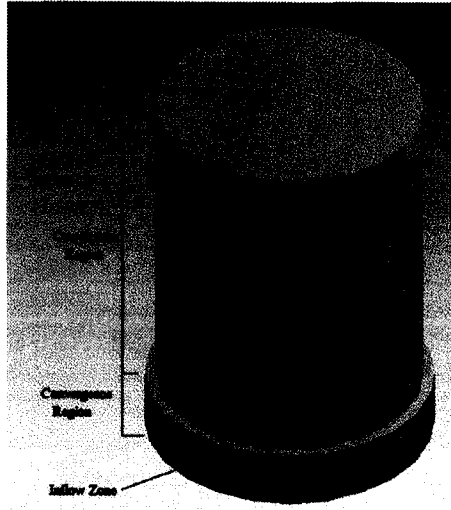


Figure 4.10: 3-D Numerical representation of Ward's Model.

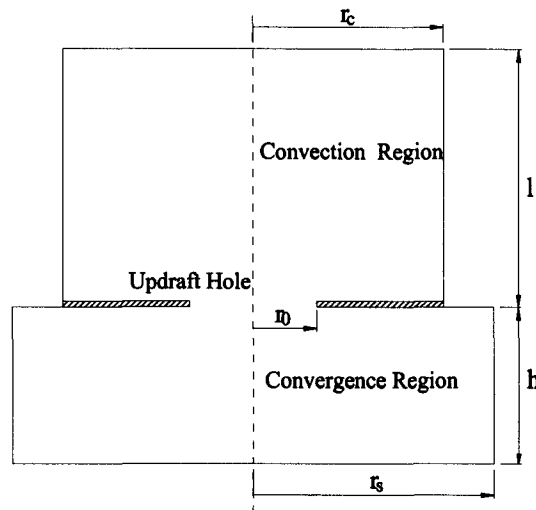


Figure 4.11: Geometric parameters used for Ward's model simulation.

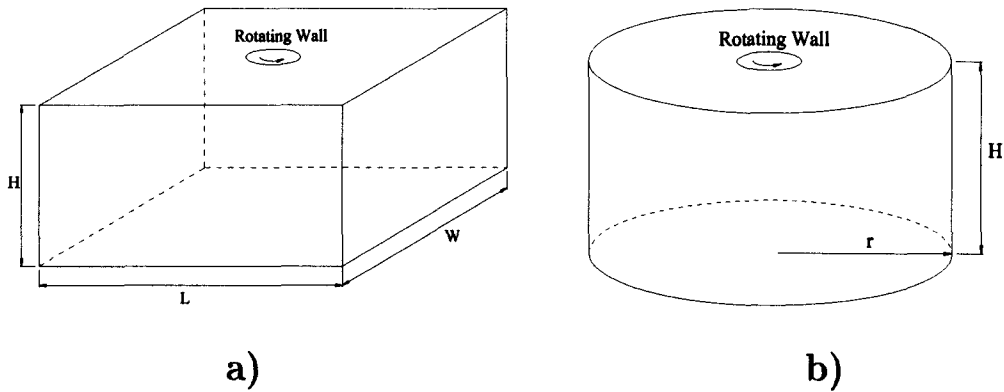


Figure 4.12: Two schematics of open vortex numerical domains: a) rectangular domain, b) cylindrical domain.

characterization of the dust devil. In addition, the walls of both domains are placed far away from the vortex region to avoid any influence in the flow profile. Finally, a third model, representing the actual dimensions of the laboratory room (Figure 4.1), is designed to evaluate the effect of the dust devil over the water vapour flux transport, by adding a representation of the test table (Section 4.1.2) into the numerical domain (Figure 4.13).

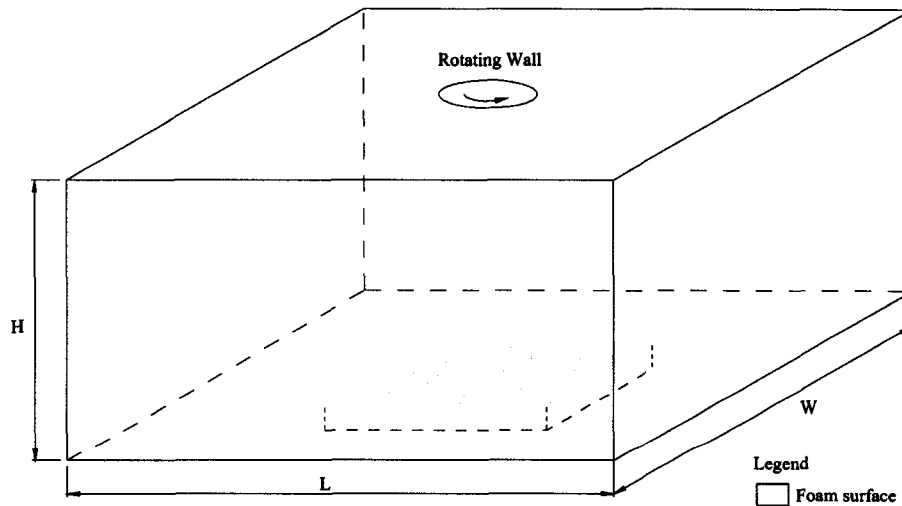


Figure 4.13: Numerical schematic of the Laboratory Open Model including the Test Table.

4.2.3 Test Table and Mini Tank

The numerical model used to represent the test table for quiescent air simulations can be defined as a rectangular shape geometry. The bottom represents the water source (water reservoir), the top is the connection between the foam and the room, and the sides are the walls of the water tank. The dimensions are the same as the real laboratory water tank, which are 2 m x long x 1 m wide and 0.1 m height (foam thickness). The description of the boundary conditions is presented in Chapter 5.

Similar to the numerical test table domain, the mini tank domain represents a simplification of the Mini Tank described in Section 4.1.3, where the bottom represents the water source, the top the intersection between the foam and the room, and the sides represent the walls of the water tank. The dimensions for the mini tank are 0.2 m x 0.2 m x 0.1 m, in accordance with the experiment.

4.3 Instrumentation

The laboratory experiments described above are instrumented to measure ambient temperature, and relative humidity, and weight. The first two measurements, temperature and humidity, involved the use of a dual microsensor manufactured by *Sensirion, model SHT71* (Westlake Village, CA, USA). The weight was measured using an analogical balance manufactured by *Mettler-Toledo, model KCC150* (Columbus, OH, USA), and it was used to measure the water losses of the water tank due to evaporation. An ideal instrument to be used for the present study would be a Laser Doppler Anemometer (LDA). However, the use of this specific instrument for the analysis of the vortex flow fields was not allowed under certain circumstances. Thus, inclusion of a velocity profile characterization of dust devils in the analysis was prevented.

The dual temperature/humidity sensor is a single chip that produces a calibrated digital output. The sensor includes a capacitive polymer element sensitive to relative humidity (range of 0-100%, accuracy $\pm 3\%$ *RH* between 20-80%), and a bandgap temperature device (range 233-393 K, accuracy ± 0.4 K @ 298 K). The balance with capacity of 150 kg and a resolution of 1 g (accuracy ± 3 g @ 50 kg) has four built-in load cells. This device is also calibrated automatically by factory settings. The manufacturer calibration of the T-RH sensors and the balance were verified, as described in Chapter 5.

The parameter time interval measurements and their instrumentation are listed in Table 4.1. The measurement of the relative humidity, temperature, and weight were conducted once every second for experiment 1, and every 60 seconds for experiments 2 and 3 (for details see Chapter 5).

Table 4.1: Measured Parameters and Instrumentation.

Parameter	Instrument	Measuring Interval	Location Point	Experiment No.
Air humidity/Temperature	Dual Sensor	1 s/ 60 s	Point A/B/C/D	1/(2,3)
Foam humidity/Temperature	Dual Sensor	1 s/ 60 s	0 m, 0.05 m, 0.1 m	1/(2,3)
Water	Balance	1 s/60 s	-	1/(2,3)

Chapter 5

Procedures and Results

Theoretical modelling in porous medium, as mentioned before, required the proper definition of its macro properties. The first part of this chapter describes the methodology used to assess the porosity and the permeability of the foam utilized for the mass transport experiments. Next, the values obtained for these parameters are compared with manufacturer's commercial data, in order to validate the experiments carried out on the foam. The second part of this chapter details the procedure followed to determine the water vapour mass flux across the foam under still air conditions, and under the vortex generator effects. This section also presents a comparison with the experimental data obtained and with the theory described before. Finally, the last part of this chapter presents the numerical simulation based on the governing equations (Chapter 3), and their consistency with the laboratory data.

5.1 Porous Medium Properties

5.1.1 Porosity

Following the recommendations of the manufacturer (see Section 4.1.5), helium was used in the multipycnometer. Four samples were used to characterize the porosity of the foam. The samples came from the same polyurethane foam core used for the

mass transfer experiments. The four samples were specimens of irregular shape due to the difficulties of cutting small pieces of regular aspect able to fit in the cylindrical sample cell of the machine, which was 48.98 mm in diameter and 73.95 mm in length. However, an estimate of the volume of each sample can be calculated if the ρ_{pm} of the porous material is known. For this reason, two bigger samples were used to assess ρ_{pm} , one of dimensions 0.05 m x 2 m x 1 m, and other of 0.585 m x 0.510 m x 0.097 m. The balance used was an analog balance of resolution ± 0.1 g (accuracy ± 0.1 g, maximum capacity 4100 g). Table 5.1 shows the values obtained.

Table 5.1: Polyurethane foam bulk density, ρ_{pm} .

Sample	Volume	Weight	ρ_{pm}
1	0.1 m ³	3.272 kg	32.7 kg/m ³
2	0.028 m ³	0.943 kg	33.7 kg/m ³

These values agree well with the density provided by the manufacturer for the polyurethane foam (*Foamex Intl.*, Linwood, PA, USA), which is 32 kg/m³. Using $\rho_{pm} = 33$ kg/m³, based on Table 5.1, and using a more precise balance to determine the four sample weights (accuracy ± 0.002 g, maximum capacity 410 g), the results in Table 5.2 for estimated bulk volume were obtained.

Table 5.2: Multipycnometer foam samples approximate volume.

Sample	Weight	\approx Bulk Volume
1	$2.88 \cdot 10^{-3}$ kg	$8.73 \cdot 10^{-6}$ m ³
2	$3.05 \cdot 10^{-3}$ kg	$9.24 \cdot 10^{-6}$ m ³
3	$2.66 \cdot 10^{-3}$ kg	$8.06 \cdot 10^{-6}$ m ³
4	$2.84 \cdot 10^{-3}$ kg	$8.61 \cdot 10^{-6}$ m ³

The procedure used for the multipycnometer to evaluate the change in pressure was as follows:

1. Air inside the system is removed using a vacuum pump.
2. The system is pressurized approximately to 17 psig¹(11.72·10⁴ Pa).
3. The pressure drop in the system is evaluated when the empty cell sample is connected. This is to check any leak issues. No significant difference in the pressure ratio P_1/P_2 should be found. P_1 and P_2 are the pressure levels with (reference volume) and without the cell sample attached, respectively (see Figure 4.9).
4. The pressure drop is evaluated with a known calibrated spherical volume².
5. The pressure drop is estimated for the samples.

The detailed procedure of the multipycnometer can be found in Quantachrome [2003]. In addition, the experimental data obtained using the procedure described above is presented in Appendix A for all four samples (Tables A.1 to A.6).

Based on equation 4.1, we can calculate the true volume of the foam sample, and therefore, the solid phase average density of the foam. However, two unknowns arise, namely: the reference volume, V_R , and the cell volume sample, V_C . Using the relationship $P_1V_1 = P_2V_2$, it is possible to express V_C in terms of $V_{g\ sphere}$, and therefore, calculate V_R by rewriting equation 4.1 as:

$$V_R = \frac{V_{g\ sphere}}{\left[\frac{P'_1}{P'_2} - 1 \right] - \left[\frac{P_1}{P_2} - 1 \right]} \quad (5.1)$$

where:

- $V_{g\ sphere}$ = volume of the calibration sphere= 56.58·10⁻⁶ m³
- P'_1 = pressure in V_R with no sphere in the cell, Table A.1.
- P'_2 = pressure in V_R and the cell with no sphere in the cell, Table A.1.

¹As recommend by the manufacturer

²Provided by the manufacturer

- P_1 = pressure in V_R with the sphere in the cell, Table A.2.
- P_2 = pressure in V_R and the cell with the sphere in the cell, Table A.2.

A typical calculation for V_R is:

$$V_R = \frac{56.58 \cdot 10^{-6}}{\left[\frac{17.102}{6.409} - 1 \right] - \left[\frac{17.104}{8.423} - 1 \right]} = 88.67 \cdot 10^{-6} \text{ m}^3$$

After solving V_R for all measurements from tables A.1 and A.2, we can use the average of $\overline{V_R} = 88.63 \cdot 10^{-6} \text{ m}^3$ to calculate V_C as (see equation 4.1):

$$V_C = V_{g \text{ sphere}} + \overline{V_R} \cdot \left(\frac{P'_1}{P'_2} - 1 \right) \quad (5.2)$$

For instance, one value for V_C is given by:

$$V_C = 1 \cdot 10^{-6} \cdot (56.58 + 88.63) \cdot \left(\frac{17.102}{6.409} - 1 \right) = 147.95 \cdot 10^{-6} \text{ m}^3$$

and the average $\overline{V_C}$ is $147.94 \cdot 10^{-6} \text{ m}^3$.

Now it is possible to calculate the true volume of the samples (equation 4.1). For example, for sample 1:

$$V_{g1} = \overline{V_C} - \overline{V_R} \cdot \left(\frac{P^*_1}{P^*_2} - 1 \right) \quad (5.3)$$

where:

- P^*_1 = pressure in V_R with no sample in the cell, Table A.3.
- P^*_2 = pressure in V_R and the cell with the sample in the cell, Table A.3.

Therefore:

$$V_{g1} = 1 \cdot 10^{-6} \cdot (147.94 - 88.63) \cdot \left(\frac{17.110}{6.486} - 1 \right) = 2.76 \cdot 10^{-6} \text{ m}^3$$

The average true volume, $\overline{V_g}$, for each sample and its respective weight is shown in Table 5.3:

Table 5.3: Average density obtained using the polyurethane foam.

Sample	V_g	Weight	$\bar{\rho}_g$
1	$2.710 \cdot 10^{-6} \text{ m}^3$	$2.88 \cdot 10^{-3} \text{ kg}$	1063 kg/m^3
2	$2.879 \cdot 10^{-6} \text{ m}^3$	$3.05 \cdot 10^{-3} \text{ kg}$	1059 kg/m^3
3	$2.547 \cdot 10^{-6} \text{ m}^3$	$2.66 \cdot 10^{-3} \text{ kg}$	1044 kg/m^3
4	$2.659 \cdot 10^{-6} \text{ m}^3$	$2.84 \cdot 10^{-3} \text{ kg}$	1068 kg/m^3

Finally the solid phase average density of the foam that allows us to determine the porosity (equation 3.31) of the porous media is given by the average of the values presented in Table 5.3, which is $\rho_g=1059 \text{ kg/m}^3$. As we expected, this density is much higher than the bulk material, which is 33 kg/m^3 , since it does not include the void space in the material. Therefore, the porosity of the polyurethane foam used in the present study is given by:

$$\varphi = 1 - \frac{33}{1059} = 0.97$$

By definition the porosity of a material varies between $0 \leq \varphi \leq 1$, for open cells, where 0 corresponds to a solid material, and 1 for a gas. Based in this concept, we can infer that the polyurethane foam used for the present study is a highly porous material. This means that the resistance in the binary diffusion coefficient offered by the foam is almost negligible in comparison with the binary diffusion coefficient in air. This does not mean that the molecular diffusion in the foam has to be necessarily similar to the molecular diffusion in air, since other factors to be explained later in this chapter are involved in the water vapour transport (see Section 5.3.2). In addition, the value calculated above, $\varphi = 0.97$, is consistent with typical range values of porosity in polyurethane foams, which are $0.924 \leq \varphi \leq 0.975$ [Hebner, 1995].

In Section 3.2.1, we assumed that the mean free path was much smaller than the geometrical length scale where the molecule travels through. Even though this approach has little or no relation with the porosity assessment, the definition of the geometrical length scale does, since it is defined as the average pore diameter. For this reason, the proof of this assumption is included here.

The Knudsen number, K_n is defined as the ratio of the mean free path, λ , and the average pore diameter, L_{pd} [Mills, 2001]. Moreover, K_n determines the degree of rarefaction of the gas and the validation of the continuum flow assumption. For $Kn \leq 0.001$ the continuum hypothesis is appropriate [Barber and Emerson, 2002] and the flow can be analyzed using the equations 3.3, 3.4, and 3.10. From the above, we have:

$$K_n = \frac{\lambda}{L_{pd}} \quad (5.4)$$

For the standard atmospheric air conditions, $\lambda = 5 \cdot 10^{-8} \text{m}$ [Kundu, 1990]. For the case of L_{pm} , a simple experiment was conducted to evaluate the diameter of the pores. Table 5.4 shows the diameter of several pore sizes at the edge of two foam samples obtained using a scaled microscope.

Table 5.4: Typical pore diameters for a polyurethane foam.

Sample	Diameter [mm]	Sample	Diameter [mm]
1	0.264	5	0.526
2	0.502	6	0.492
3	0.358	7	0.379
4	0.597	8	0.498

Therefore, the average pore size, or L_{pm} is equal to 0.452 mm ($4.52 \cdot 10^{-4} \text{ m}$), and the corresponding value of K_n is:

$$K_n = \frac{5 \cdot 10^{-8}}{4.52 \cdot 10^{-4}} = 1.11 \cdot 10^{-4}$$

since K_n is smaller than 0.001, we can infer that the continuum approach holds for the present study (no slip-flow regime present, Section 2.1.1). and that molecular diffusion as the unique diffusion process. In addition, since the mean free path is four orders of magnitude smaller than the average pore diameter, the assumption that Knudsen diffusion can be neglected for mass transport modeling is also valid.

5.1.2 Permeability

Using the experiment described in Section 4.1.4, we were able to assess the intrinsic permeability, K , of the material for a steady-state flow for relatively small velocities ($\approx 5 \cdot 10^{-2} \text{m/s}$), based on equation 3.12. Two extra instruments were used to conduct the experiment needed to determine K :

- A pressure transducer to evaluate the static pressure difference between both sides of the foam (see Appendix A).
- A volume flow transducer to assess the volumetric rate into the cylinder (also Appendix A).

Two additional experiments were needed to determine the calibration curve for the pressure transducer and the volume flow transducer. Procedure and data values are presented in Appendix A.

Figure 5.1 represents the calibration curve of the pressure transducer using data from Table A.7 (see Appendix A). As expected, ΔP is a linear function of the voltage.

Based on Figure 5.1, equation 5.5 was constructed using a polynomial fit of first degree (linear regression) and it shows the relationship of ΔP as function of the voltage, thus:

$$\Delta P = 249.08 \cdot (0.1143 \cdot \text{Voltage} - 0.2968) \quad [\text{Pa}] \quad (5.5)$$

Figure 5.2 represents the calibration curve of the volume flow transducer using data from Table A.8 (see Appendix A). The curve was also constructed using a polynomial fit of first degree. As expected, the volume flow as function of the voltage is linear as well.

Based on Figure 5.2, the relationship of the volume flow rate, V_F , as function of the

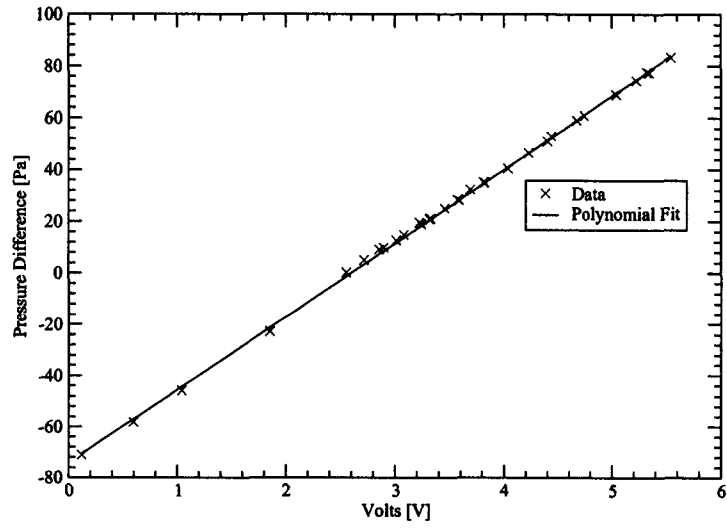


Figure 5.1: Calibration curve of the pressure transducer.

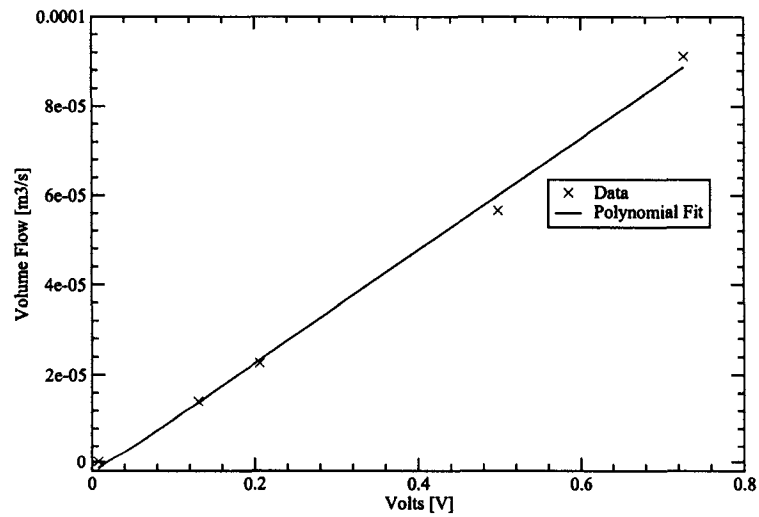


Figure 5.2: Calibration curve of the volume flow transducer.

voltage is given by:

$$V_F = 1.25 \cdot 10^{-4} \cdot \text{Voltage} - 2.42 \cdot 10^{-6} \quad [\text{m}^3/\text{s}] \quad (5.6)$$

Using a needle valve to regulate the volume introduced to the volume flow transducer described above, we were able to determine the pressure drop between four different foam samples (see Figure 4.7). The dimensions of the samples were:

Table 5.5: Permeability sample dimensions.

Sample	Diameter [m]	Length [m]
1	$78.62 \cdot 10^{-3}$	0.5
2	$79.42 \cdot 10^{-3}$	0.5
3	$78.85 \cdot 10^{-3}$	0.5
4	$79.15 \cdot 10^{-3}$	0.5

It is important to mention that for this experiment the range of pressure difference to be assessed was $0 \text{ Pa} \leq \Delta P \leq 60 \text{ Pa}$, since these are the typical pressure drop values expected inside dust devils generated in laboratory [Greeley et al., 2001], and therefore, the gradient pressure involved in the advection flux process for the water vapour flux.

Based on equation 3.12 it is possible to determine the intrinsic permeability of the foam used, by evaluating the pressure drop across the porous medium as a function of the velocity inside the foam, V . Figure 5.3 represents the laboratory values of ΔP against V (Table A.9, see Appendix A) for the foam samples described above.

From Figure 5.3, the assumption that the non-linear term in equation 3.12 can be neglected is clearly valid (see Section 3.2), since the pressure difference profile can be represented by a linear function of the form:

$$\Delta P = m \cdot V \quad (5.7)$$

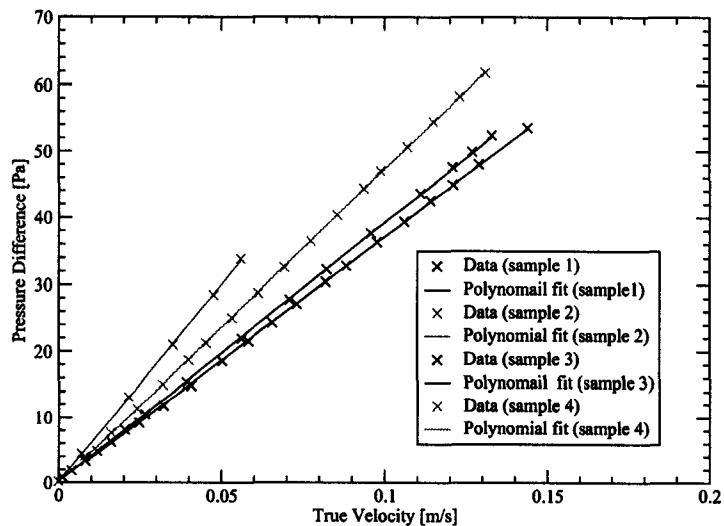


Figure 5.3: Permeability test results.

where m is the slope of the curve. Recalling equation 3.15, m is defined as $m = \mu/K$.

Even though pressure gradients are slightly different in Figure 5.3, this study assumed the foam as a homogenous material. The reason for this particular approach is that the foam edges in sample 2, during the experiment, could be subjected to compression, due to the plastic tube, which could reduce the foam permeability to the air movement [Gummaraju et al., 2001]. Consequently, only samples 1, 3, and 4 were taken into consideration to determine the permeability, where each individual K was calculated using a polynomial fit of first order. Furthermore, channelling effects were avoided in the permeability experiments by ensuring that no gap between the tube and the foam sample existed. This was possible by cutting the foam 1 mm bigger than the internal diameter of the tube. Therefore, the permeability used for the numerical simulations is an average of these three samples, i. e.

$$\bar{K} = 2.22 \cdot 10^{-9} \text{m}^2$$

assuming an air viscosity $\mu = 1.85 \cdot 10^{-5} \text{ Pa} \cdot \text{s}$ [Mills, 2001].

The intrinsic permeability can also be defined in terms of the saturated per-

meability, as described in Chapter 2. Therefore, K can be written as:

$$K = \frac{K_s \cdot \mu}{\rho \cdot g} \quad (5.8)$$

where K_s is the saturated permeability. μ , ρ , and g are the dynamic viscosity, the density, and gravity respectively. The equation described above is useful since in the literature sometimes the permeability is expressed in terms of the saturated permeability instead of the intrinsic permeability. If we consider water at 298.15 K as the working fluid through the polyurethane foam, the saturated permeability that corresponds to $K = 2.22 \cdot 10^{-9}$ is equal to (using equation 5.8):

$$K_s = \frac{K \cdot \rho \cdot g}{\mu} = \frac{2.22 \cdot 10^{-9} \cdot 997.13 \cdot 9.81}{8.91 \cdot 10^{-4}} = 0.024 \text{ m/s}$$

This value is in agreement with the range present by Foamex [1999], which is $0.020 \text{ m/s} \leq K_s \leq 0.040 \text{ m/s}$ for liquid water.

5.2 Data Acquisition

The procedure to obtain the water losses was quite simple, since the balance used to measure the weight for the experiments was equipped with its own built-in data interface. This device sends all the weight measurements directly to a computer serial port. In addition, the balance came with a fully internal auto-calibrated system tested in the laboratory with standard weights of 1 kg and 50 kg. However, for the data acquisition from the dual temperature/relative humidity sensors, there was a need to design a computer code able to request and store the data from the dual sensors. A simple experiment was conducted to validate the accuracy of these measurements and to identify errors in the data acquisition code.

The use of saturated salt solutions is a convenient method to calibrate humidity sensors, since the relative humidity of the solution does not depend on the temperature significantly. The use of this method allowed us to check the accuracy of the relative humidity part of the sensor. In addition, a thermocouple was used to determine if

the temperature sensor part was also measuring correctly. The salt solution used was Potassium Carbonate with a relative humidity, RH , of 43.16 %. The solution was enclosed in a sealed glass with four sensors and a thermocouple wire. Figures 5.4 and 5.5 show the values of RH and T , respectively.

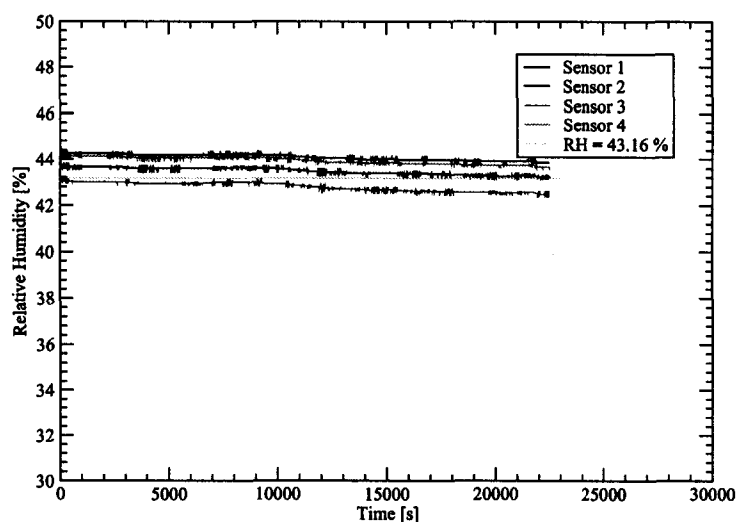


Figure 5.4: Calibration of Relative Humidity Sensors.

From Figures 5.4 and 5.5 we can determine that the RH and T average absolute error of the four sensors is 0.59 % RH and 0.54 K. These results are fully consistent within the sensor accuracy specifications.

Finally, an experiment to assess the relative humidity time response of the dual sensors was conducted using two different saturated solutions. First, the sensor was introduced in a sealed glass containing Lithium Chloride solution ($RH = 11.31\%$) until it reached steady state. Next, the sensor was placed in a high water concentration container with Sodium Chloride solution ($RH = 75.29\%$). The values obtained are shown in Figure 5.6.

From these results shown in Figure 5.6, the time response of the sensors is 5.3 s ($1/e$,

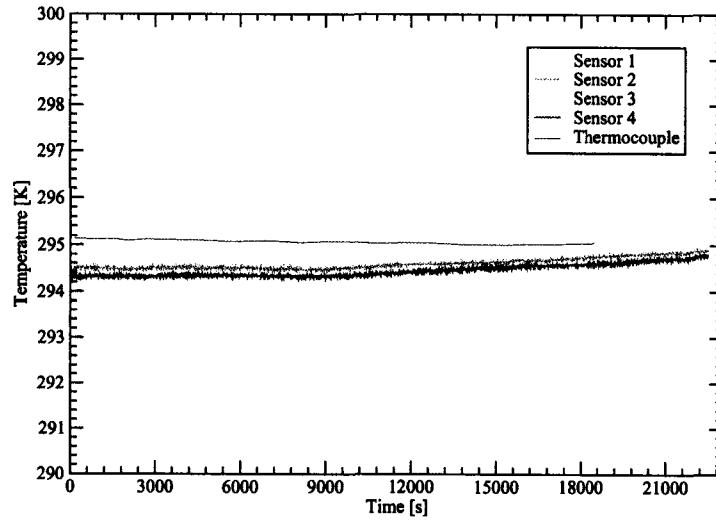


Figure 5.5: Calibration of Temperature Sensors.

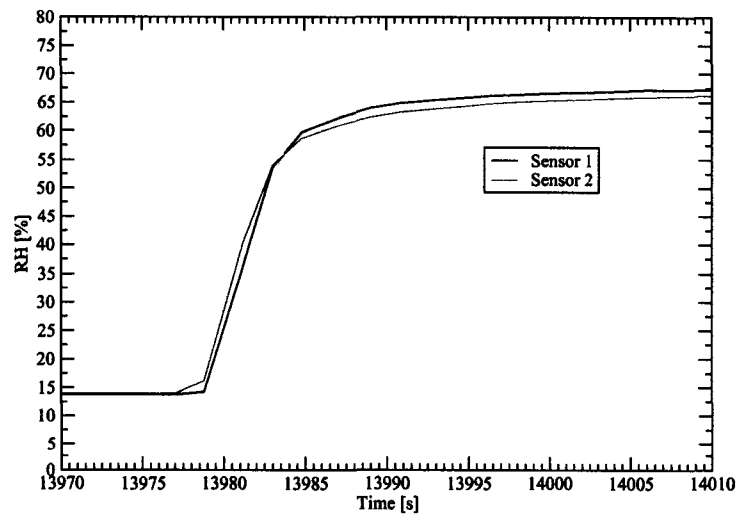


Figure 5.6: Time Response for the Relative Humidity Sensors.

63%), which agree quite well with the specifications provided by the manufacturer of 4 s on slowly moving air.

5.3 Mass Transport Experiments

This section describes the procedures used to assess water vapour losses due to evaporation and the results obtained using the test table, the mini tank, and the vortex generator described before. More importantly, these experiments were carried out to determine the ability of the model of conservation of species (Section 3.2) to predict and to quantify the water vapour transport process in still air conditions, and under the influence of a laboratory vortex or a mini dust devil.

5.3.1 Test Table

The test table was used to determine the foam influence in the water vapour transport due to evaporation, as described in Chapter 4. Three experiments were conducted to analyse the humidity, temperature and water losses in steady state conditions. The procedure was as follows:

- The balance was levelled horizontally using its own levelling bubble system device.
- The test table was placed on top of the balance without any type of external support except for the balance itself. It is important to mention that since the balance has an effective surface support of 0.8 m long x 0.6 m wide, which is much smaller than the test table, it was necessary to centre the table on top of the balance to avoid any possible deflection of the water tank.
- Once the table was in place, the tank was filled with distilled water.

- After introducing the water in the tank, a second levelling procedure was required. Basically, the water level was inspected using two small sticks marked with measurements. Thus, because the balance legs influenced water level, they were adjusted to obtain similar water heights along the tank.
- After levelling the water tank, two layers of foam were placed inside, above the water level. The foam has one sensor at the lower surface, one at the interface between them, and one at the upper side. All the sensors were placed at the centre of the foam area, which was at 0.5 m and 1 m from tank walls.
- In order to assess the boundary conditions to be implemented in the numerical simulations, four sensors were also placed at the centre of the laboratory room walls and above experimental setup (see Figure 4.1).
- The experiment consisted a time record of RH , T , W_i , where W_i represents the instantaneous water weight during the experiment.

The next section describes the values obtained for each of the three experiments. As a final note, the use of relative humidity as a variable of study has been used for the following experiments because of the assumption made of isothermal conditions.

Experiment 1

From Figure 5.7 we can assume that the steady state condition has been reached at $6 \cdot 10^4$ s, since the water relative humidity levels are reasonably constant. The temperature across the foam is considered isothermal since the temperature difference is only two degrees (Figure 5.8). Therefore, in order to determine the mass water losses due to evaporation, we can calculate the slope in Figure 5.9 from $6 \cdot 10^4$ s until the end of the experiment, which is $2.26 \cdot 10^5$ s, thus:

Water weight @ $6.00 \cdot 10^4$ s; $W_0 = 16.000$ kg

Water weight @ $2.26 \cdot 10^5$ s; $W_1 = 15.197$ kg

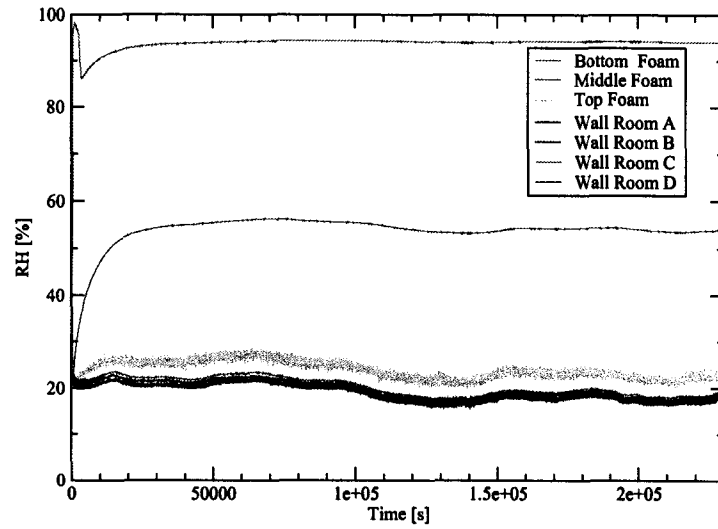


Figure 5.7: Relative humidity profiles as a function of time.

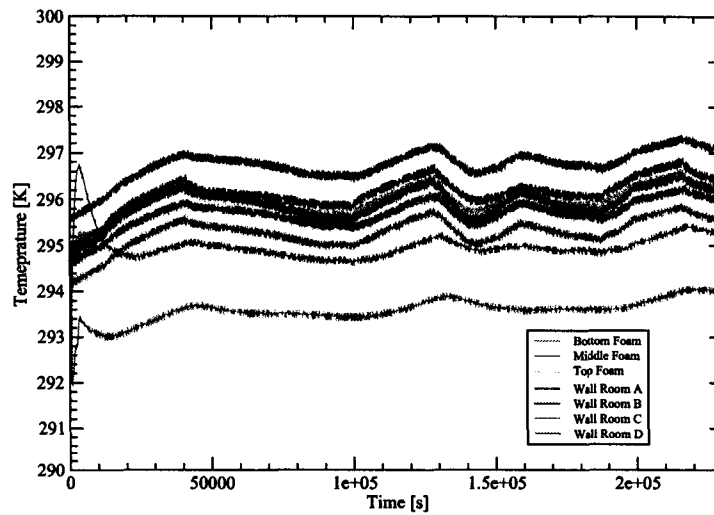


Figure 5.8: Temperature profiles as a function of time.

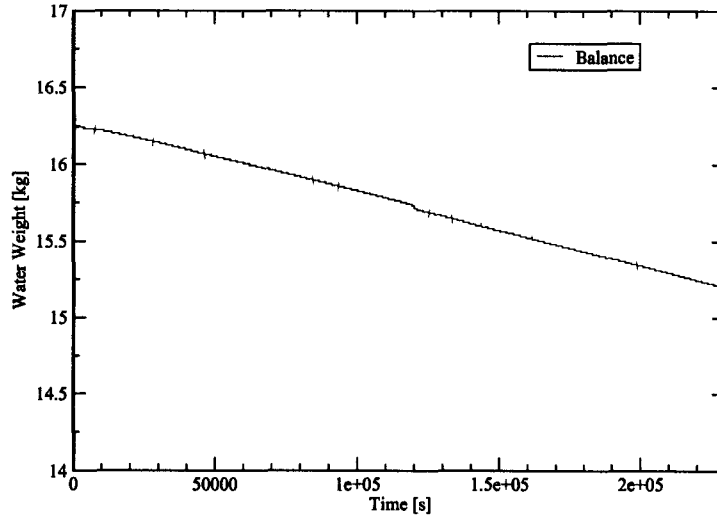


Figure 5.9: Water loss profile as a function of time.

Therefore, the water vapour losses rate, \dot{m} , is:

$$\dot{m} = \frac{W_1 - W_0}{t_1 - t_0} = \frac{15.197 - 16.000}{2.26 \cdot 10^5 - 6 \cdot 10^4} = -4.84 \cdot 10^{-6} \text{ kg/s}$$

where the negative sign represents the water loss from the water tank. Finally, the water loss per unit area (total area, 2 m²) is

$$\dot{m}_A = \frac{\dot{m}}{A} = \frac{4.84 \cdot 10^{-6}}{2} = 2.42 \cdot 10^{-6} \frac{\text{kg}}{\text{m}^2 \cdot \text{s}}$$

Now, considering equation 3.29 as a particular case of the conservation of species from porous media, equation 3.11, as explained before, we have:

$$\frac{\partial \varphi \rho_v}{\partial t} + \nabla \cdot (\varphi \rho_v \mathbf{u}) = \nabla \cdot (\varphi \tau D_{va} \nabla \rho_v) \quad (5.9)$$

Since the experiment is for steady state condition and still air, equation 5.9 becomes:

$$0 = \nabla \cdot (\varphi \tau D_{va} \nabla \rho_v) \quad (5.10)$$

If we integrate equation 5.10 across the foam, and considering a 1-D problem, we can express equation 5.10 as the Fick's law equation for porous medium (see equation 3.8):

$$\dot{m}_A = \varphi \tau D_{va} \frac{\Delta \rho_v}{\Delta z} \quad (5.11)$$

The water concentration, ρ_v , can be obtained from Figure 5.7 using the time average of the sensors at the bottom and top of the foam (see equations 3.25 and 3.26). The value Δz is the thickness of the foam 0.1 m. Hence:

Water vapour concentration bottom:

$$\bar{\rho}_{z0} = \frac{\overline{RH}_{z0} \cdot \rho_{sv}(\bar{T})}{100} = \frac{94.12 \cdot 0.02}{100} = 1.78 \cdot 10^{-2} \text{kg/m}^3$$

Water vapour concentration top:

$$\bar{\rho}_{z1} = \frac{\overline{RH}_{z1} \cdot \rho_{sv}(\bar{T})}{100} = \frac{23.48 \cdot 0.02}{100} = 4.44 \cdot 10^{-3} \text{kg/m}^3$$

where $\rho_{sv}(\bar{T})$ represents the saturated water vapour concentration at specific temperature, which is a function of the average temperature in the foam, \bar{T} . From Figure 5.8, $\bar{T} = 294.70$ K. ρ_{sv} is determined from tables of saturated vapour in air [Mills, 2001], we have:

$$\rho_{sv} = 0.02 \text{ kg/m}^3$$

The diffusion coefficient D_{va} was obtained using equation 3.30:

$$D_{va} = 2.17 \cdot 10^{-5} \left(\frac{294.70}{273.15} \right)^{1.81} = 2.45 \cdot 10^{-5} \text{m}^2/\text{s}$$

Finally, using Fick's law (equation 5.11) we can estimate the last of the properties of the porous medium, the tortuosity:

$$\tau = \frac{\dot{m}_A \cdot \Delta z}{\Delta \rho_v \cdot \varphi \cdot D_{va}} = \frac{2.42 \cdot 10^{-6} \cdot 0.1}{(1.78 \cdot 10^{-2} - 4.44 \cdot 10^{-3}) \cdot 0.97 \cdot 2.45 \cdot 10^{-5}}$$

$$\Rightarrow \tau = 0.76$$

which satisfies the definition where $\tau \leq 1$ (see Section 3.2.2).

The following experiments (2 and 3) were repeats of experiment 1 for longer periods (6 days instead of 2.5). The repeats were used to verify foam properties and to ensure stability of the mass water vapour flux in steady state conditions, and zero wind velocity.

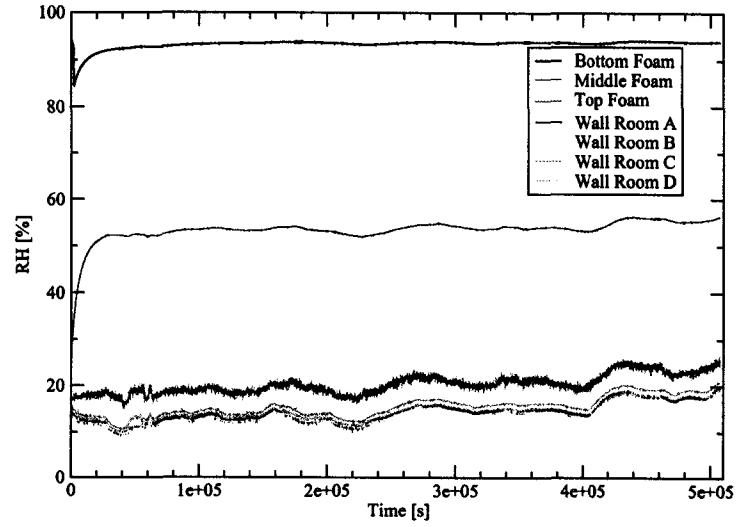


Figure 5.10: Relative humidity profiles as a function of time.

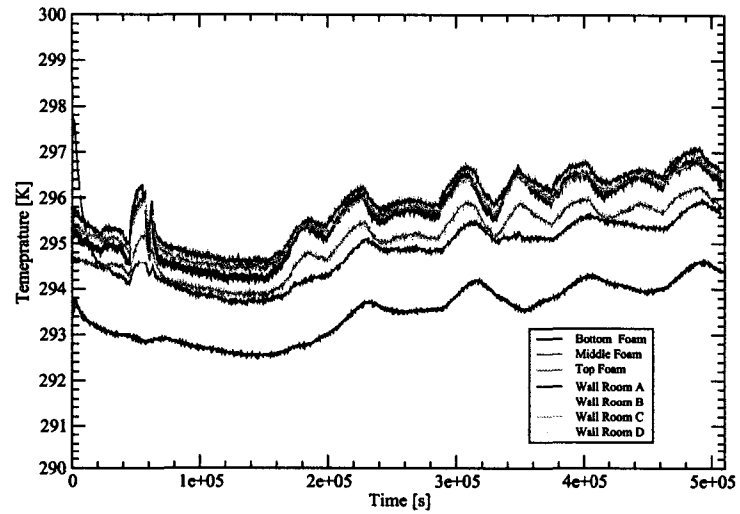


Figure 5.11: Temperature profiles as a function of time.

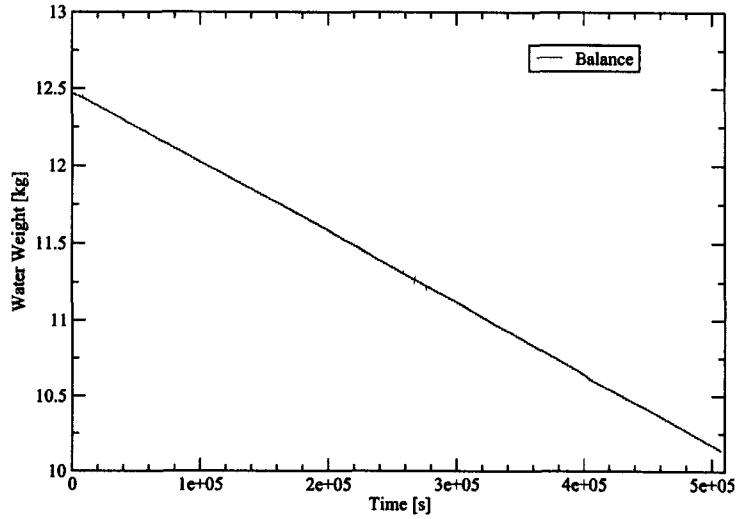


Figure 5.12: Water loss profile as a function of time.

Experiment 2

As in experiment 1, from Figure 5.10 we can assume that the steady state conditions are reached at $6 \cdot 10^4$ s, where the final time is $5.07 \cdot 10^5$ s. Therefore, \dot{m} is (from Figure 5.12):

$$\dot{m} = -\frac{W_1 - W_0}{t_1 - t_0} = \frac{10.138 - 12.202}{5.07 \cdot 10^5 - 6 \cdot 10^4} = 4.62 \cdot 10^{-6} \text{ kg/s}$$

and per unit area:

$$\dot{m}_A = 2.31 \cdot 10^{-6} \text{ kg/s}$$

Using equation 5.11 and values from Figures 5.10 and 5.11 to estimate the tortuosity as in experiment 1, we have:

$$\tau = \frac{2.31 \cdot 10^{-6} \cdot 0.1}{(1.78 \cdot 10^{-2} - 3.91 \cdot 10^{-3}) \cdot 0.97 \cdot 2.45 \cdot 10^{-5}} = 0.70$$

As we can see the difference to the tortuosity estimate in experiment 1 is only 8%.

Experiment 3

As with the previous experiments, from Figure 5.13 we can assume that the steady state condition is reached at $6 \cdot 10^4$ s, where the final time is $5.35 \cdot 10^5$ s. Therefore, \dot{m}

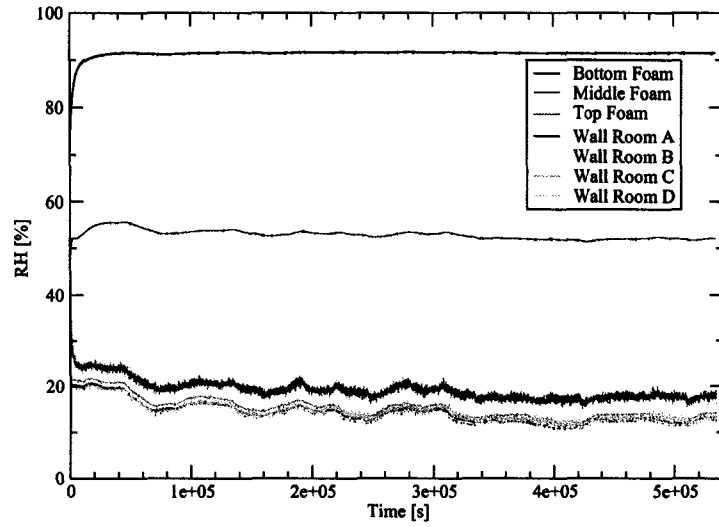


Figure 5.13: Relative humidity profiles as a function of time.

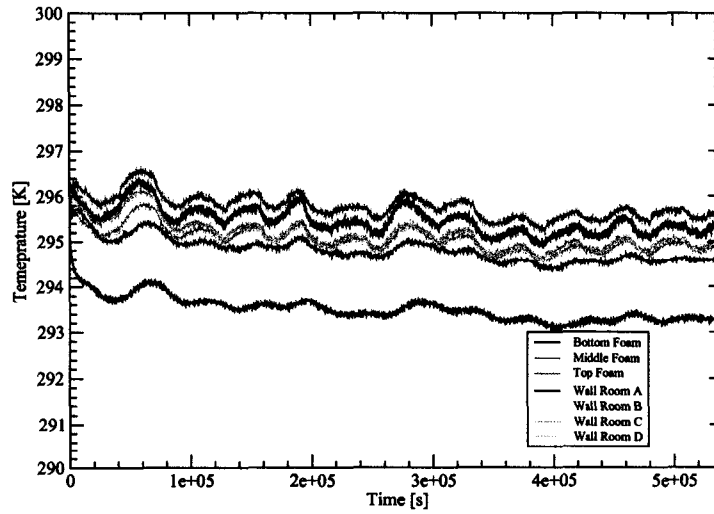


Figure 5.14: Temperature profiles as a function of time.

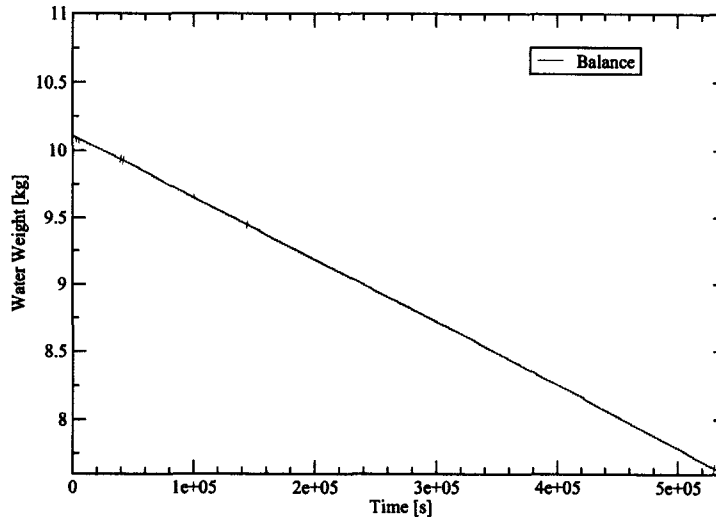


Figure 5.15: Water loss profile as a function of time.

is (from Figure 5.15):

$$\dot{m} = -\frac{W_1 - W_0}{t_1 - t_0} = \frac{7.62 - 9.84}{5.35 \cdot 10^5 - 6 \cdot 10^4} = 4.68 \cdot 10^{-6} \text{ kg/s}$$

and per unit area:

$$\dot{m}_A = 2.34 \cdot 10^{-6} \text{ kg/s}$$

Using equation 5.11 and values from Figures 5.13 and 5.14 to estimate again tortuosity, we have:

$$\tau = \frac{2.34 \cdot 10^{-6} \cdot 0.1}{(1.71 \cdot 10^{-2} - 3.49 \cdot 10^{-3}) \cdot 0.97 \cdot 2.45 \cdot 10^{-5}} = 0.72$$

As we can see the difference to the tortuosity result in experiment 1 is only 5%.

Summary

The results show that steady-state conditions can be obtained after approximately 16 h and that experimental conditions can be maintained stable for many days. A small variation ($\approx 5-8\%$) in the estimate of tortuosity between the three runs was observed. Fick's law (equation 5.11) describes the test data quite well, as expected. Based

on this finding, the molecular diffusion can be viewed as the dominant mechanism of diffusion. Moreover, the assumption that thermal diffusion can be neglected is validated, since it represents no appreciable influence in the total mass transport phenomena. This condition supports the idea that relatively small changes in low temperature environments have no effect over the diffusion process. However, the present study does not imply that Fick's law is strictly obeyed on high temperature regions, for instance, boiling conditions.

5.3.2 Mini Tank

The mini tank set-up was used to assess the transient effects on the water vapour transport under better-controlled laboratory conditions. Two experiments were conducted to determine the humidity-temperature profiles. Several sensors were placed inside the mini tank, for instance, top water level, bottom foam, middle foam, top foam, top tank, and three extra sensors attached at the walls of the room. The experimental procedure was as follows:

- Filling the bottom of the tank with water.
- Closing the water source with the removable impermeable lid (see Figure 4.5).
- Placing both foam layers on top of the lid. No need of support for the foam was required this time.
- The lid was removed when the water source (top water sensor) reached saturated conditions ($\approx 100\% RH$), exposing the foam layers to the water vapour.
- Immediately after removal of the lid, data acquisition was started to record RH , T , W_l .
- The experiment was stopped when values reached steady state conditions.

These experiments were conducted to provide the numerical simulations with transient results to be included as boundary conditions at the bottom of the foam. Figures 5.16 and 5.17 represent the transient profile of RH over time for experiment 4 and 5 respectively.

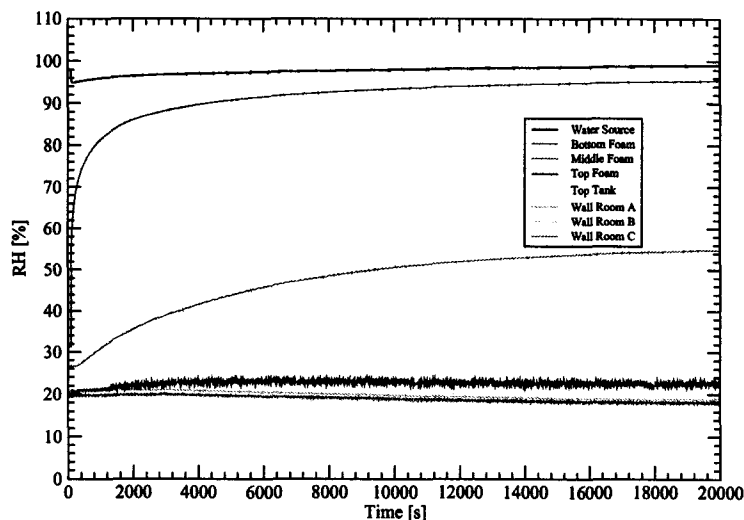


Figure 5.16: Transient RH profiles of experiment 4.

As expected, the transient profiles in the RH for both experiments behaved in a similar manner. As soon as the lid is removed, a drop in the levels of humidity on the water source is observed. This can be explained due to the fact that the water vapour pressure needs to balance the gradient created in the air gap and in the bottom part of the foam. It can also be observed that the water humidity levels at the bottom of the foam increase almost immediately. However, further inspection in Figures 5.16 and 5.17 brings up certain issues about the water vapour profile behaviour. Figure 5.18 represents a shorter period of time study.

From Figure 5.18 we can observe a significant delay (≈ 600 s) in the increment of water vapour in the middle of the foam layers after the bottom starts increasing its humidity levels. Even though the foam should introduce a certain degree of resistance to the

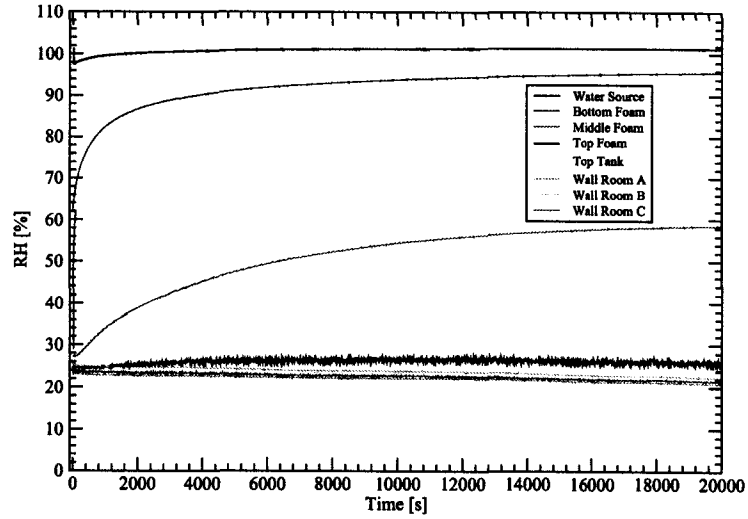


Figure 5.17: Transient RH profiles of experiment 5.

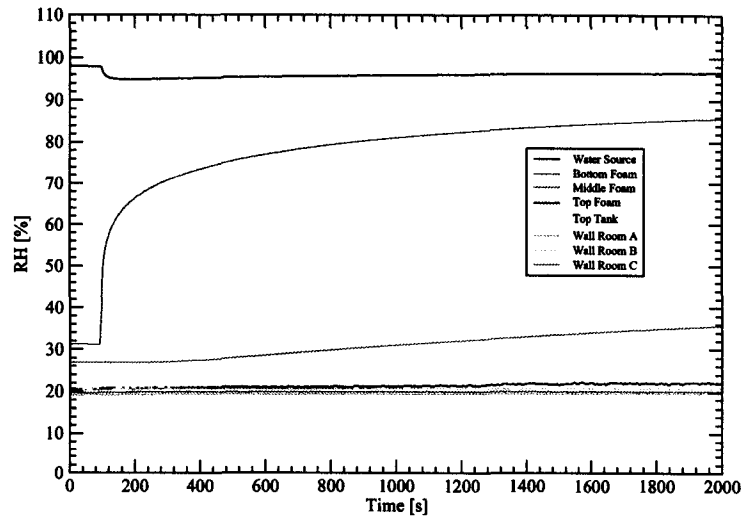


Figure 5.18: Relative humidity profiles as a function of time (shorter study).

water vapour transport (as it was mentioned in Section 5.1.1), this big difference in vapour concentration time response may not be due to different diffusion coefficient values. It was hypothesised that an extra source of resistance to the mass transport in the foam, which was not included in the governing equations, could be affecting the general transient behaviour of the experiment. The following experiment was designed to test if this source could be caused by an adsorption mechanism within the porous material.

Two foam samples were subjected to two different humidity conditions. A “dry state” environment at 16.04% *RH*, and a second state, “wet state”, at 66.30% *RH*. Basically each foam was introduced in the mini tank under these two environments for 6 hours and their final weight was determined. Table 5.6 shows the summary of the experiment (see Appendix A, Table A.10 for details).

Table 5.6: Water adsorption on polyurethane foams.

Sample	66.30% <i>RH</i>	16.04% <i>RH</i>	Difference
1	74.210 g	72.984 g	1.226 g
2	75.324 g	74.565 g	0.759 g

The significant increase in the foam sample weights (Table 5.6), even though the difference in weights are not similar between samples, confirms the hypothesis described above, where an extra term in the conservation of species (equation 5.9) would be need in case of transient simulations. However, it is not the objective of the present study to go further into the study of adsorption analysis, but to demonstrate that the material retains water vapour, thus explaining the behaviour seen in the initial phase of the Mini tank tests. As a result of this, the use of a different non-adsorptive porous material would be recommended to assess the consistency of the transient theoretical model with experimental data, without requiring introduction of an extra source term. Finally, these observations do not affect the present steady state studies, since once the porous medium has reached a “saturated” adsorption level, the resistance

to the water vapour diffusion will correspond to a regular porous medium.

The second variable studied on the transient process in the mini tank was the temperature. Figures 5.19 and 5.20 present the data obtained.

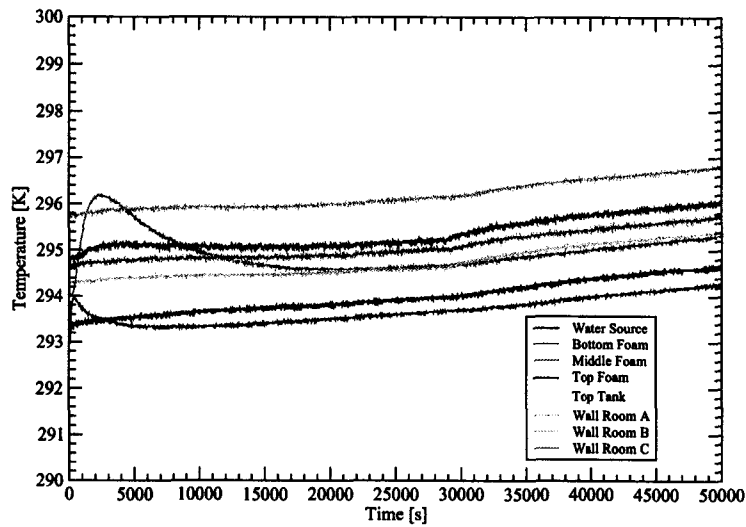


Figure 5.19: Transient T profiles of experiment 4.

Figures 5.19 and 5.20 show a substantial temporary increase in the middle sensor and the bottom temperature sensors of 3 and 1 K, respectively. This increase in the temperature responses can be explained by the exothermic nature of the adsorption process in the foam [Gülseren et al., 2001], where the strength of the adsorptive bonds is directly proportional to the heat dissipated by the adsorption process. This explains the higher temperature registered in the middle of the foam compared with the bottom, since the heat generated within the foam cannot easily dissipate to the surroundings. In fact, the increment of the temperature in the foam confirms that the strong adsorption process that is present in the material is causing the delay in the water vapour levels at the middle sensor location.

In spite of this, Figure 5.21 (experiment 4, bottom sensor) shows that small tem-

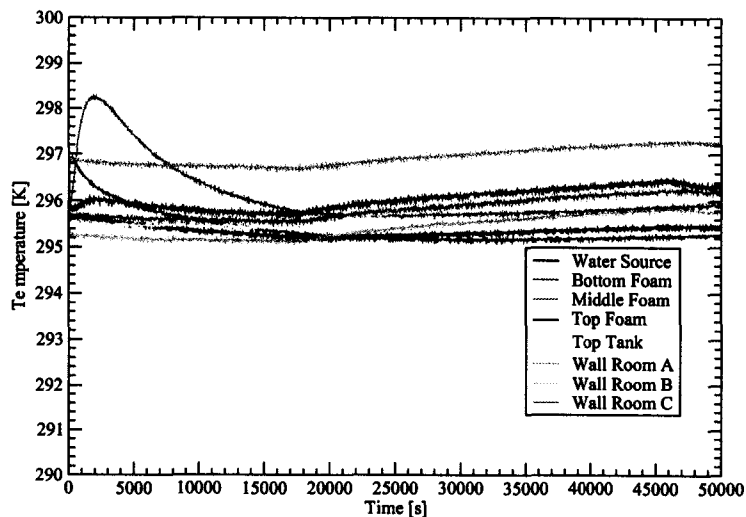


Figure 5.20: Transient T profiles of experiment 5.

perature variations do not affect the general molecular diffusion process, as it was mentioned in Section 5.3.1.

5.3.3 Laboratory Air Circulation

The second uncertainty is the water vapour profile at the top of both foam and tank. Even though there is a continuous increase of the RH levels of vapour inside the foam, the RH at these locations remains relatively constant. In fact, the water vapour levels are quite similar to the ones at the wall locations in the room (Figures 5.16 and 5.17). This effect is observed in Figures 5.7, 5.10, and 5.13. A reasonable explanation for this behaviour is that the experiments were not conducted in perfectly still air conditions. A small current of fresh air with low RH at the surface of the foam maintains the water vapour concentrations at constant levels. In other words, a slow convection process is present in the laboratory (see Figure 4.1). Table 5.7 shows volume flow and RH air measurements made at different lab openings that validate this assumption.

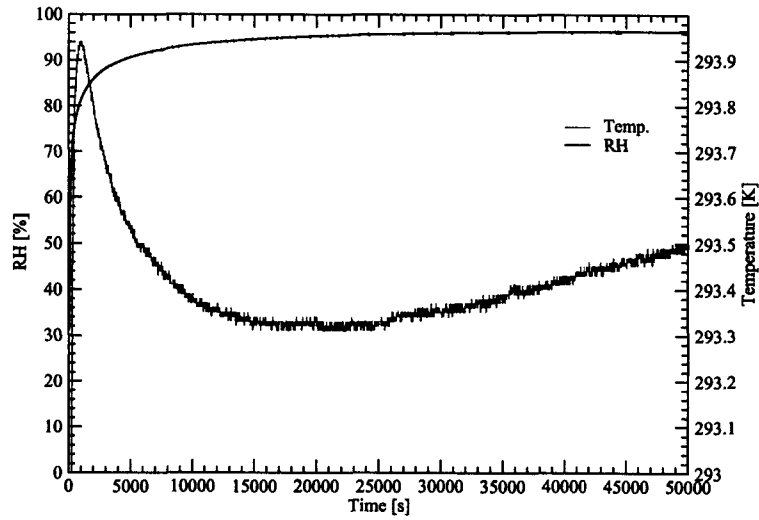


Figure 5.21: Relative humidity profiles as a function of time.

Table 5.7: Approximate volume flow and RH at lab openings.

Location	Volume Flow	RH
Door Gap	$2.35 \cdot 10^{-4} \text{ m}^3/\text{s}$	16.15%
Right Hole	$4.00 \cdot 10^{-2} \text{ m}^3/\text{s}$	15.20%
Left Hole	$4.00 \cdot 10^{-2} \text{ m}^3/\text{s}$	14.30%
Exhaust	$-8.02 \cdot 10^{-2} \text{ m}^3/\text{s}$	18.15%

As Table 5.7 shows, a source of fresh air is introduced into the room maintaining the water vapour levels relatively constant. In Section 5.4.3 further analysis of this process will be presented.

5.3.4 Vortex Generator

In order to assess the influence of turbulent vortex flows on the water vapour rate, three experiments were conducted. The procedure was as follows:

- The set-up for the test table was the same as described in Section 5.3.1 (still air case).
- The vortex generator was started when relative humidity steady state conditions over the test table were reached, after approximately 16 hours (Figure 5.7).
- The rotation of the vortex generator was set to 1750 RPM.
- Finally, the data acquisition was started to record RH , T , W_l . Time measurement were performed at intervals of 1 s for experiment 6 and 60 s for experiment 7.
- The experiments were carried out until RH reached steady state conditions again.

Experiment 6

The following figures present the values obtained for water vapour mass flux under the influence of a laboratory dust devil.

From Figure 5.22 we can assume that the steady state condition has been reached at 5035 s, since the water relative humidity levels show a reasonably constant average. The mass water losses due to evaporation were calculated based on Figure 5.24 from

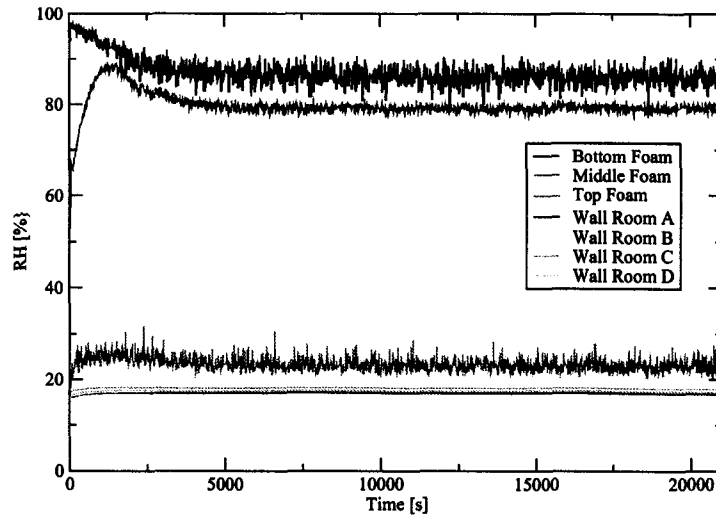


Figure 5.22: Relative humidity profiles as a function of time.

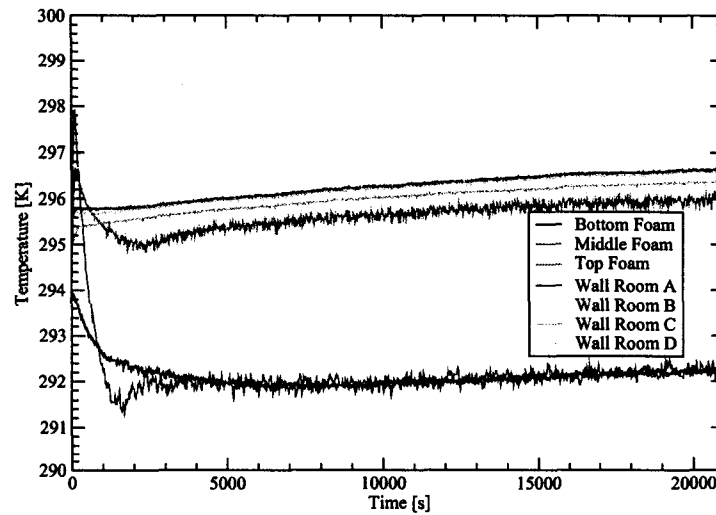


Figure 5.23: Temperature profiles as a function of time.

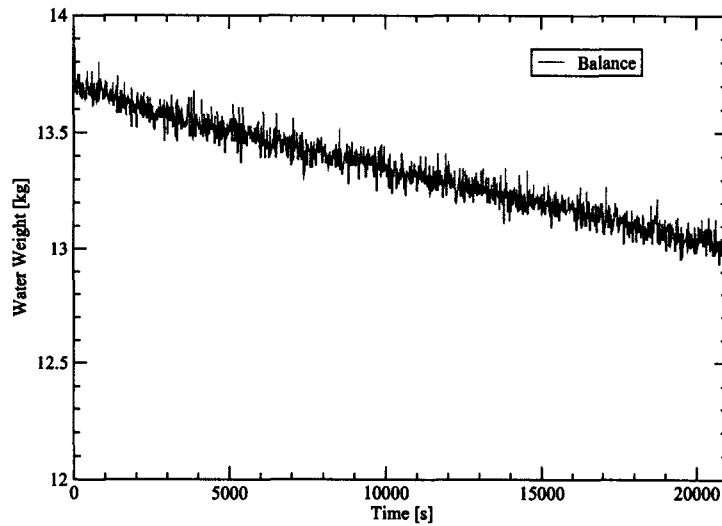


Figure 5.24: Water loss profile as a function of time.

5035 s until the end of the experiment, which was 20818 s, thus:

Water weight @ 5035 s; $W_0 = 13.56$ kg

Water weight @ 20818 s; $W_1 = 12.97$ kg

Therefore, the water vapour losses rate, \dot{m} , is:

$$\dot{m} = -\frac{W_1 - W_0}{t_1 - t_0} = \frac{12.97 - 13.56}{20818 - 5035} = 3.74 \cdot 10^{-5} \text{ kg/s}$$

Finally, the water loss per unit area (total area, 2 m^2) is:

$$\dot{m}_A = \frac{\dot{m}}{A} = \frac{3.74 \cdot 10^{-5}}{2} = 1.87 \cdot 10^{-5} \frac{\text{kg}}{\text{m}^2 \cdot \text{s}}$$

The water losses due to the vortex influence in comparison with still air increased from $2.42 \cdot 10^{-6} \text{ kg/m}^2 \cdot \text{s}$ for still air (see Section 5.3.1) to $1.87 \cdot 10^{-5} \text{ kg/m}^2 \cdot \text{s}$ in the presence of the vortex. This significant increase in the water vapour mass flux rate is a response to the introduction of an advective flux from the bottom of the foam towards the surface caused by the low pressure of the dust devil core. Moreover, a second mechanism that might also influence this increment is the absorption of moisture in the air that travels below the foam parallel to the water source. This moisturized airflow then moves towards the centre of the foam. This increment can also be explained mathematically due to the new mass transport term, which is a

convective mechanism, present in the governing equation of a species (Equation 3.29).

The three-dimensional nature of the equation described above requires the use of a numerical simulation to solve it. This is because the assumption of Fick's Law is no longer valid. Another reason is that the velocity gradients are not themselves constant along the surface of the foam, particularly due to the vortex. This is in contrast with the still air case.

Aside from these results, other features can be extracted and differentiated between still air and dust devils conditions. From Figure 5.23 we can observe the increment of the middle foam humidity levels from values around 60% (Section 5.3.1) to 80%. This demonstrates that the humidity gradient is not longer linear, because of the additional convection transport. In addition, a temperature difference of 2 K between the bottom of the foam and the top is also observed. This difference might be caused by the cooling effect of water phase change due as the air flows in the air gap towards the centre of the vortex. However, this effect may vanish while the flow approaches the surface, because of the influence of the surrounding room temperature conditions at the foam top surface.

Experiment 7

From Figure 5.25 we can assume that the steady state condition has been reached at 5028 s. The mass water losses due to evaporation were calculated based on Figure 5.27 from 5028 s until the end of the experiment, which was 190363 s, thus:

Water weight @ 5035 s; $W_0 = 7.28$ kg

Water weight @ 20818 s; $W_1 = 2.73$ kg

Therefore, the water vapour losses rate, \dot{m} , is:

$$\dot{m} = -\frac{2.73 - 7.28}{190363 - 5028} = 2.46 \cdot 10^{-5} \text{kg/s}$$

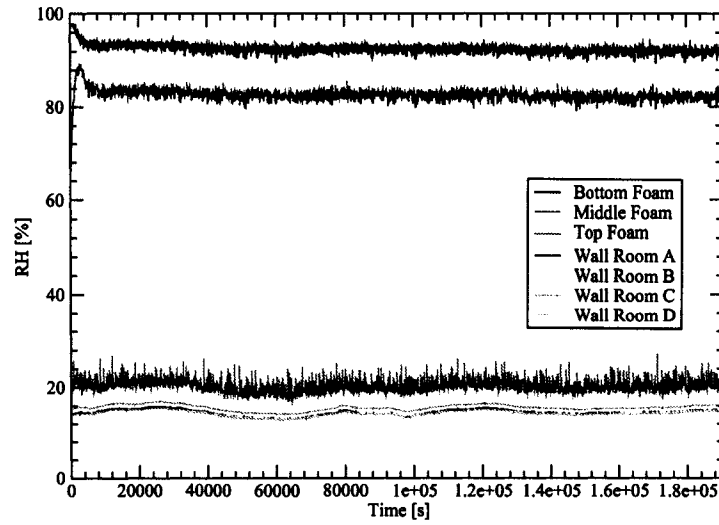


Figure 5.25: Relative humidity profiles as a function of time.

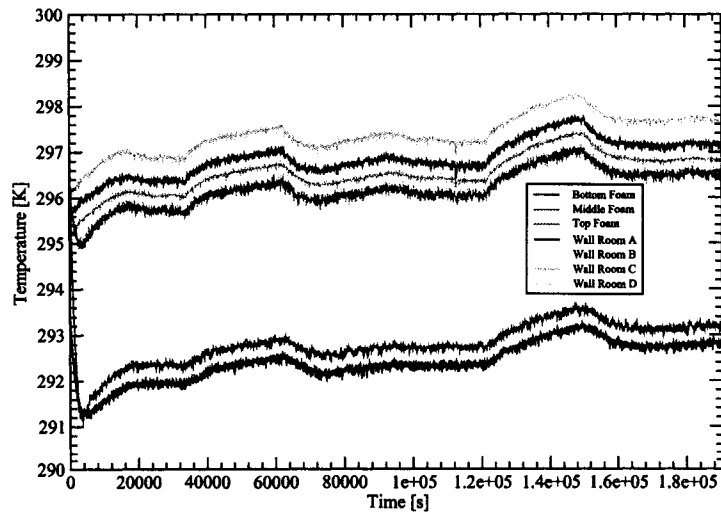


Figure 5.26: Temperature profiles as a function of time.

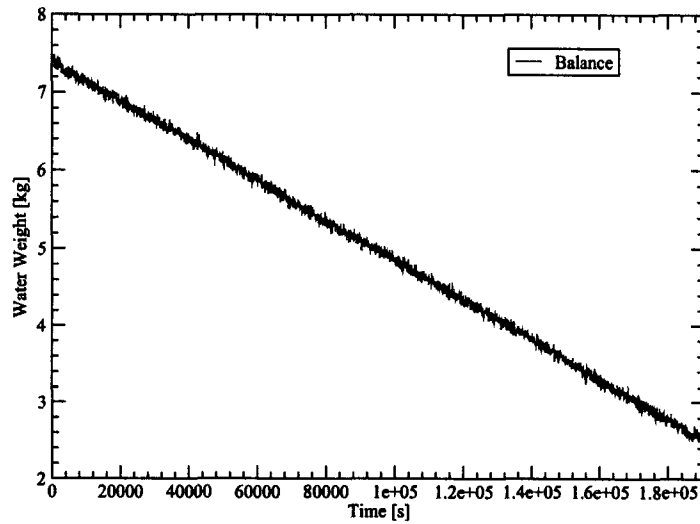


Figure 5.27: Water loss profile as a function of time.

Finally, the water loss per unit area (total area, 2 m²) is:

$$\dot{m}_A = 1.23 \cdot 10^{-5} \frac{\text{kg}}{\text{m}^2 \cdot \text{s}}$$

As it is observed, experiment 7 is in good agreement with the values obtained in experiment 6. Moreover, similar temperature and humidity profiles are observed in both graphs.

Summary

Vortex flows (0.1 m radius) over porous regions (2 m x 1 m) with water reservoirs have a large impact on water vapour flux rates. The results suggest that the flux rate is 5 to 7 times larger than in still air case. Based on these values, the advection flux due to velocity profiles generated by the vortex can be described as the dominant mechanism of mass transport through the foam, with more predominance than the molecular diffusion. More importantly, dust devils can be an important factor in local water vapour mass flux rates from the regolith to the Martian atmosphere, considering the higher velocities, and pressure gradients that these atmospheric events can produce.

5.4 Numerical Simulations

This section describes the procedure and results of the CFD study to analyze the diffusion, water vapour advection flux, and vortex flows using laminar and the standard $k - \varepsilon$, and Reynolds stress models (RSM) of turbulence. The simulations were performed in transient mode for the RSM, and in steady state mode for laminar and the $k - \varepsilon$ turbulence model to validate the theoretical models with the experimental data.

In the numerical simulations presented below, an unstructured mixed element mesh was created using the fully automated mesh generation tool WORKBENCH from ANSYS. Different mesh controls were implemented to produce fine mesh elements to obtain desirable stability and convergence wherever it was needed. The use of non-orthogonal elements allows for a fast setup of the problem, requiring only few parameters as input, for instance:

- Minimum and maximum lengths of the element mesh. These parameters control the range size of the element created by the mesh generator and must be proportional in size to the full-length scale of the numerical domain.
- Mesh control elements. In order to create refined regions in a numerical domain, CFX use numerical devices such as line or point controls. These features establish a second set of element mesh usually smaller than the core mesh in order to capture small flow field fluctuations.

All of the numerical simulations to be described below were conducted using a mesh sensitivity analysis to ensure that the numerical results were not affected by the mesh design.

5.4.1 Test Table

In a first step to verify the correct implementation of the water vapour mass transport theoretical model in the CFD code, a test table simulation, as described in Chapter 4, was conducted. The numerical domain consisted of the foam region only and it was defined with a zero velocity field and steady state conditions. Moreover, no particular mesh control was used, but a same size element mesh (Figure 5.28).

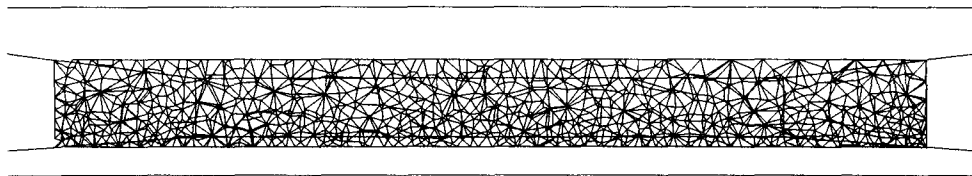


Figure 5.28: Unstructured mixed element mesh used for the discretization of the test table at mid plane.

The boundary conditions at the walls of the test table were set up as zero flux for the relative humidity, RH and no-slip for velocities. The top and bottom of the domain were prescribed at $RH_1=18.74\%$, and $RH_2=94.12\%$ (from experimental data, Section 5.3.1). In addition, the model was considered isothermal and laminar. The porous medium was numerically defined based on equation 3.13 using the permeability and the porosity obtained from the experiments described in Section 5.1. Finally, the model used the central differencing scheme for conduction, and a global normalized residual of 10^{-6} as the convergence criteria. Figure 5.29 presents the relative humidity contour along the foam obtained in the simulation.

From Figure 5.29, due to the fact that the mass flux is constant along the test table (1D movement), it is expected that a proportional decrease of RH further goes away from the water vapour source. This gives an indication that the water vapour concentration gradient is constant, as Fick's law predicts, where a linear humidity profile (water vapour concentration) should be expected.

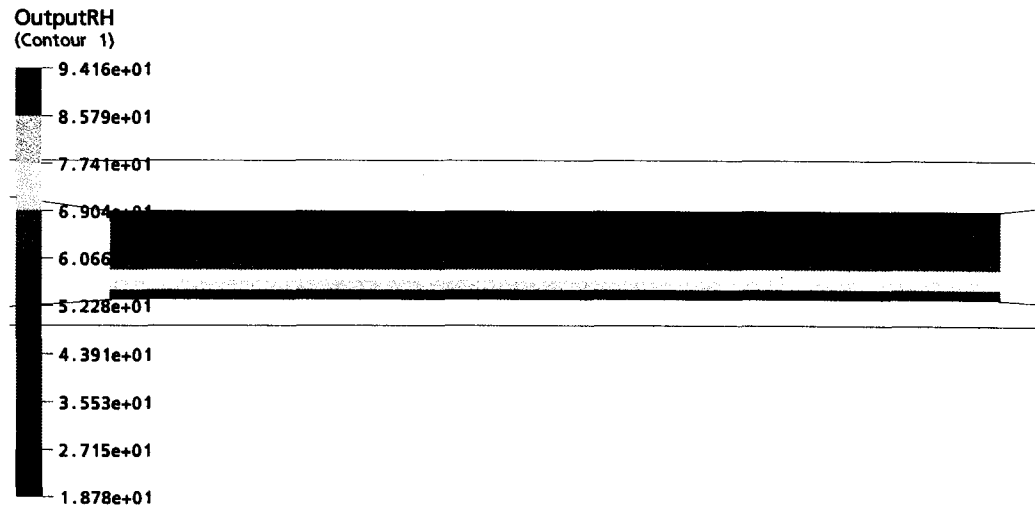


Figure 5.29: Contour of water vapour relative humidity in mid plane of the test table

Figure 5.30 illustrates a comparison between the numerical simulation and the experimental data obtained in experiment 1 (Section 5.3.1). It confirms the linearity of the water vapour mass flux behaviour. Equally important is the quantitative analysis of the mass flux rate per unit area calculated by CFX, $\dot{m}_A = 2.42 \cdot 10^{-6} \text{ kg/m}^2 \cdot \text{s}$, which for this case results in similar values as obtained in experiment 1. These results suggest the correct definition of Fick's law in the numerical code.

5.4.2 Mini Tank

A second numerical analysis to assess and to validate the still air case with unsteady water vapour concentration measurement is described. As mentioned before, the mini tank experiment was used to achieve a better control of the boundary conditions at the bottom of the foam. As in the case of the test table, a numerical domain repre-

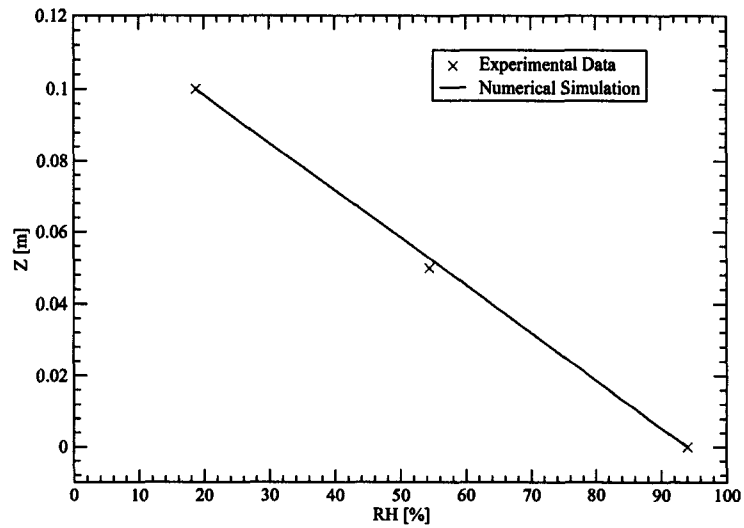


Figure 5.30: Relative humidity profile along a vertical line at the centre of the foam.

senting the foam was used to simulate the transient mass transport across the foam layers. Figure 5.31 illustrates the mesh used for this simulation, where no mesh controls were implemented in the mesh generation, but a constant element mesh size was used.

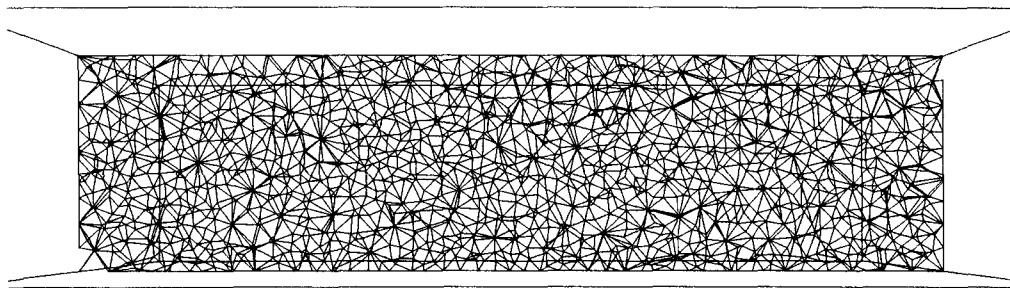


Figure 5.31: Unstructured mixed element mesh used for the discretization of the mini tank at mid plane.

The numerical simulation was carried out under isothermal conditions, in contrast with the experimental data. This assumption is based on experimental results ob-

tained for steady state, where small variations of temperature did not affect the water vapour diffusion in a significance way. In addition, zero velocity is also imposed inside the foam. The initial conditions for RH were set up as the room conditions at the time of the experiment (26% RH). The boundary conditions were zero RH flux at the walls, constant humidity at the top of the foam (as previously explained), and a time dependent humidity profile prescribed at the bottom corresponding to experiment 5 (Figure 5.17). A CDS scheme and a global residual tolerance of 10^{-6} were used for the simulation. Figure 5.32 shows the relative humidity obtained numerically compared with the experiment 5 (Section 5.3.2). The continuous lines represent the values calculated with CFX, while the dotted line represents the experimental data.

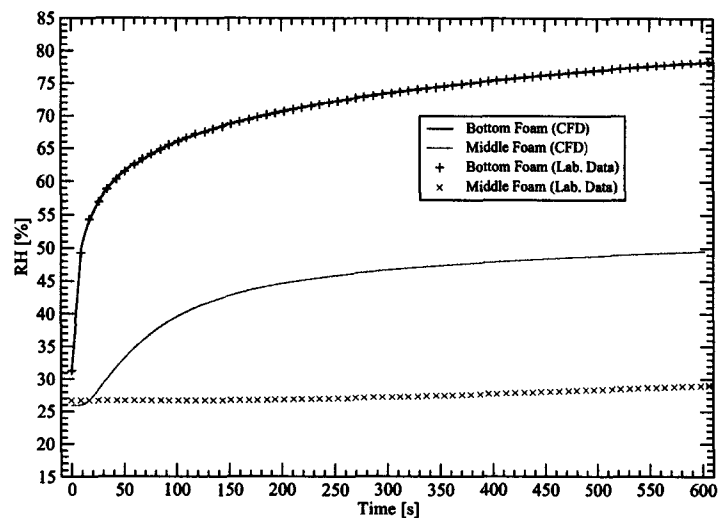


Figure 5.32: A comparison of transient analysis for relative humidity profiles between numerical simulation and experimental data at two different foam locations (bottom and middle position).

The bottom foam humidity values are shown to verify that the boundary conditions are correctly implemented. The difference between the predicted model values and the experiment is quite obvious at the middle foam level, for instance, the predicted amount is 72% larger at the end of the calculations. These results suggest that the theoretical model not only overestimates water vapour transport during this initial

transient, but it also reaches quasi-steady state conditions at 600 s, when the water vapour experiment middle foam sensor starts to respond to the increase of humidity at the bottom of the foam. The explanation for this behaviour comes from the fact that the model does not take into account the adsorption process that occurs in the experiment, as it was explained before. This water accumulation mechanism results in a delay in the mass diffusion through the foam. Therefore, it remains an open question for future research the selection of a suitable porous material that avoids this particular property, adsorption, or to determine through experiments the proper adsorption coefficient that needs to be included into the conservation of species equation.

5.4.3 Convective Flux

In Section 5.3, a relatively constant humidity level was observed at the top of the foam for both test table and mini tank experiments, no matter the amount of water vapour transferred through the foam. Table 5.7 demonstrates that a small continuous flow of fresh air enters the laboratory room (Figure 4.1), which is believed to be responsible for keeping the water vapour concentration constant at the surface of the foam as well as the rest of the laboratory. The following numerical simulation was conducted to approximate this flow as a horizontal flow traveling from one end to the other end of the domain, and to determine the possible velocity magnitude of this approximated flow.

The domain used for this simulation corresponds to the laboratory dimensions and it was described in Figure 4.13, where H , L , W are 1, 4, and 3 m respectively. The steady state analysis was set up with an unstructured mixed element as in previous simulations, where the boundary conditions were as follows:

- Room walls, top room at $RH = 18.79\%$.
- Walls of the porous region (foam) with zero RH flux.

- Water source (bottom of foam), $RH=94.12\%$.
- Left end of the domain was set up to a relative pressure of 0 Pa. (Outlet condition, $\frac{\partial p}{\partial n} = 0$).
- Right end of the domain was set up with normal velocities of 0, 0.01, and 0.5 m/s (Inlet condition at $RH = 18.79\%$).

The process was also defined as isothermal, for the reasons previously described. Two different types of binary diffusion coefficients were used, one for the room (the free space diffusion coefficient), and the effective diffusion coefficient for the foam (calculated in Section 5.3.1). The numerical advection schemes used were CDS, for the 0 m/s case (residual 10^{-6}), and High resolution for 0.01 (residual 10^{-5}) and 0.5 m/s cases (residual 10^{-4}). The initial condition was defined at $RH = 18.79\%$. Figures 5.33, 5.34, 5.35 illustrate the humidity profiles of the room under 0, 0.01 and 0.5 m/s, respectively.

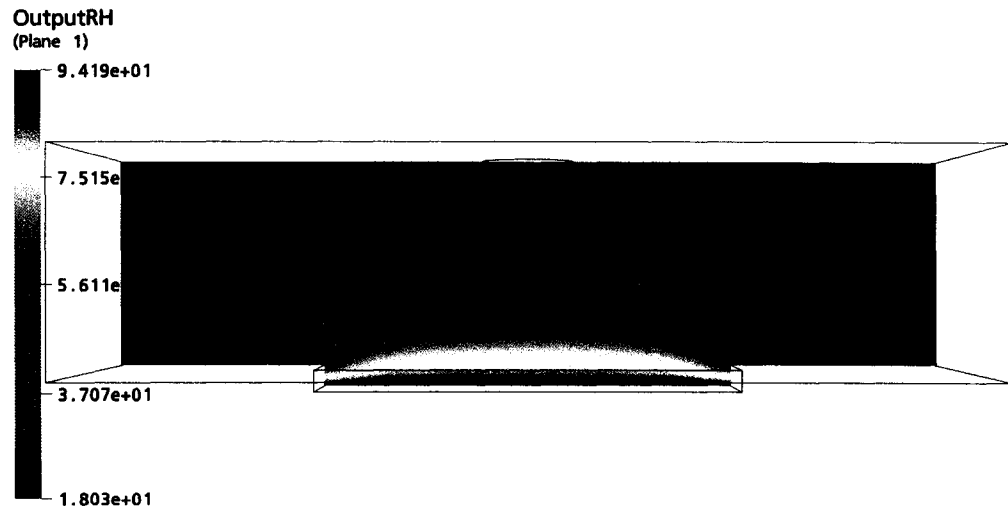


Figure 5.33: Relative humidity profile with no velocity.

Based on Figure 5.33, it can be observed that without any air displacement in the

room the water source under the porous medium humidifies a large part of the region. This differs from the experimental observation. This suggests once again the presence of a convective flow across the room.

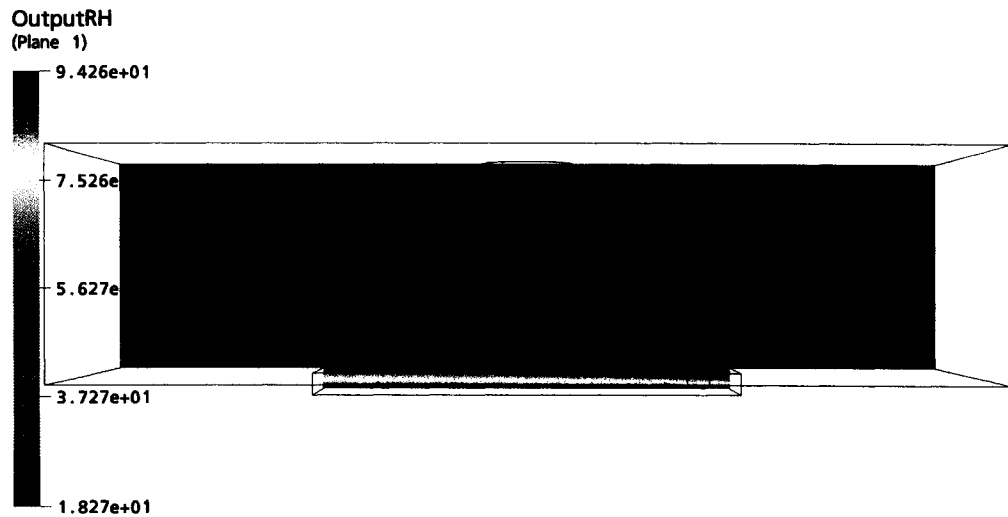


Figure 5.34: Relative humidity profile with a horizontal velocity of 0.01 m/s across the domain.

Figure 5.34 illustrates the significant impact that even small velocities, 0.01 m/s, have on the diffusion process. The highly dominant effect of convection over the molecular diffusion process is obvious.

Finally, Figure 5.35 suggests that in order to maintain a relatively constant humidity on top of the foam surface at 54% *RH*, as it was found in the experimental data, an approximate air flow of 0.5 m/s should be affecting the diffusion process.

Figure 5.36 represents the different *RH* profiles along a vertical line at the centre of the room. The humidity “penetration” into the room is significantly reduced as the transversal velocity across the room increases. Another interesting feature of the simulation is that the linearity of Fick’s law only applies inside the porous medium,



Figure 5.35: Relative humidity profile with a horizontal velocity of 0.5 m/s across the domain.

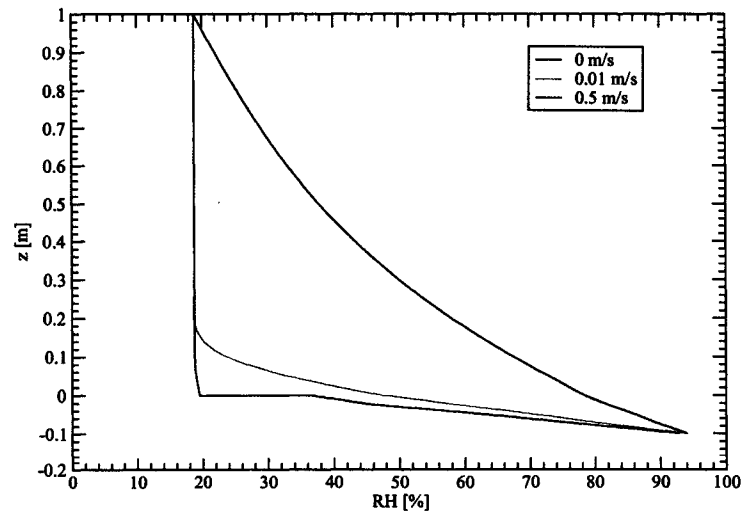


Figure 5.36: Relative humidity profile at mid line for different room air velocities. Zero height corresponds to the surface of the foam.

where the cross sectional area of mass transfer remains constant. In comparison the profile of pure diffusion (black line) within the room becomes nonlinear, due to a continuous increase in the transversal area of diffusion. Finally, the humidity profile at 0.5 m/s (blue line) remains similar to the room conditions just above the foam, as observed in the experimental data. The water vapour flux per unit area calculated in the foam under this condition was, $\dot{m}_A = 2.05 \cdot 10^{-6} \text{ kg/m}^2\text{s}$, which agrees quite well with the experiment 1.

5.4.4 Ward's Model of Laboratory Vortex

The Ward's model used in the following simulation is based on the work of Church and Snow [1993] and Lund and Snow [1993], since detailed experimental data can be used to validate the feasibility of CFX to simulate vortex flows. In addition, this comparison provided an excellent method to evaluate the appropriate turbulence model to be used to simulate tornado-like vortices, and to define the criteria that represent these phenomena geometrically.

The boundary conditions are almost the same as described in Rottuno [1984]. However, a few exceptions were taken into consideration for this study. Since no fan was introduced in the simulation, a larger convection region was placed instead of the original model length. The reason for this approach was to make sure that no disturbing effect was introduced in the vortex flow from downstream. Secondly, no internal cylinder was attached inside the generator. Instead, a control mesh was introduced, which will be described later in this section. Tables 5.8 and 5.9 present a summary of the parameters (Figure 4.11) and boundary conditions used for the Ward's model simulation:

Here c_v and c_r stand for convergence region and convection region respectively.

Table 5.8: Ward’s model geometric parameters (adapted from Church and Snow [1993] and Lund and Snow [1993]).

Parameter	Value	Parameter	Value
h	0.304 m	r_0	0.204 m
r_s	0.5 m	l	5 m
r_c	1.42 m		

Table 5.9: Ward’s model boundary conditions (adapted from Church and Snow [1993] and Lund and Snow [1993]).

BC	Type	Location	Value
Wall	Non-slip	Bottom (cv)	-
Inlet	U_r	Outer edge (cv)	-0.75 m/s
Inlet	U_θ	Outer edge (cv)	0.49 m/s
Outlet	ΔP	Top (cr)	0 Pa
Wall	Non-slip	Outer edge (cr)	-
Temperature	Isothermal	Domain	292.25 k

Simplified numerical setup used to provide initial conditions to the proper Wards model simulations is described below:

- The initial velocity field inside the domain was set to zero.
- The numerical scheme used was UDS.
- The turbulence model used was the $k - \varepsilon$ model, due to its robustness.
- A coarse mesh was used for faster calculations.
- The global residual was set to 10^{-4} .

Once were the initial conditions obtained, a finer unstructured mesh was implemented in the region were the maximum velocities were expected, in the updraft hole region that replaced the inner cylinder in Rottuno [1984]. In addition, the numerical scheme

was changed to “High Resolution” to overcome the high artificial diffusivity introduced by the UDS method. Figure 5.37 illustrates the mesh used for both $k - \varepsilon$ and RSM models.

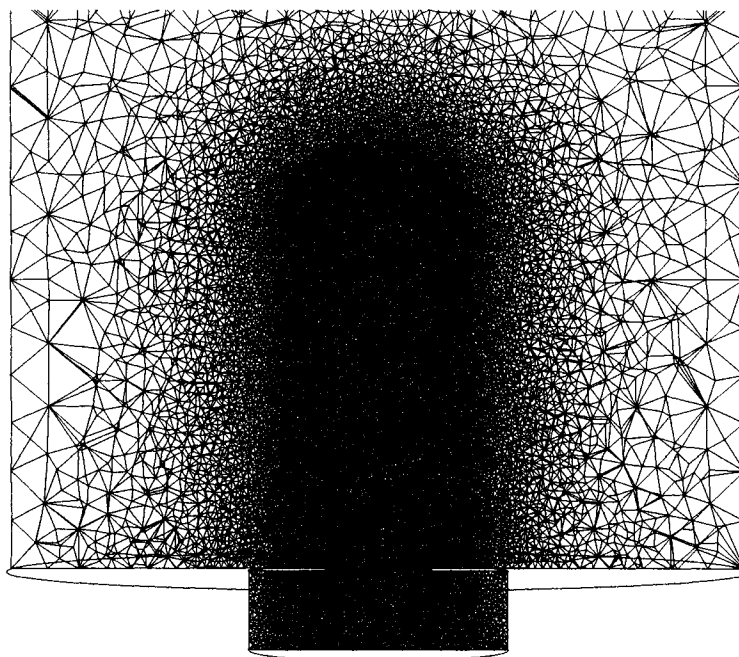


Figure 5.37: Unstructured mixed element mesh used for the discretization of the Ward's model showing the updraft hole region close up.

Versteeg and Malalasekera [1995] explain that strong streamline curvatures in developing vortices lead to a reduction in the production of turbulent kinetic energy that helps the vortex to become three dimensional. They also mention that one of the drawbacks of the $k - \varepsilon$ turbulence model is the malfunction of the model in case of flows influenced by effects of streamline curvature. In contrast, the RSM is known to perform well in anisotropic turbulence, typical of flows with streamline curvature.

A comparison between the $k - \varepsilon$ model and the RSM with in High Resolution scheme was conducted. Figure 5.38 shows the turbulent kinetic energy in the predicted flow at mid plane around the updraft hole region for the RSM (left) and the $k - \varepsilon$ models

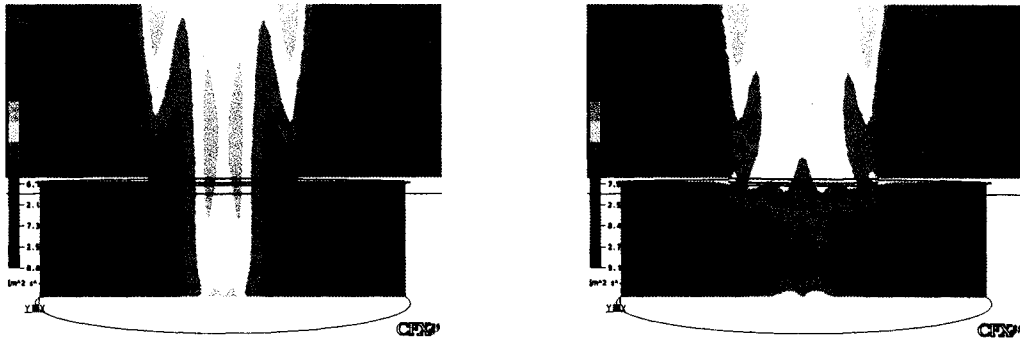


Figure 5.38: Contours of the predicted turbulent kinetic energy of the Ward's model, using RSM model (left) and $k - \varepsilon$ model (left).

(right). The $k - \varepsilon$ model leads to a high production of turbulent kinetic energy at the edges of the updraft hole. The same area presents a relative low turbulence production in the RSM model. This comparison shows the diffusive effect of the $k - \varepsilon$ model by its overpredicted turbulence kinetic energy production. As a consequence, a weaker velocity field is obtained inside the vortex region.

Figure 5.39 presents the numerical results of the tangential velocity profiles for the Ward's model, compared with the experimental data of Lund and Snow [1993]. Comparison shows that the present results obtained using RSM are in reasonable agreement with the experimental data and are better than the results from $k - \varepsilon$ model.

Based on the comparison between the $k - \varepsilon$ and RSM models, a quantitative analysis was conducted by examining flow features of the Ward model that correspond to the geometric parameters r_0 and h of a vortex. Figure 5.40 and 5.41 present a simple criteria to define r_0 and h . For instance, the radial location where the radial velocity has its maximum absolute value corresponds to r_0 , and the axial location height of the maximum value of the axial velocity at r_0 corresponds to h . At these locations, the estimated values of r_0 and h agree quite well with the real dimensions of r_0 and h of the Ward's model geometry used for these simulations.

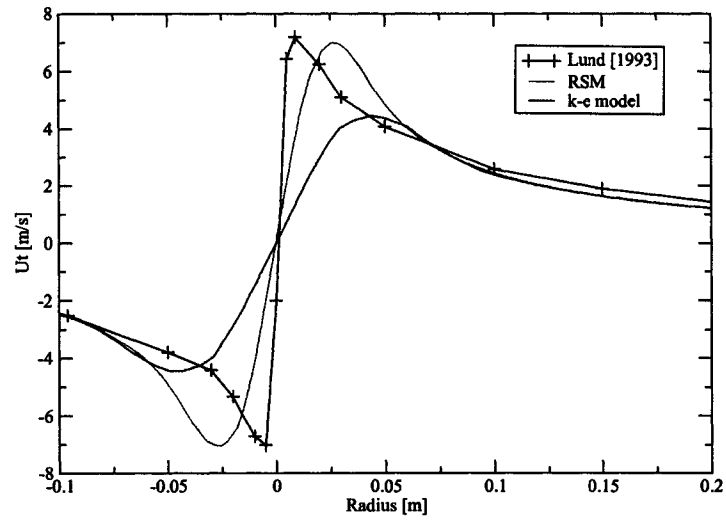


Figure 5.39: Radial profile at 0.15 m elevation of the tangential velocity component.

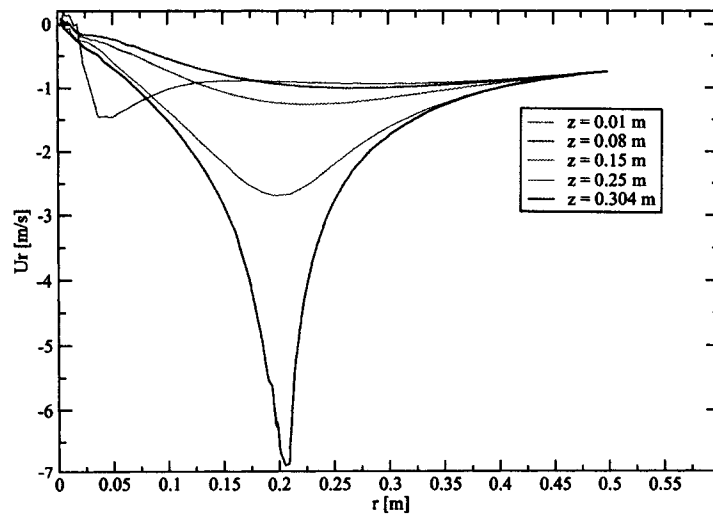


Figure 5.40: Ward's model radial profiles of radial velocity component at different elevations.

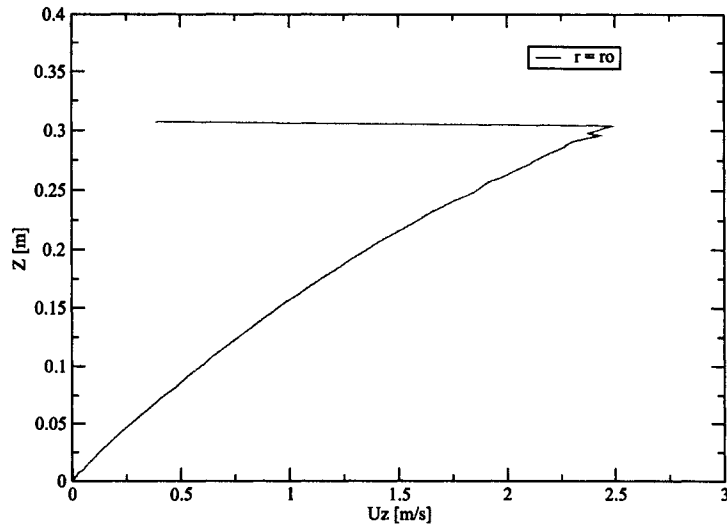


Figure 5.41: Ward's model profile of the axial vertical velocity component at $r = r_0$.

Finally, Figure 5.42 illustrates an isosurface of vorticity in the z direction equal to 4 s^{-1} in the Ward's model showing the vortex structure in 3D.

5.4.5 Open Model of Laboratory Vortex

Using the flow-based criteria developed in the previous section, we can attempt to estimate the parameters r_0 and h for the open vortex model case. This section examines the feasibility of a disc-rotating wall as the element of vortex generation, and the applicability of the characterization criteria described above to be used as a scaling method for dust devils in different domain sizes or environments, such as Earth or Mars conditions.

Two domains were used in this study: a rectangular and cylindrical domain. The rectangular has 6 m x 6 m by 1 m height, while the cylindrical consists of 6 m by 1 m height. The boundary conditions for the model case were all set as walls with non-slip condition. In other words, the numerical domain is completely closed. However, a disc shaped region in the centre of the top wall is set as a rotating wall with

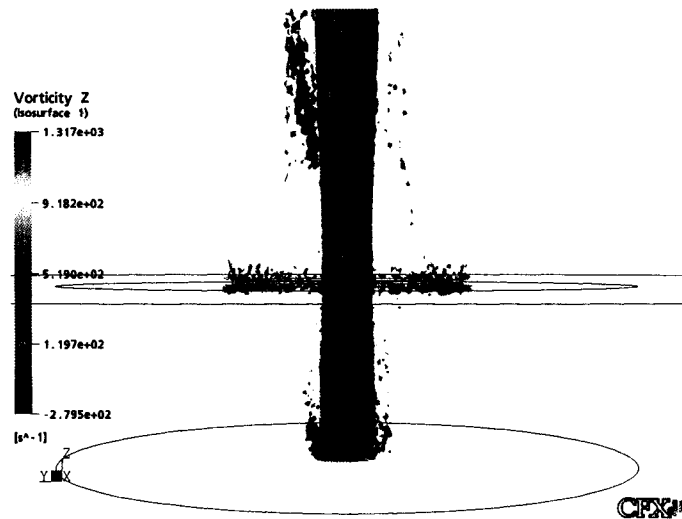


Figure 5.42: Vorticity isosurface in Ward's model.

a specified angular velocity, where the axis of rotation is the centre of the disk (see Figures 4.12a and 4.12b). The model, as in the Ward's model case, was isothermal with a temperature of 292.25 K.

The initial conditions for both rectangular and cylindrical domains were identical. The following procedure describes the method used to create the vortex from zero initial velocity to its final stage. For the initial solution all the simulations were carried out with UDS advection scheme, a global residual of 10^{-4} , and the $k - \epsilon$ turbulence model. A coarse unstructured mesh with no mesh control of any sort was used, as shown in Figures 5.28 and 5.31. Several runs were used to reach the final stage of the vortex. Incrementing the angular velocity of the rotating disk to 1, 100, 1000 RPM, and for each time using the previous RPM simulation results, we were able to obtain a final simulation with the disc rotating at 1750 RPM, the same speed as the experimental vortex generator (see Section 5.3.4). At this point, the simulation was switched to the RSM model, High Resolution advection scheme, and to transient mode. For robustness and accuracy the mesh was refined at the center of the domain, as was also the case in the Ward's model simulation (see Figure 5.37).

The first step in the open model analysis was the use of the rectangular domain, since its rectangular shape was more appropriate to represent similar characteristics in the laboratory room. However, as it can be observed in Figure 5.43, this model is not the most suitable for an axisymmetric flow analysis, due to the nonsymmetrical characteristics of the domain. Not all the flow travels towards the center of the vortex (green area), but some of it goes in the opposite direction (yellow regions). For this reason, the cylindrical domain was used instead of the rectangular domain.



Figure 5.43: Vorticity isosurface in the Open model showing the velocity field at a cross-sectional plane.

In contrast, Figure 5.44 does have a fully axisymmetric profile that is needed to evaluate the geometric dimension parameters required to characterize dust devils. Figure 5.44 also shows a vorticity isosurface at 3 s^{-1} , providing a 3D representation of the vortex.

Figures 5.45 and 5.46 represent the radial profiles of the radial velocity component at different elevations, and the vertical profile of the axial vertical velocity component at $r = r_0$, respectively, for the cylindrical domain case.

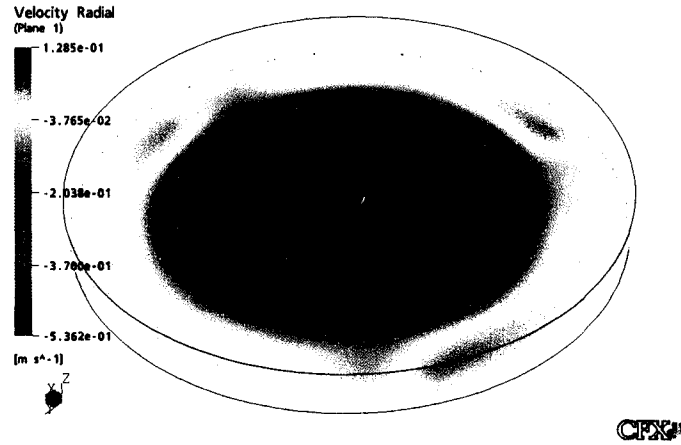


Figure 5.44: Vorticity isosurface in the Open model showing the velocity field at a cross-sectional plane.

Based on these results, we can determine the dimensions of r_0 and h based on the definitions proposed in the previous section, which for our case are 3.07 m and 0.55 m, respectively. Using equations 3.38 and 3.37, we can now calculate the values of U_r and U_θ . We obtained:

$$U_r = 0.33\text{m/s} \quad ; \quad U_\theta = 0.21\text{m/s}$$

Therefore, the values of the swirl ratio, aspect ratio, and radial Reynolds number are (see Chapter 3):

$$S = \frac{3.07 \cdot 0.21}{2 \cdot 0.55 \cdot 0.33} = 1.78$$

$$a = \frac{0.55}{3.07} = 0.18$$

$$Re_r = \frac{3.07 \cdot 0.33}{1.54 \cdot 10^{-5} \cdot 0.55} \approx 119780$$

To examine the validity of the scaling parameters we set up a new Ward's model simulation using the values of S and a calculated above, based on kinematic similarities. In other words, a new Ward's model case was calculated defining r_o , h , u_r , and

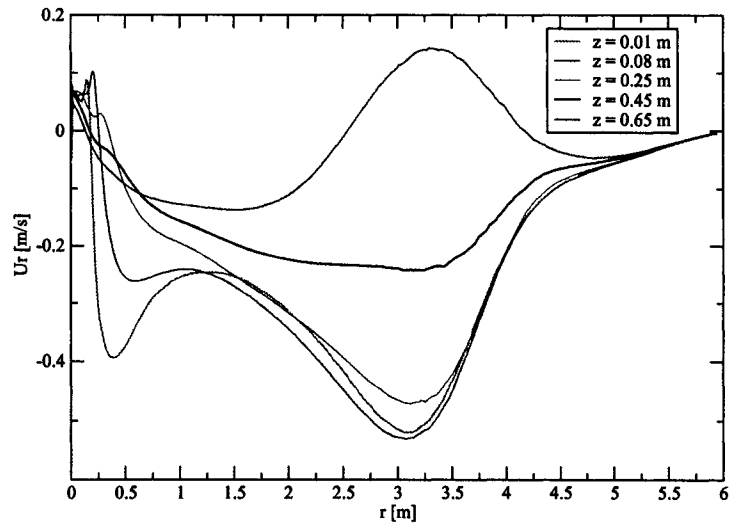


Figure 5.45: Open model radial profiles of radial velocity component at different elevations.

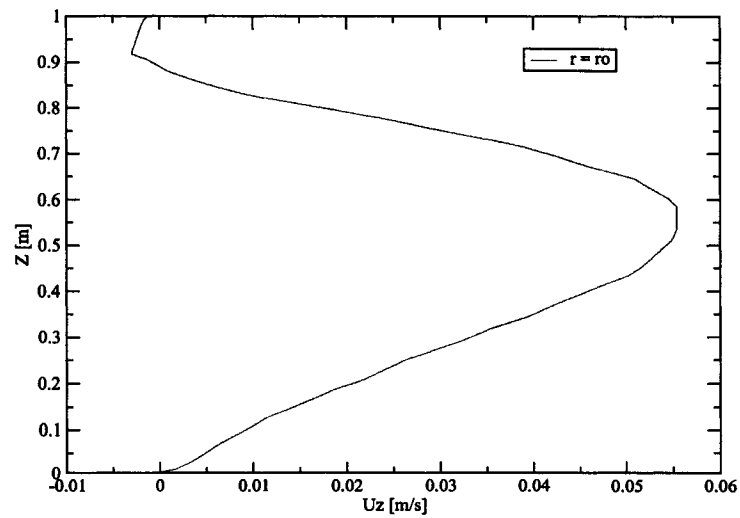


Figure 5.46: Open model axial profile of the axial vertical velocity component at $r = r_0$.

U_θ with the open model values of 3.07 m, 0.55 m, 0.33 m/s, and 0.21 m/s respectively. The rest of the set up was identical to the Ward's model in the previous section.

However, the results obtained were not as expected. In fact, the simulation reproduced a vortex structure two orders of magnitude smaller than the Open model (Figure 5.47). Another interesting difference between both models is in the core radius, which is located at the maximum tangential velocity (Chapter 2). For the open model case was 0.3 m, whereas for the Ward's model case it was 2 m. The reason for this failure of the kinematic similarities is believed to be in the numerical design of the open model vortex generator. In real tornado-like vortices the axial momentum in the core flow region is responsible for the stability of the vortex structure. However, in the current open model, the rotating wall has a suppressing action in this mechanism. This leads to a low axial momentum, and, as a consequence, a weaker vortex is produced. Even though the comparison between both Ward model and open model could not be established, it is believed that the present study presents a reasonably simple criteria to determine the geometric parameters needed to the proper characterization and scaling of dust devils.

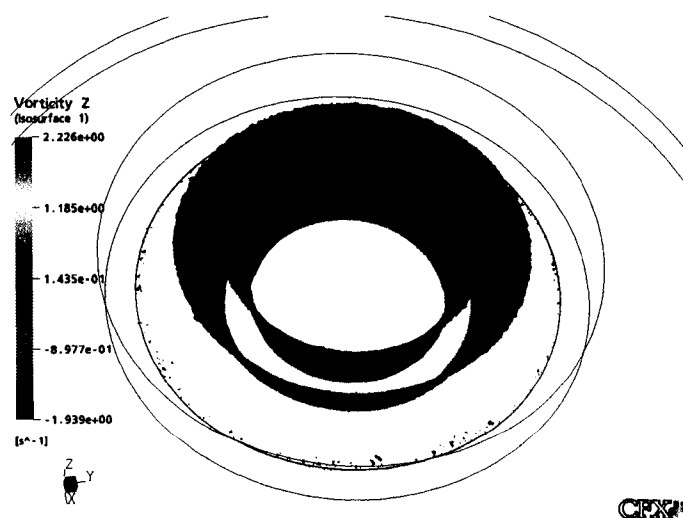


Figure 5.47: Vorticity isosurface in the new Ward's model showing a vorticity of 0.2 s^{-1} .

5.4.6 Water vapour and dust devils

This section describes a simulation that was conducted to perform a qualitative analysis of the influence of dust devils on the water vapour transport. The numerical domain is described in Section 4.2.2, Figure 4.13. The top part represents the laboratory room, and the lower part represents the test table. The boundary conditions were as follows:

- Zero RH flux at the walls of the test table.
- Bottom foam surface (experiment 1, Section 5.3.1) with a prescribed RH of 94.12%.
- Room wall (experiment 1, Section 5.3.1) with a prescribed RH of 18.79%.
- Rotating disc wall at 1750 RPM (Section 5.3.4).

The mesh was a combination of the model convective flux (Section 5.4.3) and the test table model (Section 5.4.1). The initial conditions implemented the same procedure as the method described in Section 5.4.5. However, the use of the RSM model to calculate the final stage of the numerical simulation was not possible, due to some error presented in the numerical solver code. It is believed that a numerical device used to connect both room and test table, called domain interface, was related to the error. The use of this domain interface was obligatory in order to connect the two physical domains (i.e. the room and the porous region) and no other option was available in CFX to perform this connection. Repeated attempts to overcome this issue remained unsuccessful. Nevertheless, the simulation using the $k - \varepsilon$ model indicates important aspects of the present study. A tornadolike vortex does affect locally the water vapour flux, as it was experimental data. Figure 5.48 shows a significant increase in water vapour concentration at the core of the vortex driven by the velocity gradient in comparison with Figure 5.35.

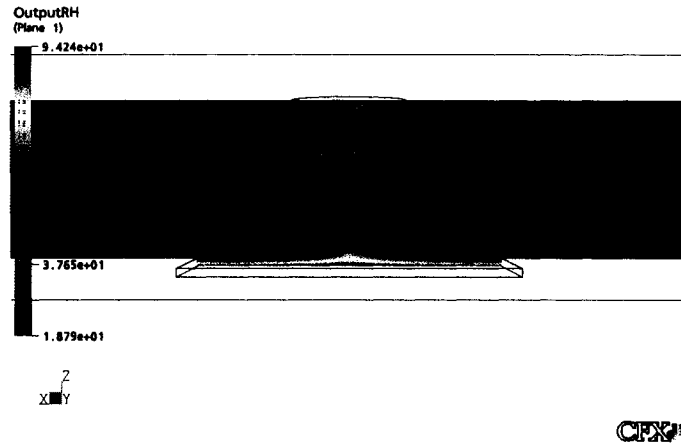


Figure 5.48: Water vapour profiles under the influence of a dust devil.

The total water vapour flux estimated in this case is $\dot{m} = 5.77 \cdot 10^{-6}$ kg/s, which represents an increase of 1.4 times over the “still air” case calculated small convection (Section 5.4.3) of $\dot{m} = 4.1 \cdot 10^{-6}$ kg/s. These final results show an increase in the water vapour loss as was demonstrated in the experimental data. However, the increase in the water vapour mass flux for the numerical simulation is much smaller than that in the experimental data. There is a difference in increase because it is believed that the lack of an axial momentum to narrow down the vortex core failed to produce a stronger convective term that would have otherwise increased the water vapour flux rate at the vortex core.

Chapter 6

Conclusions

A study was conducted to define a numerical model that predicts local water vapour transport rates under the influence of dust devils. The purpose of this work was to determine the numerical methodology and experimental devices needed to reach the final goal of a complete model able to predict spatial water vapour concentration near surface from the Phoenix Lander data field in 2008, the results of which will help us understand the cycle of water on Mars.

Experiments were performed to determine the macro-physical properties of the porous material, which in this case was a polyurethane foam representing the regolith. Porosity, φ , was determined by using a multipycnometer. The intrinsic permeability, K , was determined by a simple airflow test. Tortuosity, τ , was obtained from indirect calculations based on the experimental data and assuming Fick's law modified for porous media. The property values obtained were all in good agreement with the values from manufacturer and from literature. The aforementioned properties were required for the theoretical model.

The need for directly measuring temperature and relative humidity distributions required the development of a proper data acquisition system to store the data from the dual RH/T sensors. Calibration and reliability of the temperature and humid-

ity sensors and average absolute errors were found for each relative humidity (RH), temperature (T), and time response. Values were fully consistent with the accuracy specifications of the manufacturer.

Experiments conducted in still air conditions served not only to help characterize the foam, but also to confirm a few more points. The results show, for example, that steady state conditions were obtained after 16 hours and it could be maintained stable as long as a water source was present. An interesting feature was that small variations in temperature and small temperature gradients do not significantly affect the molecular diffusion described by Fick's Law. Numerical simulations of the foam region only matched the experimental results well.

Additional experiments were conducted to analyze the applicability of Fick's Law to predict time dependency of the water vapour transport. However, the results showed that Fick's Law alone cannot describe the process. A comparison of the numerical simulation with experimental data showed that the theoretical model significantly overestimated the mass transport in the initial stages. It was shown that the cause for this behaviour is the need for an extra source term that represents the accumulation of water inside in the porous material by adsorption.

A series of experimental and numerical simulations was conducted to analyze the degree of dominance of the convective flux over molecular diffusion. Both experiments and simulations suggest a significant influence of airflow over molecular diffusion. In fact, a relatively small air velocity, such as 0.01 m/sec in the laboratory room has a very large impact on the humidifying effect. This effect explains how a small amount of fresh air in the laboratory kept the water vapour concentration at the surface of the foam as well as the room walls stays constant regardless of the amount of water vapour provided by the water source. Finally, an additional numerical simulation was carried out to approximate the velocity of the airflow obtained in the experiments data into the numerical models. The result found that a horizontal velocity of 0.5

m/s made the data agree quite well with the experiments.

In order to validate the vortex that might influence the water vapour mass flux, Ward's Model was used to verify the feasibility of the turbulence models, such as $k - \varepsilon$ model and RSM model, built in the CFX. First of all, the numerical results in comparison with experimental data suggest that the RSM model produces more accurate results than the $k - \varepsilon$ model to reproduce a laboratory vortex, as expected. Secondly, an additional advantage of Ward's Model was to define a proper criterion to geometrically estimate the parameters of the updraft radius, r_0 , and the inflow depth layer, h , by quantitative analysis. The results suggest that r_0 is to be found at the maximum absolute radial velocity component, and h at the maximum axial vertical component at $r = r_0$.

Using the same flow-based criterion as Ward's Model, an attempt to define r_0 and h was conducted for the open case model. The findings obtained for this open case were not satisfactory. A second attempt to redefine Ward's Model based on the values obtained for the open case, that is r_0 and h , did not reproduce a similar velocity field profile, as was present in the open case. In fact, the redefine Ward's Model shows a vorticity structure two orders of magnitude smaller than that of the open case. In addition, a core radius of 0.3 m was found for the open case whereas a radius of 2 m was found for Ward's Model. It is believed that the failure in the comparison of both models do not correspond to the kinematic similarities, but in the design of the open case. This failure can be on account of the inability of the open case to recreate the axial momentum. This source of momentum helps to increase updraft flow, which is present in tornado-like vortices, in a narrow region.

However, an important feature that can be extracted from this numerical simulation is that dust devils actually do affect the local water vapour mass flux rate over porous regions. The experimental and numerical results showed an increase of five to seven times in the mass flux rate over the still air case.

In light of the findings during this study, future research could include Knudsen diffusion, thermal diffusion into the theoretical modelling since these mechanisms are believed to be an important water vapour mass transport factor in Martian conditions. Additionally, an open question for the selection of the porous material could be the implementation of the adsorption coefficient as an extra source into the governing equation, or the use a porous medium without this particular water adsorption property since numerical simulation and experimental data show that adsorption mechanisms could significantly affect the transient mass transport time response phenomenon. Moreover, the development of an open model that can reproduce tornado-like vortices, with the axial momentum included, can be a second important target for further investigation due to the need to validate the theory that supports kinematic similarities between different vortex models. Finally, because RSM Models are known to perform better than $k - \varepsilon$ model to reproduce vortex flows, another possible study is the use of the new version of CFX10.0 to assess the compatibility of the RSM model with domain interface configurations.

Bibliography

- W. Y. Abu-EL-Sha'r. *Experimental Assessment of Multicomponent Gas Transport Mechanisms in Sub-surface Systems*. Ph. D. dissertation, Univ. of Mich, 1993.
- C. R. Alexander and J. Wurman. The 30 May 1998 Spencer, South Dakota, storm. Part I: The structural evolution and environment of the tornadoes. *Mon. Wea. Rev.*, 133:72 – 96, 2005.
- A. A. Alzaydi. *Flow of Gases Through Porous Media*. Ohio State University, Columbus, 1975.
- A. A. Alzaydi and C. A. Moore. Combined pressure and diffusional transition region flow of gases in porous media. *AICHE J.*, 24(1):35–43, 1978.
- ANSYS. *ANSYS/CFX5.7 Manual*. Ansys Inc., Waterloo, Ontario, Canada, 2005.
- B. V. Antohe and J. L. Lage. A general two-equation macroscopic turbulence model for incompressible flow in porous media. *Int. J. Heat Mass Transfer*, 40(1):3013 – 3024, 1997.
- ASTM. *ASTM D 3574, Standart Test Methods for Flexible Cellular Materials - Slab, Bonded, and Molded Urethane Foams*. ASTM International, 100 Barr Harbor Drive, West Conshohocken, PA, USA, 2003.
- M. R. Balme, P. L. Whelley, and R. Greeley. Mars: Dust devil track survey in Argyre Planitia and Hellas Basin. *J. Geophys. Res.*, 108(E8), 2003.
- R. W. Barber and D. R. Emerson. *Advances in Fluid Mechanics IV*, chapter The Influence of Knudsen Number on the Hydrodynamic Development Length within Parallel Plate Micro-channels, pages 207 – 216. WIT Press, Southampton, UK, 2002.

- T. J. Barth and D. C. Jespersen. The design and application of upwind schemes on unstructured meshes. *AIAA*, (89), 1989.
- J. Bear. *Dynamics of Fluids in Porous Media*. Dover Publications, 1988.
- R. B. Bird, W. E. Stewart, and E. N. Lightfoot. *Transport Phenomena*. John Wiley and Sons, Inc., 2 edition, 2001.
- H. B. Bluestien, C. C. Weiss, and A. L. Pazmany. Doppler radar observations of dust devils in texas. *Mon. Wea. Rev.*, 132(1):209 – 224, 2003.
- D. D. Bosch and A. Shirmohammadi. *Encyclopedia of Water Science*, chapter Soils, Hydraulic Conductivity Rates in, pages 919–921. Marcel Dekker, Inc., 2003.
- Bouzidi. *The Acoustic Reflectivity and Transmissivity of Liquid Saturated Porous Media Experimental Tests of Theoretical Concepts*. University of Alberta, Edmonton, Alberta, Canada, 2003. Ph.D dissertation.
- E. Buckingham. Studies on the movement of soil moisture. *USDA Bur. Soils Bull.*, (38), 1907.
- J. M. Burgers. A mathematical model illustrating the theory of turbulence. *Adv. Appl. Mech.*, 1:171 – 199, 1948.
- Y. A. Çengel. *Heat and Mass Transfer*. McGraw-Hill, 3 edition, 2007.
- C. R. Church and J. T. Snow. *The Tornado: Its Structure, Dynamics, Prediction, and Hazards*, chapter Laboratory Models of Tornadoes, pages 277 – 295. American Geophysical Union, Washington, D. C., USA, 1993.
- S. M. Clifford and D. Hillel. Knudsen diffusion: The effect of small pore size and low gas pressure on gaseous transport in soil. *Soil Science*, 141(4):289–297, 1986.
- R. E. Cunningham and R. J. J. Williams. *Diffusion in Gases and Porous Media*. Plenum Press, 1980.
- H. Darcy. *Les Fontaines Publique de la Ville de Dijon*. Dalmaton, 1856.
- R. P. Davies-Jones. The dependence of core radius on swirl ratio in a tornado simulator. *J. Atmos. Sci.*, 30:1427 – 1430, 1973.

- R. P. Davies-Jones. Laboratory simulations of tornadoes. *Preprints Symposium on Tornadoes*, pages 151 – 174, 1976.
- R. P. Davies-Jones. *Thunderstorms: A Social, Scientific and Technological Documentary*, volume 2, chapter Tornadoes Dynamics. U.S. Department of Commerce, Washington, D. C., USA, 1982.
- R. P. Davies-Jones and E. Kessler. *Weather and Climate Modification*, chapter Tornadoes, pages 552–595. John Wiley, New York, USA, 1974.
- S. R. de Groot and P. Mazur. *Non-Equilibrium Thermodynamics*. Dover Publications, Inc, 1984.
- T. E. Detty. *Determination of Air and Water Relative Permeability Relationships for Selected Unconsolidated Porous Materials*. Ph. D. dissertation, Univ. Ariz., Tucson, 1992.
- D. D. Do. *Adsorption Analysis: Equilibria and Kinetics*, volume 2. Imperial College Press, 1998.
- J. Dupuit. *Etudes Theoriques et Pratiques sur le Mouvement des Eaux*. Dunod, 1863.
- K. S. Edgett and M. C. Malin. Martian dust raising and surface albedo controls: Thin, dark (and sometimes bright) streaks and dust devils in mgs high-resolution images. In *XXXI Lunar and Planetary Science*, 2000.
- A. Fick. Über diffusion. *Annalen der Physik und Chemie*, 94:59–86, 1855.
- Foamex. Permanently compressed reticulated foam polyester or polyether urethane. Report TS-696-FLT-5M, Foamex, 1500 East Second Street, Eddystone, Pa, 19022, 1999.
- P. Forchheimer. Wasserbewegung durch Boden. *Z. Ver. Deutsch. Ing.*, 45:1781–1788, 1901.
- W. A. Gallus, F. L. Haan, P. P. Sarkar, K. Le, and J. Wurman. Comparison of numerical model and laboratory simulator tornado wind fields with radar observations of the Spencer, South Dakota tornado. In *Symposium on the Challenges of Severe Convective Storms*, Atlanta, GA, USA, 2006. Amer. Meteor. Soc.

- E. R. Gilliland, R. Baddour, G. P. Perkinson, and K. Sladek. Diffusion on surfaces. *Ind. Eng. Chem. Fund.*, 13(3):95 – 99, 1974.
- A. Grant. Dust devils in the sub-artic. *Weather*, 4:402 – 403, 1949.
- R. Greeley, J. Iversen, G. Beardmore, B. Mickelson, and S. Metzger. Martian dust devils: Laboratory simulations. In *XXXII Lunar and Planetary Science*, 2001.
- R. Greeley, M. R. Balme, J. D. Iversen, S. Metzger, R. Mickelson, J. Phoreman, and B. White. Martian dust devils: Laboratory simulations of particle threshold. *J. Geophys. Res.*, 108(E5), 2003.
- L. Gu, C. K. Ho, O. Plumb, and S. W. Webb. Diffusion with condensation and evaporation in porous media. In *AIAA/ASME Joint Thermophysics and Heat Transfer Conference*, volume 2, pages 213 – 220. ASME, 1998.
- O. Gülseren, T. Yildirim, and S. Ciraci. Tunable adsorption on carbon nanotubes. *Phys. Rev. Lett*, 87(11), 2001.
- R. V. Gummaraju, R. F. Pask, H. J. Koller, S. E. Wujcik, and K. A. Reimann. Evaluation, modification, adaptation of an airflow test method for polyurethane foams. *J. Cell. Plast.*, 37:193 – 206, 2001.
- M. G. Hall. The structure of concentrated vortex cores. *Prog. Aeronaut. Sci.*, 7:53 – 110, 1966.
- R. Hannesen, N. Dotzek, and J. Handwerker. Radar analysis of a tornado over hilly terrain on 23 July 1996. *Phys. Chem. of the Earth*, pages 1079 – 1084, 2000.
- P. W. Hebner. Polyurethane foam: Polymers’s cinderella product. In *Insight 95 International Conference*, USA, 1995. Foamex International.
- G. D. Hess and K. T. Spillane. Characteristics of dust devils in Australia. *J. Appl. Met.*, 29:498 – 507, 1990.
- C. K. Ho and S. W. Webb. A review of porous media enhanced vapor-phase diffusion mechanisms, models, and data - does enhanced vapor-phase diffusion exist? Report 1198, Sandia National Laboratories, Albuquerque, New Mexico 87185 and Livermore, California 94550, 1996.

- C. Hsu. Laboratory modeling of the tornado suction mechanism. In *8th Conference on Severe Local Storms*, pages 199 –202. AMS, 1973.
- M. K. Hubbert. Darcy law and the field equations of the flow of underground fluids. *Trans. Amer. Inst. Min. Mandal. Eng.*, 207:222–239, 1956.
- S. B. Idso. Tornado or dust devil: The enigma of desert whirlwinds. *Amer. Sci.*, 62: 530 – 541, 1974.
- D. B. Jaynes and A. Rogowski. Applicability of fick's law to gas diffusion. *Soil Sci. Soc. Am. J.*, 47:425–430, 1983.
- D. D. Joseph, D. A. Nield, and G. Papanicolaou. Nonlinear equation governing flow in a saturated porous medium. *Water Resour. Res.*, 18(4):1049–1052, 1982.
- J. C. Kaimal and J. A. Businger. Case studies of a convective plume and dust devil. *J. Appl. Met.*, 9:612 – 620, 1970.
- K. M. Kanak. Numerical simulation of dust devil-scale vortices. *Q. J. R. Meteorol. Soc.*, 131:1271 – 1292, 2005.
- L. J. Klinkenberg. *Drilling and Production Practices*, chapter The Permeability of Porous Media to Liquid and Gases, pages 220–213. Am. Pet. Inst., Washington, D.C., USA, 1941.
- M. Knudsen. Die gesetze der molecularströmung und der inner reibungsströmung der gase durch röhren. *Annalen der Physik und Chemie*, 28:75–130, 1909.
- A. Kolmogorov. Dissipation of energy in the locally isotropic turbulence. *Dokl. Akad. Nauk. SSSR*, 30(301), 1941. Reprinted in Proc. R. Soc., London, 1991.
- P. K. Kundu. *Fluid Mechanics*. Academic Press, London, England, 1990.
- B. E. Launder and D. Spalding. The numerical computation of turbulent flows. *Comput. Methods Appl. Mech. Eng.*, 3:269 – 289, 1974.
- D. C. Lewellen and W. S. Lewellen. The influence of local swirl ratio on tornado intensification near the surface. *J. Atmos. Sci.*, 57:527 – 544, 2000.
- W. S. Lewellen. A solution for three-dimensional vortex flows with strong circulation. *J. Fluid. Mech.*, 14:420 – 432, 1962.

- W. S. Lewellen. Theoretical models of the tornado vortex. In R. E. Peterson, editor, *Proceedings of Symposium on Tornadoes*, pages 107 – 143, Lubbock, Texas, USA, 1976. Texas Tech. University.
- W. S. Lewellen. *The Tornado: Its Structure, Dynamics, Prediction, and Hazards*, chapter Tornado Vortex Theory, pages 19–39. American Geophysical Union, Washington, D. C., USA, 1993.
- W. S. Lewellen and D. C. Lewellen. Large-eddy simulation of a tornado’s interaction with the surface. *J. Atmos. Sci.*, 54(5):581 – 605, 1997.
- W. S. Lewellen and Y. P. Sheng. Modeling tornado dynamics. Report 1585, Aeronaut. Res. Assoc. of Princeton Inc., Springfield, Va, USA, 1980.
- C. Ludwig. Diffusion zwischen ungleich erwärmten Orten gleich zusammen-gesetzter Lösungen. *Sitzber. Akad. Wiss.*, 20:539, 1856.
- D. E. Lund and J. T. Snow. *The Tornado: Its Structure, Dynamics, Prediction, and Hazards*, chapter Laser Doppler Velocimeter Measurements in Tornadolike Vortices, pages 297 – 306. American Geophysical Union, Washington, D. C., USA, 1993.
- E. A. Mason, R. J. Munn, and R. J. Smigh. *Advances in Atomic and Molecular Physics*, chapter Thermal Diffusion in Gases, page 33. Academic Press, New York, USA, 1966.
- E. A. Mason, A. P. Malinaukas, and R. B. E. III. Flow and diffusion of gases in porous media. *J. Chem. Phys.*, 46(8):3199–3216, 1967.
- W. J. Massmann. A review of the molecular diffusivities of H₂O, CO₂, CH₄, CO, O₃, SO₂, NH₃, N₂O, NO, and NO₂ in air, O₂ and N₂ near STP. *Atmospheric Environment*, 32(6):1111–1127, 1998.
- W. J. Massmann and D. F. Farrier. Effects of atmospheric pressures on gas transport in the vadose zone. *Water Resour. Res.*, 28:777–791, 1992.
- M. T. Mellon and B. M. Jakosky. Geographic variations in the thermal and diffusive stability of ground ice on Mars. *J. Geophys. Res.*, 98(E2):3345–3364, 1993.
- S. M. Metzger, J. R. Johnson, J. R. Carr, T. J. Parker, and M. T. Lemmon. Dust devils vortices seen by the Mars Pathfinder Camera. *Geophys. Res. Lett.*, 26:2781 – 2784, 1999.

- S. M. Metzger, J. R. Carr, J. R. Johnson, T. J. Parker, and M. T. Lemmon. Techniques for identifying dust devils in Mars Pathfinder Camera. *IEEE Trans. Geosci. Remote Sens.*, 38(2):870 – 876, 2000.
- A. F. Mills. *Mass Transfer*. Prentice Hall, 2001.
- B. R. Morton. The physics of firewhirls. *Fire Res. Abstr. Rev.*, 12:1 –19, 1970.
- B. R. Morton. Vorticity and vortices. In *Proceedings of the Joint IUTAM/IUGG Symposium on Intense Atmospheric Vortices*, 1981.
- D. A. Nield and A. Bejan. *Convection in Porous Media*. Springer, 2 edition, 1999.
- D. S. Nolan and B. F. Farrell. The structure and dynamics of tornado-like vortices. *J. Atmos. Sci.*, 56:2908 – 2936, 1999.
- P. V. Patel and J. B. Butt. Computational simulation of surface diffusion in porous materials. *Chem. Eng. Science*, 27(12):2175–2182, 1972.
- Quantachrome. *Multipycnometer Manual*. Quantachrome Instruments, Boynton Beach, FL, USA, 2003.
- W. J. Rankine. *A Manual of Applied Mechanics*. Charles Griffin and Co., London, England, 1858.
- N. O. Rennó, M. L. Burkett, and M. P. Larkin. A simple thermodynamical theory for dust devils. *J. Atmos. Sci.*, 55:3244 – 3252, 1998.
- N. O. Rennó, A. A. Nash, J. Lunine, and J. Murphy. Martian and terrestrial dust devils: Test of a scaling theory using pathfinder data. *J. Geophys. Res.*, 105(E1): 1859–1865, 2000.
- N. Rott. On the viscous core of a line vortex. *Z. Agnew Math. Mech.*, 9:543 – 553, 1958.
- R. Rottuno. Numerical simulation of a laboratory vortex. *J. Atmos. Sci.*, 34:1942 – 1956, 1977.
- R. Rottuno. Vorticity dynamics of a convective swirling boundary layer. *J. Fluid Mech.*, 97:623 – 640, 1980.

- R. Rottuno. An investigation of a three-dimensional asymmetric vortex. *J. Atmos. Sci.*, 41:283 – 297, 1984.
- H. Savijarvi. Mars boundary layer modeling: Diurnal moisture cycle and soil properties at the Viking lander 1 site. *Icarus*, 117:120–127, 1995.
- B. R. Scanlon, J. P. Nicot, and J. W. Massmann. *Soil Physics Companion*, chapter Soil Gas Movement in Unsaturated Systems, pages 297 – 341. CRC Press, Boca Raton, FL ,USA, 2002.
- P. Schneider and J. M. Smith. Adsorption rate constant from chromatography. *AICHE J.*, 14:762 – 771, 1968.
- P. C. Sinclair. General characteristics of dust devils. *J. Appl. Met.*, 8:32 – 45, 1969.
- P. C. Sinclair. The lower structure of dust devils. *J. Atmos. Sci.*, 30:1599 – 1619, 1973.
- B. E. Sleep. Modeling transient organic vapor transport in porous media with the dusty gas model. *Adv. Water Resour.*, 22(3):247 – 256, 1998.
- J. T. Snow. A review of recent advances in tornado vortex dynamics. *Rev. Geophys. Space Phys.*, 20(4):953 – 964, 1982.
- J. T. Snow and D. E. Lund. Considerations in exploring laboratory tornadolike vortices with laser doppler velocimeter. *J. Atmos. and Oceanic Tech.*, 14:412 – 425, 1997.
- C. Soret. Sur l'état d'équilibre que prend, du point de vue de sa concentration, une dissolution saline primitivement homogène, dont deux parties sont portées à des températures différentes. *Arch. Sci. Phys. Nat.*, 2:48–61, 1879.
- C. G. Speziale, S. Sarkar, and T. B. Gatski. Modelling the pressure-strain correlation o turbulence: An invariant dynamical system approach. *J. Fluid. Mech.*, 227:245 – 272, 1991.
- D. A. Stonestrom and J. Rubin. Air permeability and trapped air content in two soils. *Water Resour. Res.*, 25(9):1947–1958, 1989.

- H. W. Teunissen. Wind tunnel simulation of atmospheric flows and its applicability to meteorological problems. Report, Environment Canada-Atmospheric Environment Service, 4905 Dufferin Street, Downsview, Ontario, 1974.
- P. Thomas and P. J. Gierasch. Dust devils on Mars. *Science*, 230:175 – 177, 1985.
- D. C. Thorstenson and D. Pollock. Gas transport in unsaturated zones: Multicomponent systems and the adequacy of fick's law. *Water Resour. Res.*, 25(3):477–507, 1989.
- B. J. Travis, N. D. Rosenberg, and J. N. Cuzzi. On the role of widespread subsurface convection in bringing liquid water close to Mars' surface. *J. Geophys. Res.*, 108 (E4), 2003.
- H. Tyrrell. *Difusion and Heat Flow in Liquids*. Butterworths, 1961.
- S. V. Vasiloff. *The Tornado: Its Structure, Dynamics, Prediction, and Hazards*, chapter Single-Doppler Radar Study of a Variety of Tornado Types, pages 223 – 231. American Geophysical Union, Washington, D. C., USA, 1993.
- H. K. Versteeg and W. Malalasekera. *An Introduction to Computational Fluid Dynamics*. Pearson Education Hall, 1995.
- N. B. Ward. The exploration of certain features of tornado dynamics using a laboratory model. *J. Atmos. Sci.*, 29:1194 – 1204, 1972.
- S. W. Webb. Gas-phase diffusion in porous media - evaluation of an advective-dispersive formulation and the dusty-gas model including comparison to data for a binary mixture. Report 1197, Sandia National Laboratories, Albuquerque, New Mexico 87185 and Livermore, California 94550, 1996.
- A. Wegener. Staubwirbel auf island. *Meteor. Z.*, 31:199, 1914.
- T. Wilson and R. Rottuno. Numerical simulation of a laminar vortex flow. In *Proceedings of International Conference on Computational Methods and Experimental Measurements*, Washington, D. C., USA, 1982. ISCME.
- Y. Z. Zhao, Z. L. Gu, Y. Z. Yu, Y. Ge, Y. Li, and X. Feng. Mechanism and large eddy simulation of dust devils. *Atmosphere-Ocean*, 42(1):61 – 84, 2004.

Appendix A

Additional Data

A.1 Multipycnometer

Tables A.1, A.2, A.3, A.4, A.5, and A.6 show the values obtained in the porosity experiments for the empty cell, the sphere, sample 1, sample 2, sample 3, and sample 4 respectively, thus:

Table A.1: Pressure obtained for the empty cell.

Experiment	P_1	P_2	P_1/P_2
Run 1	17.102 psig	6.409 pisp	2.668
Run 2	17.151 psig	6.427 psig	2.669
run 3	17.183 psig	6.438 pisp	2.669

Table A.2: Pressure obtained for the sphere.

Experiment	P_1	P_2	P_1/P_2
Run 1	17.104 psig	8.423 pisp	2.031
Run 2	17.142 psig	8.442 pisp	2.031
Run 3	17.227 psig	8.484 pisp	2.031

Table A.3: Pressure obtained for sample 1.

Experiment	P_1	P_2	P_1/P_2
Run 1	17.110 psig	6.486 psig	2.638
Run 2	17.231 psig	6.529 psig	2.639
Run 3	17.186 psig	6.551 psig	2.623

Table A.4: Pressure obtained for sample 2.

Experiment	P_1	P_2	P_1/P_2
Run 1	17.053 psig	6.467 psig	2.637
Run 2	17.109 psig	6.489 psig	2.637
Run 3	17.050 psig	6.467 psig	2.636

Table A.5: Pressure obtained for sample 3.

Experiment	P_1	P_2	P_1/P_2
Run 1	17.232 psig	6.528 psig	2.640
Run 2	17.049 psig	6.457 psig	2.640
Run 3	17.178 psig	6.504 psig	2.641

Table A.6: Pressure obtained for sample 4.

Experiment	P_1	P_2	P_1/P_2
Run 1	17.413 psig	6.598 psig	2.639
Run 2	17.078 psig	6.472 psig	2.639
Run 1	16.954 psig	6.423 psig	2.640

A.2 Pressure Transducer

Figure A.1 represents an schematic of the experiment used to calibrate the pressure transducer.

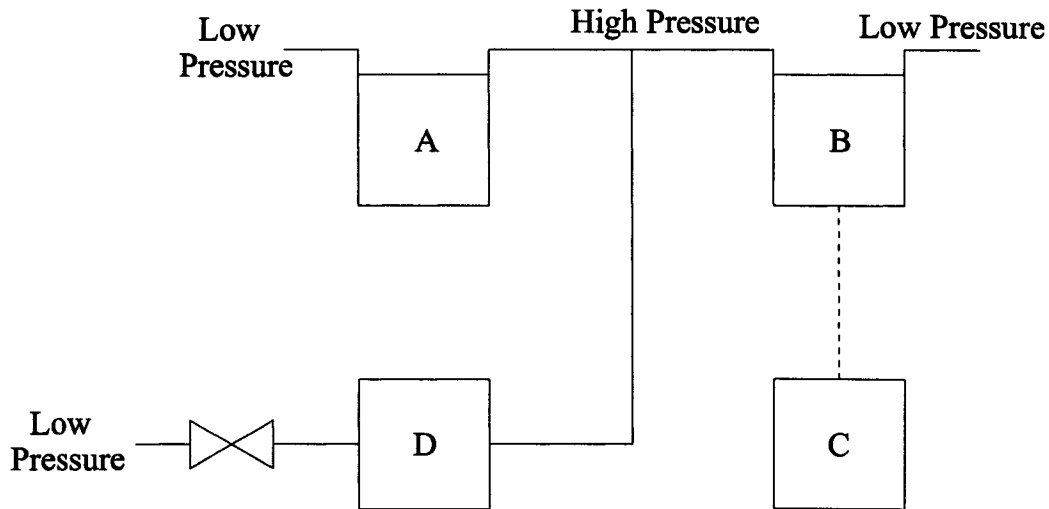


Figure A.1: A schematic of the calibration set-up used for the pressure transducer.

where the symbols stand for:

- A, Electronic point gage to determine the pressure in the system in inches of water.
- B, Pressure transducer, range ± 0.5 inches of water. This instrument was also used for the experiment described in Section 5.1.2.
- C, Water column to produce a $\pm \Delta P$ in the system.
- D, Voltmeter to register the changes of voltage produced by the pressure transducer.

Basically, the procedure to obtain the calibration curve was simple, by adjusting several heights in the water column; we were able to register the change in the voltmeter as a function of the pressure. Table A.7 represents the data obtained for this experiment:

Table A.7: Data obtained for the pressure calibration experiment.

ΔP [in. H ₂ O]	Voltage [V]	ΔP [in. H ₂ O]	Voltage [V]
-0.286	0.122	0.114	3.575
-0.234	0.598	0.129	3.692
-0.184	1.043	0.140	3.813
-0.092	1.853	0.140	3.823
0.000	2.556	0.162	4.037
0.020	2.717	0.186	4.230
0.036	2.856	0.204	4.403
0.039	2.898	0.212	4.438
0.050	3.011	0.237	4.672
0.059	3.082	0.244	4.744
0.076	3.242	0.276	5.042
0.078	3.223	0.277	5.037
0.083	3.317	0.298	5.226
0.084	3.326	0.310	5.343
0.100	3.457	0.311	5.322
0.113	3.588	0.334	5.546

A.3 Volume Flow Transducer

A simple experiment was designed to calibrate the volume flow transducer. Using a calibrated container of volume of $2 \cdot 10^{-3} \text{m}^3$, we measured the time to displace the water with air by prescribing several velocities. The data is collected in Table A.8.

Table A.8: Data obtained for the volume flow calibration experiment.

Voltage [V]	Time [s]
0.008 (For 0 m/s)	-
0.131	142.133
0.206	89.417
0.498	34.733
0.727	21.933

A.4 Permeability Data

Table A.9 presents the pressure difference as a function of the volume flow. The conversion used for the transducers were based on equations 5.5 and 5.6 (see chapter 5). Also, the volume flow is expressed in the terms of the true velocity (velocity inside the foam).

A.5 Adsorption Analysis

A series of three measurements were made for each foam sample. The average of the values were used in Table 5.6, Chapter 5.

True Velocity [m/s]	ΔP [Pa]	True Velocity [m/s]	ΔP [Pa]	True Velocity [m/s]	ΔP [Pa]	True Velocity [m/s]	ΔP [Pa]
≈ 0.00	0.4	≈ 0.00	0.16	≈ 0.00	0.26	≈ 0.00	0.24
7.18E-004	0.6	7.06E-003	4.34	1.17E-003	0.71	8.07E-003	3.96
1.44E-003	0.88	2.15E-002	13.08	4.03E-003	1.75	1.61E-002	7.59
8.21E-003	3.34	3.52E-002	20.89	1.19E-002	4.77	2.41E-002	11.17
1.61E-002	6.22	4.77E-002	28.4	2.03E-002	8.07	3.20E-002	14.87
2.47E-002	9.24	5.60E-002	33.8	2.66E-002	10.42	4.00E-002	18.61
3.23E-002	11.79	-	-	3.95E-002	15.31	4.54E-002	21.13
4.07E-002	14.87	-	-	5.63E-002	21.83	5.34E-002	24.85
5.04E-002	18.56	-	-	7.10E-002	27.62	6.14E-002	28.63
5.84E-002	21.52	-	-	8.23E-002	32.21	6.94E-002	32.43
6.57E-002	24.29	-	-	9.58E-002	37.55	7.75E-002	36.38
7.31E-002	27.09	-	-	1.11E-001	43.48	8.55E-002	40.24
8.20E-002	30.45	-	-	1.21E-001	47.54	9.36E-002	44.24
8.83E-002	32.82	-	-	1.27E-001	49.83	9.89E-002	46.87
9.77E-002	36.32	-	-	1.33E-001	52.32	1.07E-001	50.59
1.06E-001	39.4	-	-	-	-	1.15E-001	54.36
1.14E-001	42.5	-	-	-	-	1.23E-001	58.17
1.21E-001	44.94	-	-	-	-	1.31E-001	61.69
1.29E-001	48.07	-	-	-	-	-	-
1.44E-001	53.58	-	-	-	-	-	-

Table A.9: Data obtained for the permeability experiment.

Table A.10: Measured parameters of water adsorption.

Sample	Measurement 1	Measurement 2	Measurement 3	<i>RH</i>
1	72.977 g	72.995 g	72.981 g	16.04%
2	74.567 g	74.562 g	74.567 g	16.04%
1	74.231 g	74.210 g	74.189 g	66.30%
2	75.336 g	75.322 g	75.315 g	66.30%